Actively Tunable Plasmonic Nanostructures

by

Wade M. Wilson

Department of Electrical and Computer Engineering
Duke University

Date:_____

Approved:

_____
Maiken H. Mikkelsen, Advisor

_____
Adrienne D. Stiff-Roberts

_____
Aaron D. Franklin

_____
Steven A. Cummer

_____
Nan M. Jokerst

Dissertation submitted in partial fulfillment of
the requirements for the degree of Doctor of Philosophy in the Department of
Electrical and Computer Engineering in the Graduate School
of Duke University

2020

Abstract

Actively Tunable Plasmonic Nanostructures

by

Wade M. Wilson

Department of Electrical and Computer Engineering
Duke University

Date:_____
Approved:

_____
Maiken H. Mikkelsen, Advisor

_____
Adrienne D. Stiff-Roberts

_____
Aaron D. Franklin

_____
Steven A. Cummer

_____
Nan M. Jokerst

An abstract of a dissertation submitted in partial fulfillment of
the requirements for the degree of Doctor of Philosophy in the Department of
Electrical and Computer Engineering in the Graduate School
of Duke University

2020

Copyright by
Wade M. Wilson
2020

Abstract

Active plasmonic nanostructures with tunable resonances promise to enable smart materials with multiple functionalities, on-chip spectral-based imaging and low-power optoelectronic devices. A variety of tunable materials have been integrated with plasmonic structures, however, the tuning range in the visible regime has been limited and small on/off ratios are typical for dynamically switchable devices. An all optical tuning mechanism is desirable for on-chip optical computing applications. Furthermore, plasmonic structures are traditionally fabricated on rigid substrates, restricting their application in novel environments such as in wearable technology.

In this dissertation, I explore the mechanisms behind dynamic tuning of plasmon resonances, as well as demonstrate all-optical tuning through multiple cycles by incorporating photochromic molecules into plasmonic nanopatch antennas. Exposure to ultraviolet (UV) light switches the molecules into a photoactive state enabling dynamic control with on/off ratios up to 9.2 dB and a tuning figure of merit up to 1.43, defined as the ratio between the spectral shift and the initial line width of the plasmonic resonance. Moreover, the physical mechanisms underlying the large spectral shifts are elucidated by studying over 40 individual nanoantennas with fundamental resonances from 550 to 720 nm revealing good agreement with finite-element simulations.

To fully explore the tuning capabilities, the molecules are incorporated into plasmonic metasurface absorbers based on the same geometry as the single nanoantennas.

The increased interaction between film-coupled nanocubes and resonant dipoles in the photochromic molecules gives rise to strong coupling. The coupling strength can be quantified by the Rabi-splitting of the plasmon resonance at ~300 meV, well into the ultrastrong coupling regime.

Additionally, fluorescent emitters are incorporated into the tunable absorber platform to give dynamic control over their emission intensity. I use optical spectroscopy to investigate the capabilities of tunable plasmonic nanocavities coupled to dipolar photochromic molecules. By incorporating emission sources, active control over the peak photoluminescence (PL) wavelength and emission intensity is demonstrated with PL spectroscopy.

Beyond wavelength tuning of the plasmon resonance, design and characterization is performed towards the development of a pyroelectric photodetector that can be implemented on a flexible substrate, giving it the ability to be conformed to new shapes on demand. Photodetection in the NIR with responsivities up to 500 mV/W is demonstrated. A detailed plan is given for the next steps required to fully realize visible to short-wave infrared (SWIR) pyroelectric photodetection with a cost-effective, scalable fabrication process. This, in addition to real-time control over the plasmon resonance, opens new application spaces for photonic devices that integrate plasmonic nanoparticles and actively tunable materials.

Dedication

For my wife and children. You are my world.

Contents

List of Tables

List of Figures

Acknowledgements

I would like to thank my advisor, Professor Maiken Mikkelsen, for believing in me and giving me the opportunity to pursue my passion for plasmonics. Her insight and encouragement through my unique Ph. D. experience kept me on track despite the difficulties of starting a family, switching research groups, and the COVID-19 shutdown. Thank you to my defense committee, Professors Adrien Stiff-Roberts, Aaron Franklin, Nan Jokerst, and Steven Cummer. Your teaching, feedback, and guidance have been invaluable.

I would like to thank all of my labmates and friends that made my graduate school experience such an enjoyable one. Thank you Jon, Andrew, Qixin, Daniela, Nathan, and many others for your collaboration and friendship.

I would like to thank my family. Without the steadfast love and support of my wife, Alyssa, and inspiration from my children, Jack and Ada, I would not have been able to cross the finish line. Alyssa, thank you for your grace and commitment to helping me achieve my goals. I will love you always.

I would like to thank my parents, for their continual support through my academic career. Your example of hard work and devotion taught me to strive for success and do what is right. Thank you to my siblings who have been a source of happiness and love.

Finally, and most importantly, I must thank God. I am nothing beyond my identity in Christ Jesus. I cannot know what the future holds, but I know I am safe in His arms. John 3:16

1. Introduction

1.1 Perspective

Naturally occurring materials tend to suffer from weak absorption and lack narrow spectral features suitable for applications such as spectrally selective photonic sources and photodetectors [1]. Plasmonic metasurfaces based on subwavelength metallic elements can be employed to address the limitations of natural materials in wavelength ranges including the ultraviolet (UV) [2], visible [3], and from the near-infrared (NIR) [4] to the long-wave infrared (LWIR) [5]. Among these demonstrations, the use of bottom-up fabrication techniques has attracted much interest for its inherent scalability to large-area applications.

Plasmonic metamaterials are attractive for use in a variety of photonic applications because of their broad tunability and good spectral selectivity. Typically such metamaterials are fabricated using top-down lithographic techniques [6], limiting their scalability. Moreover, the use of lithographic techniques to tailor spectral responses in the UV to visible range is difficult due to the requirement of feature sizes much smaller than the wavelength of light. These limitations make the use of colloidally synthesized nanoparticles as the subwavelength plasmonic elements attractive for fabricating macroscopic scale photonic devices. Such solution-based fabrication allows for conformal, large-area coverage and can produce highly desirable optical properties including near-perfect absorption [4] and enhanced spontaneous emission [7].

These colloidal metasurfaces are typically made of metallic nanoparticles separated from a metal films by a dielectric spacer layer [8, 9]. This effectively fixes the optical response of the metasurface at the time of fabrication, only allowing it to be changed by refabricating the device or by inducing permanent morphological changes [10, 11]. This passive tunability is useful for tailoring the optical response of a metasurface to the desired application. Recent examples of inverse design show that nearly most arbitrary spectral shapes of the optical response can be achieved [12, 13]. However, since there are applications that may require multiple optical responses in a single on-chip device and simplicity of fabrication is more desirable for scalable processes, having the ability to dynamically shift the response is highly desirable. Incorporating active materials that have tunable mechanical and optical properties with plasmonic nanostructures promises to provide novel dynamic optical materials with full reversibility and repeatability.

In this dissertation, I explore the capabilities and physical mechanisms behind actively tunable plasmonic nanostructures as first published in Ref. [14]. Additionally, a similar nanostructure geometry is applied to a thermal photodetection platform in pursuit of a flexible photodetector.

1.2 Background

Active plasmonics have been pursued since the 1980s when early demonstrations of light modulators attempted to control surface plasmon resonances (SPR) with mechanical and electrical perturbation of the generation of surface plasmon polaritons

(SPP) [15-17]. The advent of nanotechnology brought the ability to control light-matter interactions at the nanoscale, opening the door to the use of deeply subwavelength features. These nano-sized features allow incident electromagnetic energy to be confined in ultra-small mode volumes, generating large field enhancements [18]. Furthermore, they allow the optical response of a photonic device to be tailored to the desired properties because their spectral shape is highly dependent on size, shape, and geometry [4].

These advances have generated exciting new possibilities for integrating plasmonic materials with active bulk materials, but several outstanding challenges remain in the search for reversible control over the optical response of photonic devices. First, typical nanophotonic fabrication procedures make it difficult to embed subwavelength elements into active surrounding materials with the required level of control over feature sizes and geometry for high performance devices. Second, most demonstrations of tunable materials integrated with plasmonics have limited variation in optical properties in the visible and NIR regimes, resulting in small on/off modulation ratios. Third, the mechanisms that provide large tuning ranges tend to apply stimuli to the nanostructure using external equipment that limits their use in on-chip applications. Finally, high performance nanophotonic devices are generally built on the well-understood, but rigid and opaque semiconducting substrates, which prohibits their applicability in wearable technologies.

To address these issues, recent research interest has focused on identifying novel tuning mechanisms and plasmonic nanostructures that allow for ease of integration and electrical or optical tuning techniques [19]. In particular, techniques that affect the local

environment around film-coupled plasmonic nanoparticles have received significant attention due to the development of novel functional materials that can be incorporated into the nanostructure itself. Moreover, the use of bottom-up fabrication techniques is of interest for developing scalable photonic devices [4]. These tunable plasmonic nanostructures have demonstrated a wide range of optoelectronic and nanophotonic applications including sensors, photonic components, and imaging [19-22].

1.3 Organization

This dissertation is organized as follows. Chapter 2 provides an introduction to the field of plasmonics, the use of active materials to tune plasmon resonances, enhancement of emission and absorption in plasmonic nanostructures, as well as the application of plasmonics to thermal photodetection. Chapter 3 discusses the mechanisms and capabilities of plasmonic nanoantennas with integrated phase change materials to provide active control over the plasmon resonance and applies this behavior to control the coupling strength of a plasmonic metasurface absorber to the materials' resonant dipoles. In Chapter 4, fluorescent dyes are used to evaluate the ability of tunable metasurfaces to control their emissive properties. Chapter 5 applies the plasmonic metasurfaces absorbers to thermal photodetection to allow for a simple, scalable photodetector fabrication procedure.

2. Active Plasmonics

2.1 Introduction

Resonant plasmonic devices can be tailored for the desired optical response due to their inherent dependence on device geometry and optical properties. Customarily, plasmonic nanostructures are embedded in a static environment. This effectively fixes the device structure, shape, and thus the plasmon resonance which can only be changed by refabricating the device or inducing permanent morphological changes [10, 23]. However, dynamic, "smart" materials with optical and physical properties that can be controlled in real time would allow for tailored optical response for multiple applications without having to refabricate the device. While there are many methods for achieving this dynamic control, there are a few that stand out for their large change in spectral response, speed of switching between states, or ability to be integrated into on-chip applications. The fundamentals of plasmonic nanoantennas are reviewed in section 2.2 to provide a foundation for the work described in this dissertation. Section 2.3 gives a brief discussion of mechanisms that can be used to tune plasmonic devices. Plasmonic enhancement of emission is discussed in section 2.4. Section 2.5 overviews thermal photodetection in the context of plasmonics and defines the challenge of developing a flexible photodetection platform.

2.2 Plasmonic nanoantennas

In the early 1950s, Bohm and Pines presented a new approach to describing electron energy losses in gases and on thin foils as "collective", suggesting that the energy losses

were due to plasma oscillations among collections of conduction electrons [24-26]. Stern and Ferrell later noted that the energy losses at a metal-dielectric interface resulted from plasma oscillations at the metal surface in which part of the restoring electric field extended into the dielectric material [27]. This causes the plasma oscillation to be highly sensitive to the material properties on both sides of the metal-dielectric interface [28]. The effect was described as the excitation of electromagnetic evanescent waves at the metal surface, which are referred to as surface plasmons.

Surface plasmons can be excited by incident electromagnetic energy in subwavelength metallic particles, confining the evanescent wave to the surface of the nanoparticle and the near field just outside, thus localizing it. When the driven electrons in the localized surface plasmon (LSP) experience a restoring force from atomic nuclei in the metal surface, resonance can occur resulting in an increase in the amplitude of oscillation (field enhancement) [30]. This resonance is referred to as localized surface plasmon

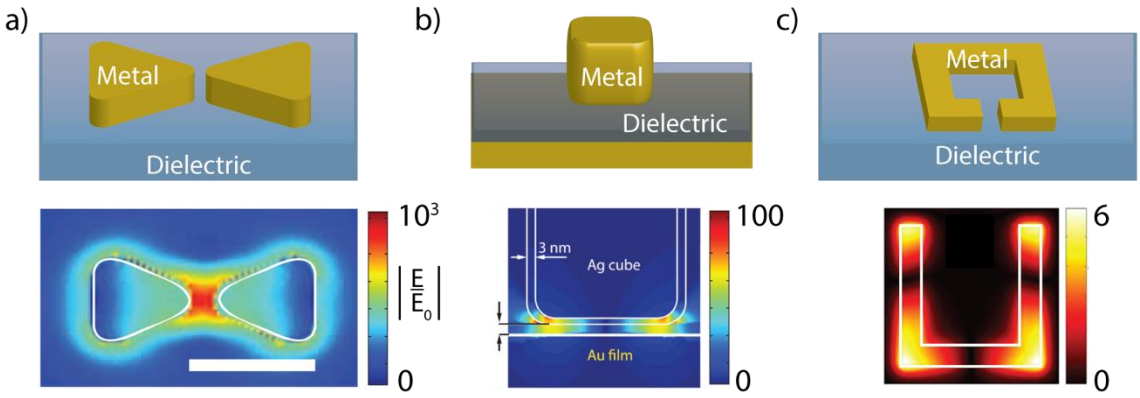

Figure 2.1: Schematics and field profiles of plasmonic nanostructures. (a) Bowtie antenna [30], (b) nanocube coupled to metal film [31], (c) split-ring resonator [39].

resonance (LSPR). LSPR results in amplified electric and magnetic fields that can be exploited for many interesting applications. Because the momenta of incident photons and LSPs must match for resonance to occur, a LSPR occurs at a particular resonant frequency (photon energy). Since the resonance phenomenon depends on the generation of surface plasmons, its resonant frequency is dependent on the dielectric environment surrounding the nanoparticle. This includes the geometry, size, and material properties of the nanoparticles and the surrounding media. Many plasmonic nanostructure designs have been used to study LSPRs including film-coupled nanoparticles of varying shapes [30-39]. Figure 2.1 shows the structures and field profiles for several different plasmonic nanostructures including a bowtie antenna [30], film-coupled nanocube [31], and split-ring resonator [39], demonstrating their ability to confine energy and produce large field enhancements.

Because the LSPR is so dependent on the material properties of its surroundings, the optical response of plasmonic devices can be engineered by selecting materials and designing the size and geometry of the nanostructure. There have been demonstrations of plasmonic nanostructures that can be tailored across a wide spectral range, but once fabricated the operating wavelength is either fixed or the nanostructure must be permanently altered to change it [10, 23]. Incorporating active materials with plasmonic nanostructures promises to provide novel dynamic optical materials with full reversibility, repeatability, and ultrafast response times. In the next section, various methods for achieving dynamic tuning of plasmon resonances are discussed.

2.3 Mechanisms for active tuning

2.3.1 Phase change materials

Plasmonic devices are inherently sensitive to their surrounding dielectric environment. Therefore a simple method for achieving dynamic control is to incorporate a material into the device structure that has actively tunable optical properties. Phase change materials (PCM)are those that undergo a transition from one state of matter to another upon absorbing or releasing energy. The transition could also be from a particular crystalline or chemical structure to another. PCMs have been utilized in many applications including energy storage [40], tunable material properties [41], and digital memory systems [42].

Materials that undergo a phase transition between two solid states with differing optical properties are of particular interest for photonic devices. In most solids, crystalline and amorphous states have very similar optical properties because their bond structures do

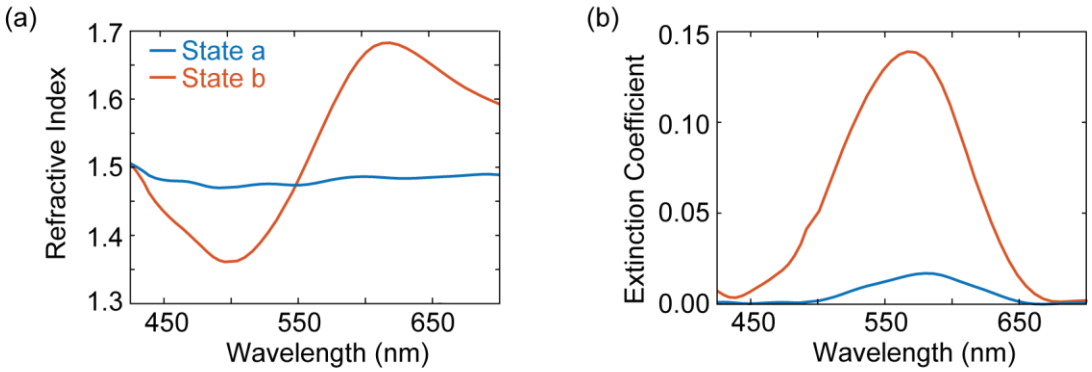

Figure 2.2: Optical properties of spiropyran (SPI). Refractive index (a) and extinction coefficient (b) for a PCM before and after the phase change. The blue lines show the properties of one particular state while the red lines show the properties after the phase change. This data was first reported in Ref. [14].

not differ significantly [43]. PCMs in contrast exhibit drastically different bond structures upon transitioning between phases and thus exhibit different optical properties after switching. This process is best visualized by looking at the material's transition-induced change in refractive index (n) and extinction coefficient (k), which describe its response to an applied electric field. Figure 2.2 shows n and k for a common class of PCM known as spiropyrans [14]. There is a clear difference in the optical properties between the two states. The change in optical properties can be exploited to actively control the optical properties of a photonic device.

Because they can be easily incorporated into plasmonic nanostructures, PCMs have been widely studied as a method to modulate the plasmon resonance in pursuit of actively tunable photonic devices [14, 41, 44-48]. Some examples of common PCMs employed in plasmonics are vanadium dioxide (VO_2) [44-47] and germanium antimony telluride (GeSbTe, "GST") [41,48]. These are materials that exhibit thermal transitions at 68 C [44] and 160 C [48], respectively, allowing for active control over the optical properties by heating the sample beyond its transition temperature. In the case of VO_2, the transition causes the crystalline structure to transition from insulating (<68 C) to metallic (>68 C) [44]. On the other hand GST transitions from amorphous to crystalline when heated beyond its critical temperature. These transitions can occur at picosecond timescales across the entire sample area [41]. However, the change in optical properties are most prominent at particular frequencies where the material has the most change in physical properties. For example, spiropyran transitions from electrically inert to dipolar under UV illumination

[14]. The largest change in optical properties occurs near the dipolar resonance. For many PCMs this prohibits operation at visible wavelengths due to the small shifts in optical properties exhibited in this regime.

2.3.2 Direct variation of dielectric environment

Another tuning mechanism that has enjoyed significant research volume is direct variation of the dielectric environment around the plasmonic nanostructure. This is often achieved through optical or electrical enhancement of the local density of states around the nanostructure [31, 49-59].

The density of states of a system describes the number of available states that can be occupied at a particular energy level. When a system is inhomogeneous (having multiple materials), the density of states can be spatially resolved. This is denoted as the local density of states (LDOS). For electrically tunable devices, an applied bias across the device injects carriers which can form an accumulation or depletion layer at a metal-insulator interface. The accumulation of carriers at this interface alters the LDOS and thus the optical refractive index of the device. Several methods for charge injection in plasmonic devices have been studied including embedding the plasmonic nanostructure in liquid crystal [31, 53, 56, 57] and sandwiching it in the dielectric spacer between two metal contacts [54, 55, 58]. Electrically tuning the LDOS is conducive for designing integrated photonic devices that can be electrically addressed alongside other electronics such as readout circuitry and input/output devices [59].

Similarly, the LDOS can be modulated optically by incident laser excitation of inter- or intraband transitions in the device to inject charge carriers though optical absorption [49-52]. Photonic devices based on this tuning scheme can be pumped with ultrafast laser pulses, yielding femtosecond response times that can be used to study the transient behavior of LSPRs [49]. This tuning scheme is particularly suited for optical computing applications due to its all-optical nature and fast response times. However, like other tuning mechanisms, optical modulation of the LDOS relies on the intrinsic absorption properties of the materials involved to stimulate changes in the plasmon resonance of devices. This typically restricts the operating regime of devices to wavelengths longer than the visible spectrum where material band gaps are lower.

2.3.3 Structural modification

Similar to techniques that modify the dielectric environment surrounding plasmonic nanostructures, methods that take advantage of the dependence of plasmon resonances on device geometry can achieve large shifts in the response of the device. Because plasmonic structures are highly sensitive to sub-nanometer scale changes in device geometry, large shift in plasmon resonance can be induced by small structural changes in the device. These can be induced by mechanical [60], chemical [61-66], or thermal [67, 68] deformations. For example, a device can be tuned by stretching an elastomeric substrate to increase or decrease the distance between plasmonic nanoparticles [60].

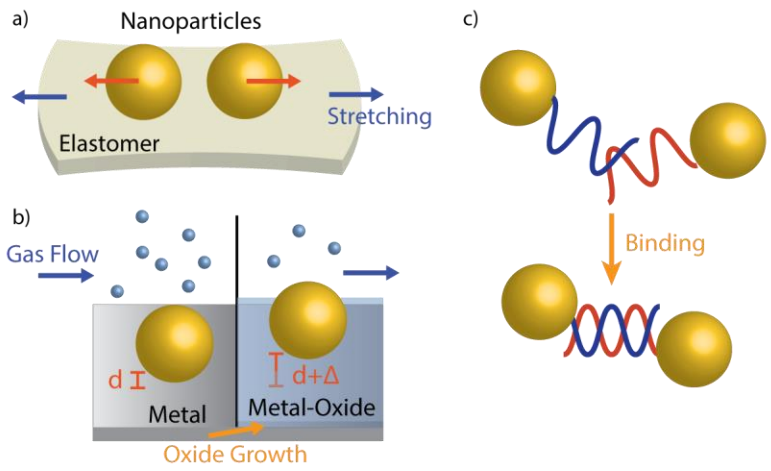

Figure 2.3 Methods of structural modification. (a) Two metal nanoparticles form a dimer on a stretchable elastomer substrate. (b) A metal nanoparticle is suspended over a metal film. An oxide layer is formed when an oxidizing agent is flowed over the substrate. (c) Two metal nanoparticles are functionalized with a reactive molecular structure that can bind to its complimentary molecule to form a dimer by bringing the nanoparticles close together.

Figure 2.3(a) depicts this type of tuning for a generic dimer of metal nanoparticles. Part (b) shows how a chemical reaction can be used to modify the geometry of a film-coupled nanoparticle system, where the plasmon resonance depends on the thickness of the oxide growth. Part (c) shows a schematic representation of a simple chemical reaction sensing system in which the binding of complimentary molecules (DNA, for instance) changes the spacing between nanoparticles. The resulting plasmon resonance changes can be large compared to non-structural tuning mechanisms, but tend to rely on external mechanical [60] or chemical [61] stimuli that are not conducive to compact, on-chip applications.

2.4 Enhancement of emission

Typically, luminescent emitters have long intrinsic emission lifetimes and non-directional emission making them ill-suited for high performance nanophotonic devices. Furthermore, limiting their absorption efficiency to the natural absorption profile of the emitter can prohibit their use in applications requiring broadband absorption or low incident intensity. Generally, there are two methods for improving the properties of optical emission using plasmonic nanostructures. (1) By overlapping the plasmon resonance of the nanostructure with the absorption cross-section of the emitter, large enhancements up to 30,000 times can be achieved because more of the incident excitation energy is absorbed by the emitter [69]. (2) Large photoluminescence (PL) enhancements over 1000 times can be achieved by spectrally overlapping the resonance of the nanopatch antenna with the emission from fluorescent dyes and quantum dots [7, 70]. In this case the Purcell effect enhances the spontaneous emission rate by increasing the local density of available states, thus increasing quantum efficiency [71]. The spontaneous emission rate of a generalized dipole is given by [72]:

$$\gamma_{sp}(\vec{r}) = \frac{\pi\omega}{3\hbar\varepsilon_0}|\vec{p}|^2\rho(\vec{r},\omega) + \gamma_{int}^0 \tag{2.1}$$

where ω is the emission frequency, $\vec{p}$ is the transition dipole moment of the emitter, $\vec{r}$ is position, and γ_{int}^0 is the non-radiative decay rate of the emitter. When coupled to the nanopatch antennas, the high field intensities enhance the local density of states according to:

$$\rho(\vec{r},\omega) \propto \widehat{n_p} \cdot \mathrm{Im}\{G(\vec{r},\vec{r})\} \cdot \widehat{n_p} \tag{2.2}$$

where $\widehat{n_p}$ is the orientation of the transition dipole of the emitter and G is the dyadic Green's function, representing the electric field's interaction with the emitter [70]. The resulting Purcell factor, $F_p = \gamma_{sp}/\gamma^0_{sp}$, is dependent on the amount of confinement of the incident electromagnetic energy and can be approximated as the ratio between the nanocavity quality factor and its mode volume ($F_p \sim Q/V$), thus necessitating high Q-factors and small

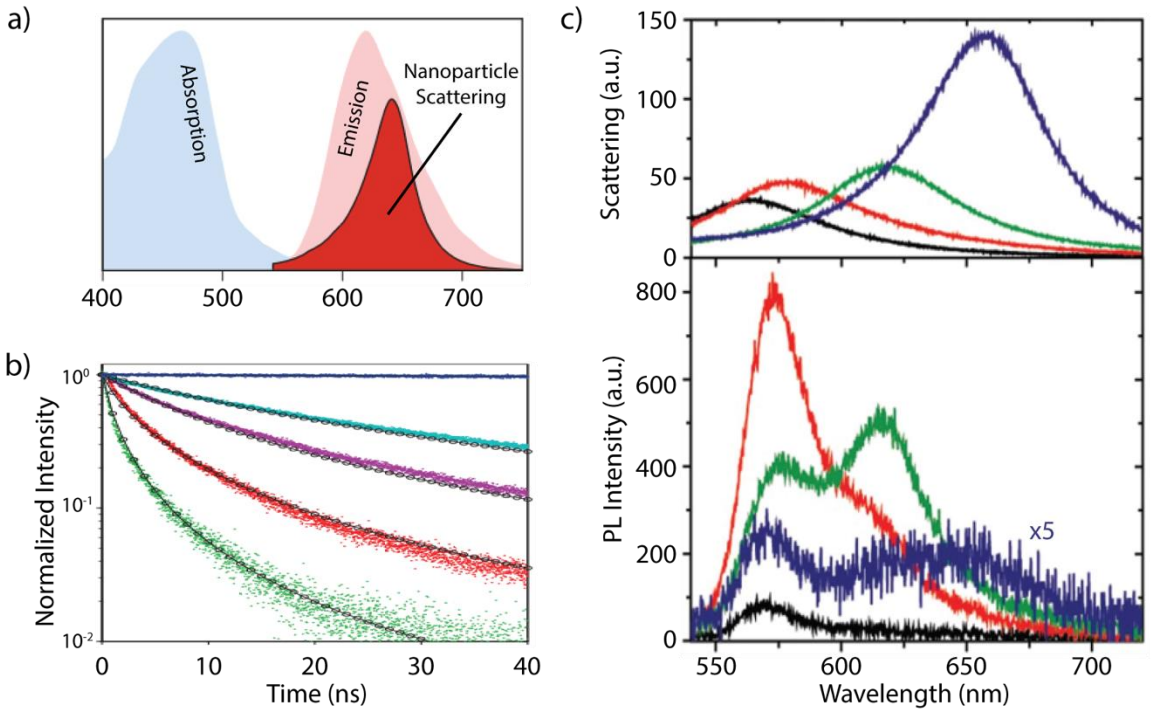

Figure 2.4: Plasmonic enhancement of spontaneous emission. (a) Scattering from nanocavity and fluorescence intensity from fluorescent emitter [70]. (b) Time-resolved emission intensity resulting from different nanocavity coupling strengths [70]. (c) Scattering from nanoparticle dimers overlaid with the PL intensity with spectrally shifted along with the peak scattering wavelength [75].

mode volumes [73, 74]. Figure 2.4(a,b) shows the effect of the coupling strength between a plasmonic cavity and emitter on the spontaneous emission rate, with more spectral overlap between the emitter and cavity corresponding to a shorter spontaneous emission lifetime (higher spontaneous emission rate) [70].

When the resonance only overlaps a portion of the dye's emission spectrum, those wavelengths are selectively enhanced and the wavelength with peak PL intensity is effectively shifted to the plasmon resonance as shown in Figure 2.4(c) [75]. This process can be used to extend the breadth of an emitter's spectrum to previously dim wavelengths, or shift the wavelength of maximum intensity. Wavelength-selective enhancement will be most effective when the Q-factor of the nanoantenna is sufficiently high to make its optical response spectrally narrower than that of the emitter so that only a portion of the spectrum is enhanced. Alternatively, a broad nanoantenna response can be acceptable if used to overlap a portion of the emitter's spectrum that has low quantum efficiency, extending the wavelength range of emission. These enhancement techniques give insight into how the performance of fluorescent sources can be improved or tailored to a desired optical response. This control over the emissive properties is critical for the development of dynamically controllable photonic sources.

2.5 Thermal photodetection

2.5.1 Review of thermal photodetector mechanisms

Most modern photodetectors use a photoelectronic mechanism to generate electron hole pairs. In these "quantum" or "photon" detectors, charge collection relies on

photoemission, photovoltaics or photoconductivity to convert the incident light energy into a current or voltage for readout [76]. These phenomena rely on the absorption of photons to generate charge carriers in the form of separated electron-hole pairs that can be measured, thus limiting the detection ability to the frequency regime where electrons in that material can be excited with enough energy to overcome the potential barrier [77]. This means different absorbing materials are required to detect in different wavelength regimes from UV to IR. By contrast, thermal detectors are uniquely capable of sensing at any frequency because they do not rely on the generation of electron-hole pairs with photon absorption. Rather than detecting photons directly, they respond to the temperature increase caused by the absorption of incident photon energy, thus eliminating the requirement of sufficient photon energy to separate an electron-hole pair.

2.5.1.1 Figures of merit

There are several key figures of merit for photodetectors, regardless of detection mechanism. The relative importance of each one depends on the desired application. Responsivity, defined as the output signal level per unit of incident light power, tends to be the foremost measure of performance for thermal photodetectors because it measures the detector sensitivity. It can be expressed as:

$$R = \frac{I_{ph}}{P_{in}}\left(\frac{A}{W}\right), \text{or } \frac{V_{ph}}{P_{in}}\left(\frac{V}{W}\right) \tag{2.3}$$

where I_{ph} is the photocurrent, P_{in} is the incident power, and V_{ph} is the photovoltage. The use of the photovoltage or photocurrent is determined by the readout circuit. Since

dispersion and absorption are closely related, there will be a spectral dependence to the responsivity of thermal photodetectors. If the desired application requires a broad spectral range, maximizing the average responsivity over that range at the expense of the peak responsivity would be preferred. For spectrally selective detectors, a narrow responsivity spectrum with a large peak is more desirable. The shape of the photoresponse is ultimately determined by the optical properties of the absorbing material.

Another consideration for thermal photodetectors is their temporal response. The two most common ways of measuring the speed of a detector are the rise/fall time and the bandwidth. The rise time (t_r) is defined as the time required for the detector signal to reach 90% of its peak value in response to incident light. Likewise the fall time (t_f) is the time required for the signal to decay to 10% of its peak value. For thermal detectors one of these values tends to limit the overall speed of the device, especially when the detector area is thermally isolated to increase sensitivity. In this case there thermal diffusion is limited by the low heat conductance of the materials surrounding the absorber and thus t_f will be the time-domain limit for the detector speed. The bandwidth (f_{3dB}) is the frequency domain measure of detector response speed. It is defined as the input light modulation frequency at which the peak detector signal is reduced by 3 dB (50%). A large bandwidth is desirable for high speed detector applications.

While the signal level and speed are important considerations, the noise performance of the detector must be considered, especially to compare detectors made with different materials and geometries. The noise equivalent power (NEP) is defined as the

minimum incident power required to generate a signal to noise ratio of 1 with a 1 Hz modulation rate. It can be expressed as:

$$\mathrm{NEP} = \frac{\overline{I_n^2}^{1/2}}{R_I} \text{ or } \frac{\overline{V_n^2}^{1/2}}{R_V} \tag{2.4}$$

where I_n and V_n are the noise current and voltage, respectively and R is the responsivity. The NEP gives a measure of the minimum intensity that can be reliably detected above the noise level. The detectivity, D^*, normalizes the detector performance to its size and is calculated as:

$$D^* = \frac{(A * f_{3dB})^{1/2}}{\mathrm{NEP}} \tag{2.5}$$

where A is the detector area and f_{3dB} is its bandwidth. The detectivity is a powerful tool for comparing detectors because it accounts for their respective sizes.

There are several types of thermal photodetectors, but with an eye toward plasmonic enhancement, they can generally be classified into 1) bolometers, 2) thermopiles, and 3) pyroelectrics. This section reviews the basic operating principles of each type of detector along with some of their advantages and limitations.

2.5.1.2 Bolometers

Bolometers, first invented by Samuel Langley, consist of an absorbing material connected to a thermal reservoir by a thermal link [78]. They function by inducing a temperature increase in the absorbing material when struck by incident light which can be measured as a change in its resistance or with an attached resistive thermometer. Figure

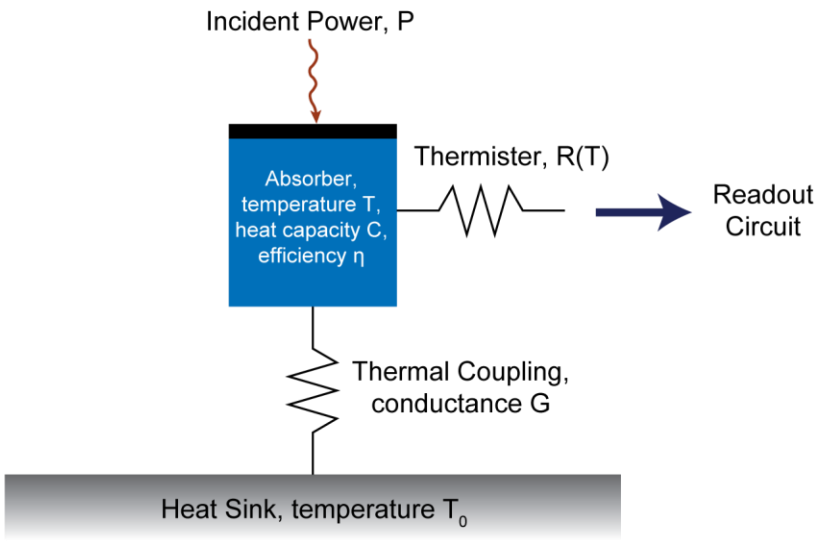

Figure 2.5: Schematic of generalized bolometer. The thermal absorber converts incident electromagnetic energy into a temperature difference between the absorber and the heat sink. This temperature difference drives a resistance change that can be measured by a readout circuit.

2.5 depicts an example structure of a basic bolometer wherein incident photon energy is absorbed as heat, increasing the temperature of the bolometer from the temperature of the thermal reservoir,T_0, to T. This heat is dissipated through a thermal link with thermal conductance G. The sensitivity of the device is dependent on the thermal isolation of the absorbing element from the thermal reservoir by a support with low G. The thermal balance between the heat sink and the absorbing layer is described by [79]:

$$\eta P = C\frac{dT}{dt} + G(T - T_0) \tag{2.6}$$

where P is incident power, η is the quantum efficiency, and C is the specific heat of the absorbing material. At steady state, the temperature increase of the bolometer is dependent

on the absorption efficiency and thermal conductance. The time constant to reach thermal equilibrium, τ = C/G, determines the thermal limit for detector bandwidth. The photoresponse is highest when the absorption is maximized and thermal conductance is minimized. However, reducing the thermal conductance increases the lifetime because it takes longer for the generated heat to dissipate, introducing a tradeoff between detector speed and sensitivity.

2.5.1.3 Thermopiles

A thermopile is a series or array of interconnected thermocouples. Thermocouples operate due to the thermoelectric effect, first observed by Thomas Seebeck in 1821 [80]. Figure 2.6(a) shows a basic schematic of a thermocouple consisting of two dissimilar metal wires, joined at one end and insulated from each other elsewhere. The end where they are joined is the measuring or "hot" junction. At the other end of each wire, a junction connects them to the terminals of the readout equipment. This junction is typically maintained at a constant reference temperature, thus it is referred to as the "cold" junction. The temperature difference along the wires increases the kinetic energy of electrons on that side of the wire, causing them to diffuse to the cold side. As a result, an electromotive force (V_{emf}) is produced in the wire according to the Seebeck effect:

$$V_{emf} = -S\Delta T \tag{2.7}$$

where $\Delta T = (T-T_0)$ is the temperature difference induced by the temperature gradient between the hot and cold sides, and S is the Seebeck coefficient, an intrinsic property of the material. The different materials in the two wires have different thermal and electrical

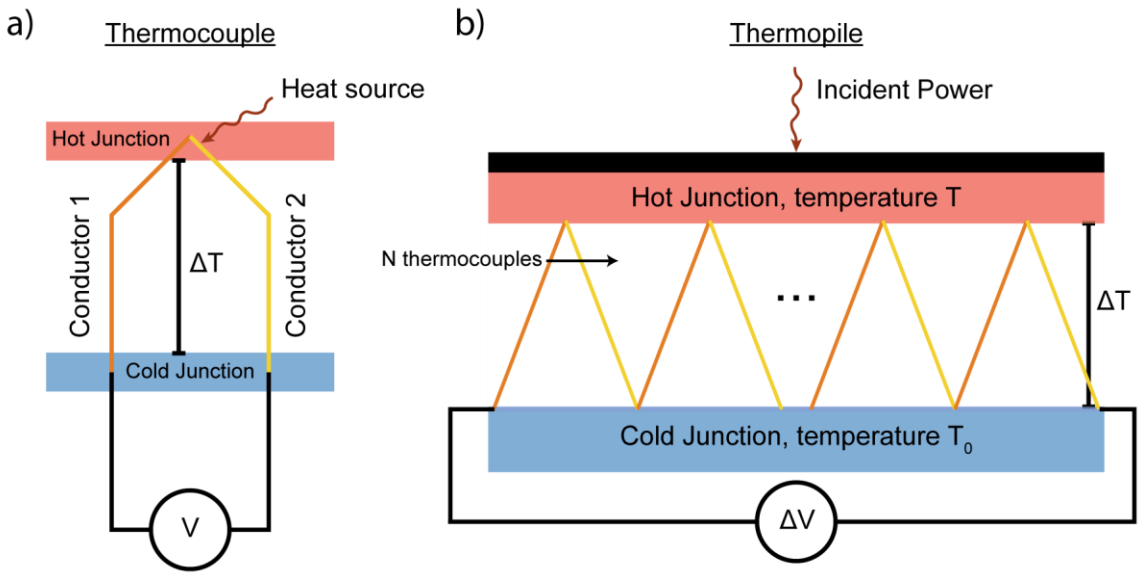

Figure 2.6: Schematic of generic thermopile. (a) Basic components of a thermocouple. (b) Thermopile consisting of N thermocouples where the generated voltage (ΔV) depends on N and the temperature change (ΔT) induced by the incident electromagnetic energy.

transport properties, producing two different voltages at the cold terminals between the hot and the cold junctions. A meter attached to the two wires at the cold junction can be used to measure the voltage differential which correlates to the temperature difference between the two materials.

When multiple thermocouples are arranged in series to make a thermopile, as shown in Figure 2.6(b), the voltages produced by the thermocouples is added to produce a larger total voltage in the device. The voltage generated by the thermopile, ΔV, is directly proportional to the temperature difference between the two materials in each thermocouple, ΔT, and to the number of thermocouples in series, N:

$$\Delta V \propto N \cdot \Delta T \tag{2.8}$$

where the constant of proportionality is the Seebeck coefficient of the thermocouples that comprise the thermopile.

Like in the case of bolometers, the signal in thermopiles does not depend on exciting electron hole pairs. Therefore it has no spectral dependence when sensing incident light beyond the spectral dependence of the absorbing material's quantum efficiency, which can be tailored to the desired application. Because the signal in thermocouples is self-generating, no bias voltage is required, eliminating the issues of offset, drift and interference from power supplies [81]. Furthermore, the readout circuit is simple because it only has to measure a small differential voltage. Unfortunately, the output signal for thermopiles tends to be small, on the order of a few microvolts, requiring the use of amplifier circuits [82].

2.5.1.4 Pyroelectrics

Pyroelectricity is a crystalline material property wherein the material is naturally electrically polarized [83]. This built-in polarization is a result of crystalline asymmetry, leading to changes in the polarization when the material absorbs heat. Figure shows the unit cell for polyvinylidine fluoride (PVDF), a commonly used pyroelectric polymer. The direction of electric polarization is shown on the crystal structure. This spontaneous polarization decreases as the crystal is heated, resulting in a change in the bound charge accumulation at the edges of the crystal. If the pyroelectric material is sandwiched between two conductive plates, as depicted in Figure 2.7 (a-c), surface charges accumulate at the conductor-pyroelectric interface. When the detector is heated by incident photon energy,

the spontaneous polarization of the crystal decreases, releasing the trapped surface charges. An external circuit can be connected to the conductor on each side of the crystal to collect the flow of surface charge. This configuration causes the crystal to act as a current source according to:

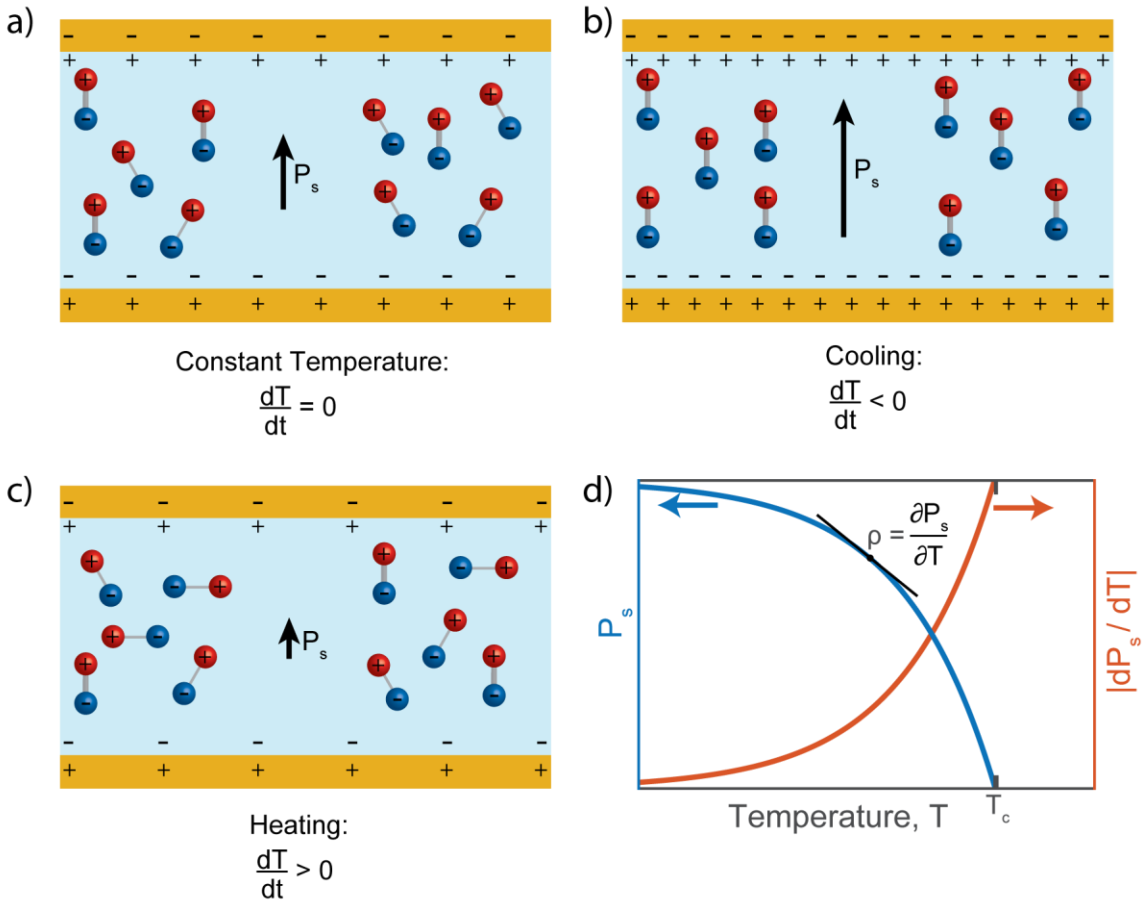

Figure 2.7: Operating principle of pyroelectric photodetector. (a) Spontaneous polarization state when detector is at constant temperature. (b) Increased spontaneous polarization while detector is cooling. (c) Decreased spontaneous polarization while detector is heated. (d) Spontaneous polarization and pyroelectric coefficient plotted against temperature.

$$i_p(t) = A\rho\frac{dT(t)}{dt} \tag{2.9}$$

where A is the crystal area in contact with the conductor, ρ is the pyroelectric coefficient of the crystal and T(t) is the temperature of the pyroelectric crystal as it evolves over time through heat diffusion. It is important to note that the pyroelectric current depends on the rate of change of the temperature with time, meaning for constant temperature there is no signal. The pyroelectric coefficient is defined as:

$$\rho = \frac{\partial P_s}{\partial T} \tag{2.10}$$

where P_s is the spontaneous polarization of the crystal and T is the temperature. Figure 2.7(d) shows an example of how the spontaneous polarization varies with temperature for a generic pyroelectric crystal. The pyroelectric coefficient, represented by the tangent line on the polarization curve, increases in magnitude with temperature until $T=T_c$ where the spontaneous polarization vanishes. This temperature is known as the Curie temperature and is a characteristic of the crystal. In general, a larger pyroelectric coefficient yields a larger signal so it can be beneficial to operate the device at higher temperatures that are just below the crystal's Curie temperature. Beyond the Curie temperature, the crystal is no longer pyroelectric so caution should be taken to maintain the device temperature below T_c either through cooling the detector or by choosing a pyroelectric material with a high T_c.

2.5.2 Plasmonic enhancement

The thermally sensitive devices outlined in this chapter offer several advantages over photon detectors, but are typically limited by sensitivity and response time. To

mitigate the inherent limitations of thermal detectors, many photonic structures have been proposed to give spectral selectivity and improve sensitivity or response time [1, 84-86]. Much of the recent work in plasmonic enhancement of thermal detection has focused on spectral selectivity and sensitivity at infrared wavelengths [87-89] and improving response speed [90-92]. In pursuit of faster and more sensitive thermal detectors, highly engineered materials that consist of subwavelength sized features, known as metasurfaces, have been employed because they offer tailorable spectral responses based on exciting localized surface plasmon resonances (LSPRs) [93, 94]. These metasurfaces can be designed to match their effective surface impedance to the dielectric environment around them, allowing for near-unity absorption at the resonance wavelength of the subwavelength elements. By confining incident light to a subwavelength volume where LSPRs dissipate the energy as heat [4], metasurface absorbers make ideal candidates for improved performance in thermal photodetection.

Recent demonstrations using 2D hole arrays and pyroelectric ZnO by Dao *et al*. have produced efficient room temperature coupling of incident infrared light into thermal decay pathways that heat a thermally-responsive film to produce an electronic signal [87]. The spectrally selective detection is tunable in wavelength by changing the fabrication parameters to produce different hole size and spacing, thus adjusting the plasmon resonance. Tang *et al*. developed a thermal imaging system based on HgTe QDs that achieved a detectivity of 4×10^{11} Jones, surpassing the sensitivity of most commercially available thermal imaging systems [96]. Furthermore, a recent study by Efetov *et al*. of

graphene bolometers produced thermal relaxation times as fast as 35 ps [97]. However, this was a measure of the internal thermal dynamics, not the external measurement speed. A demonstration of ultrafast pyroelectric photodetection was shown by Stewart *et al*. with spectrally selective detection wavelengths spanning from the NIR to MWIR [90]. These tunable detection platforms are important demonstrations of the design process for plasmonically enhanced thermal photodetector, but each one has its performance drawbacks. As described in the previous sections, the nature of thermal photodetection produces tradeoffs between each of the key performance metrics. The challenge of producing room-temperature thermal photodetection at visible wavelengths with high detectivity still remains.

2.5.3 PVDF and copolymer

Many of the previous demonstrations of plasmonic enhancement of thermal detectors use materials that provide highly crystalline thin films [4, 85-91]. These materials are engineered to have optimal thermal responses, but typically require complex deposition or post-processing to achieve high degrees of crystallinity and surface quality. A viable alternative is to use pyroelectric polymers that can be deposited by simple methods such as spin coating [98-101]. One such polymer is polyvinylidine fluoride (PVDF), with the chemical formula $(C_2H_2F_2)_n$ and well known pyroelectric properties [102].

There are 5 known crystalline phases for PVDF: the all-trans (TTT) β-phase, the TGTG' α- and δ-phases, and the T3G γ- and ϵ-phases. The polymer chain can be settled into a crystal with parallel dipoles, forming a net dipole moment for the entire crystal. This

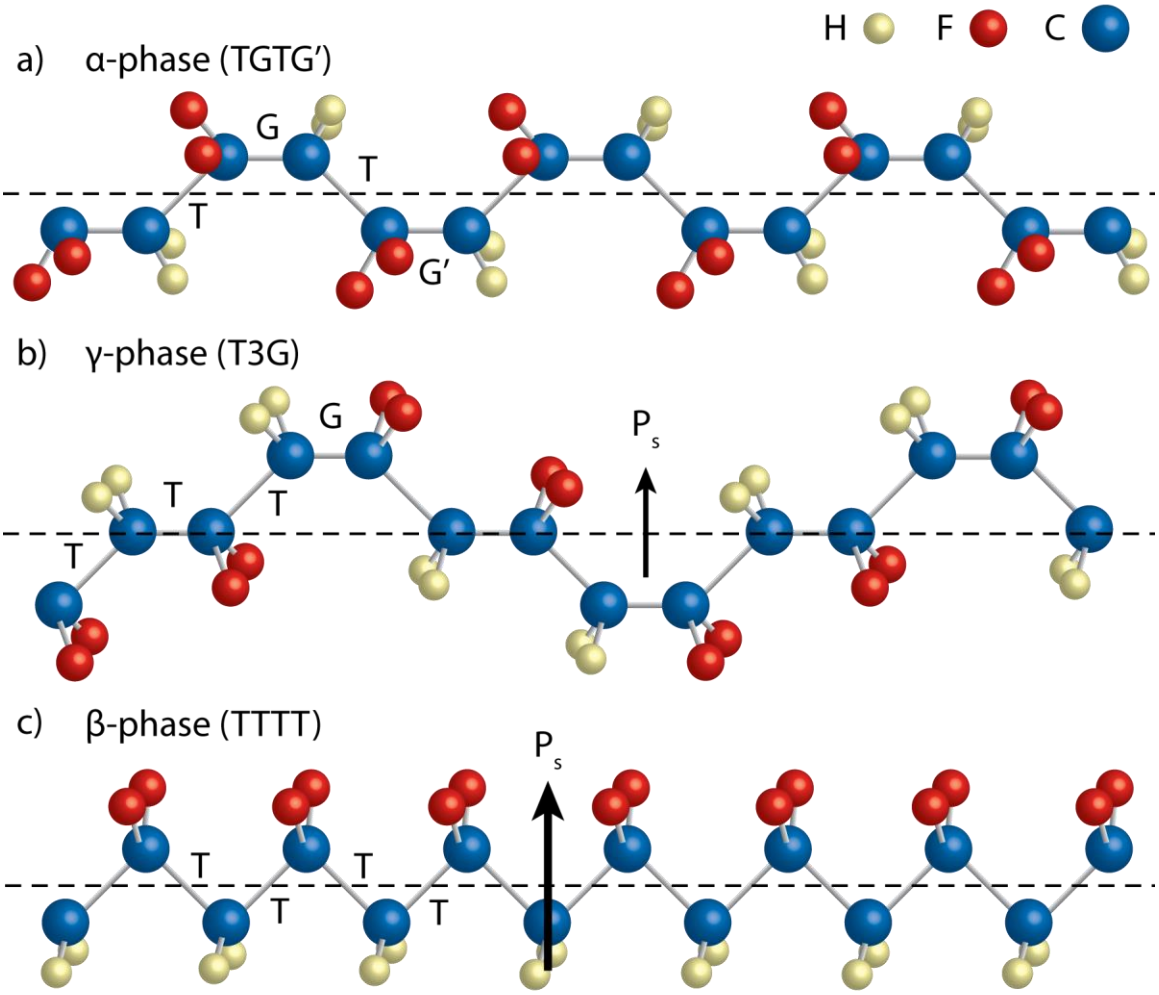

Figure 2.8: Crystalline phases of PVDF polymer. (a) Non-polar α-phase. (b) Polar γ-phase. (c) Highest spontaneous polarization β-phase.

only occurs for the crystalline phases that are polar due to their parallel dipoles, including the β-, γ-, and δ-phases. The anti-parallel dipoles in the α- and ϵ-phases cancel the net dipole moment of the crystal, eliminating any pyroelectric properties. Figure 2.8 shows the crystal structures for the α-, γ-, and β-phases with the dashed line indicating the axis of symmetry. Because the β-phase has the largest spontaneous polarization in each unit cell,

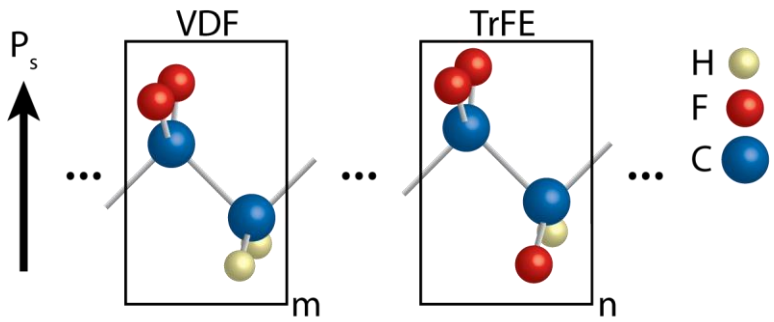

Figure 2.9: Structure of PVDF-TrFE. Trifluoroethylene replaces some of the vinylidene fluoride molecules to form PVDF-TrFE. The molecules are randomly distributed throughout the copolymer and serve as nucleation sites from which β-phase crystals can grow during evaporation of the spin coating solvent.

it exhibits the largest pyroelectric response, making it the most interesting for photodetection applications [102].

Since the non-polar α-phase is the most thermally stable at room temperature, it is preferentially formed from PVDF melts and during spin coating [103-104]. For ease of fabrication, the most desirable methods of inducing β-phase formation should not require additional equipment or machinery. Of interest in this regard are copolymers of PVDF. Figure 2.9 shows a unit cell of VDF with its copolymer trifluoroethylene (TrFE). When polymerized with TrFE, VDF forms P(VDF-TrFE) in which monomer units have a random distribution and the concentration of each can vary. The TrFE content in the copolymer reduces the polarization and thus the pyroelectric response compared to pure β-phase PVDF, but allows the PVDF to preferentially form β-phase to increase crystallinity without the need for additional processing steps [105].

2.6 Flexible photodetectors

The pursuit for active plasmonic devices is not limited to devices with actively tunable plasmon resonances. The established photodetection platforms are built on rigid semiconducting substrates. Therefore another avenue for expanding the capabilities of plasmonic devices is to design them on flexible substrates that would allow them to be used in applications requiring visible transparency, conformal surface coverage, and scalable large-area fabrication. The ideal solution would simultaneously feature high photo-responsivity, fast response time, and a high tolerance for mechanical flexion.

Flexible photodetectors have been studied as a means making adaptive sensor systems for applications requiring conformal shaping [106]. One avenue for producing such flexible detectors is to use solution-processed semiconductors on flexible substrates. Organic semiconductors have been employed to achieve such wavelength-selective photodetection [107]. Velusamy et al. demonstrated transition metal dichalcogenide (TMDC) nanosheet photodetectors with tunable wavelength sensitivity [108]. A bolometer design was implemented by Yildiz et al. showing a thermal detection mechanism can be achieved with high sensitivity on a flexible polyimide substrate without the need for external cooling [109]. Barman and Pal showed that the integration of plasmonic nanoparticles can improved device sensitivity at visible wavelengths while using flexible materials [110]. These demonstrations are important to show the possibilities of flexible photodetection, but truly high performance, flexible detection remains difficult to achieve

due to the lack of highly absorptive, fast responsive materials. Further work is required to balance the requirements of high sensitivity and low response times.

2.7 Summary

Actively tunable photonic devices open the door to applications that can be reconfigured in real time. The tuning techniques discussed in this chapter show significant promise, however, they tend to rely on intrinsic material absorption properties and thus have been either restricted to the infrared regime where small band gaps lead to broad (less spectrally selective) resonances [41, 44-52] or suffer from limitations in regards to reversibility [31, 61-66] and tuning range [31, 57, 63, 64]. Additionally for applications in on-chip light sources, optical switching, and optical computing, an all-optical tuning scheme is highly desirable. Furthermore, plasmonic nanostructures can be used to develop actively tunable emission sources [69-71] and flexible photodetectors [106-110], broadening the application space achievable with plasmonic devices. The remainder of this dissertation addresses the challenges associated with developing actively tunable plasmonic devices.

3. Dynamic tuning of plasmon resonance

3.1 Introduction

Photochromic materials undergo a color change upon interacting with incident light. One such material that is particularly well suited for visible plasmonic tuning is spiropyran (SPI), in part because of its strong response at visible wavelengths [111]. When exposed to ultraviolet (UV) light, SPI undergoes a C-O ring opening reaction that induces a change in its optical properties [112]. This molecular configuration is known as merocyanine (MC) and exhibits a drastically different index of refraction as well as an

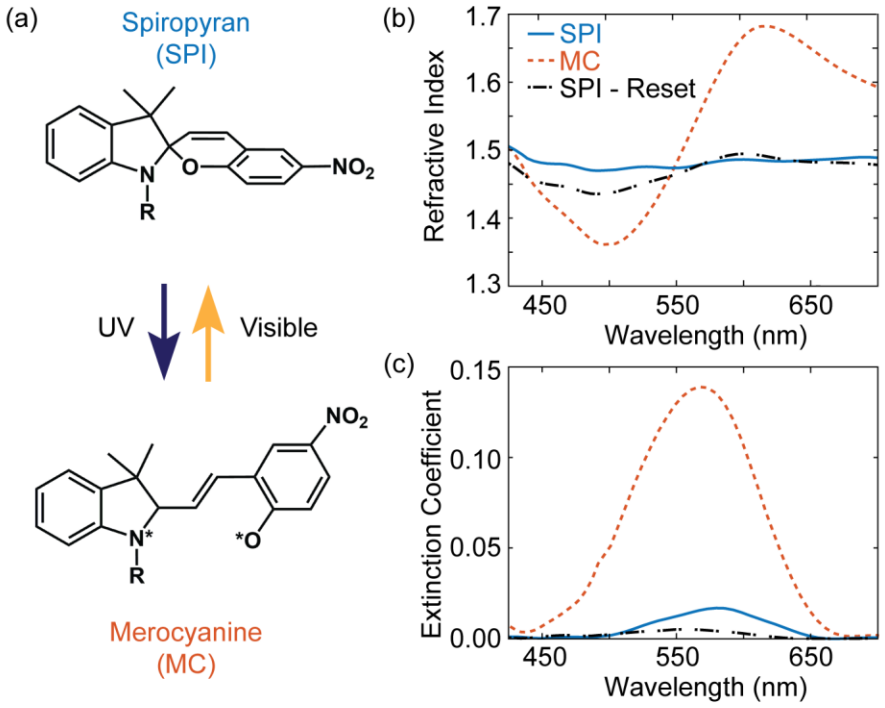

Figure 3.1: Optical Properties of SPI and MC. (a) Chemical structure diagram of SPI (top) and MC (bottom). The reaction can be reset by absorption of visible light or by heat. (b) Refractive index of SPI and MC as measured by spectroscopic ellipsometry. (c) Extinction coefficient of SPI and MC. Adapted from reference [14].

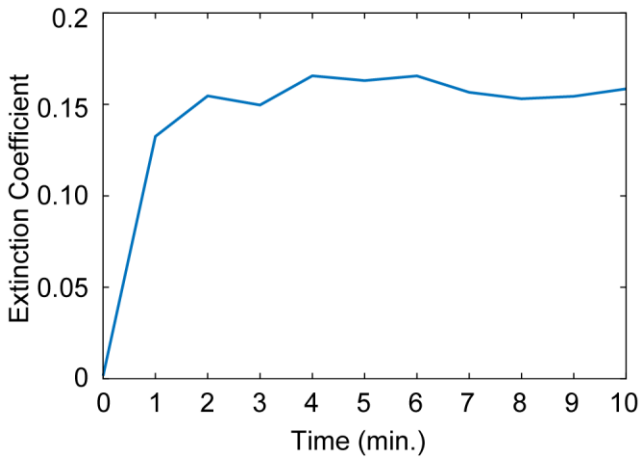

Figure 3.2: UV dose response in SPI thin films. The extinction coefficient was extracted from ellipsometry measurements on a 12 nm SPI-PMMA film. The UV dose was applied by UV-LED at ~1mW/cm^2. Adapted from reference [14].

absorption peak in the visible regime. The process can be reversed by either visible light exposure or heating the molecules to ~70 C [113]. A chemical structure diagram detailing the reaction is shown in Figure 3.1(a). The ability to induce and reverse a phase change with strong optical response using only incident light makes SPI a well-suited material for use in optical switches.

To understand the optical properties of SPI and MC as the photoisomerization process occurs, variable angle spectroscopic ellipsometry was performed on thin films of SPI suspended in a poly(methyl methacrylate) (PMMA) matrix. These measurements allow characteristics of the film such as thickness, extinction coefficient, and refractive index to be extracted as fitting parameters, which were consistent with previously reported results [113, 114, 115-119]. Figure 3.1(b-c) shows the change in the refractive index and

extinction coefficient induced in the SPI-PMMA film upon UV exposure. This data was first reported in Ref. [14].

The changes in optical properties shown in Figure 3.1 were observed after a 10 minute UV exposure dose. To find the minimum exposure dose required to fully isomerize the SPI into MC, ellipsometry was performed at 1 minute intervals during a UV exposure. Figure 3.2 shows that after 1 minute, the extinction rises to ~80% of its maximum value and after 4 minutes it reaches its peak value. In this experiment and in all other optical characterization steps an exposure power of ~1 mW/cm^2 was used because it has been shown to be sufficient to convert the SPI into MC without causing damage to the molecules themselves or to the PMMA matrix [114]. Because the SPI is fully converted to MC in only 4 minutes and there is no discernable sign of damage after 10 minutes, an exposure time is 10 minutes was selected as the safe, effective dose for all further characterization.

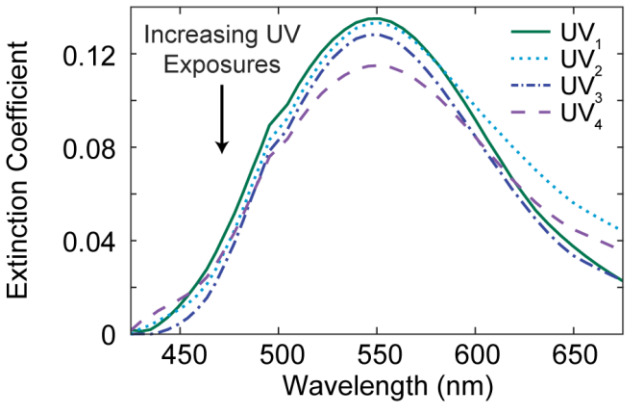

Figure 3.3: SPI response to multiple UV exposure-reset cycles. Each UV exposure was performed by illuminating the entire sample with a UV-LED at 1mW/cm^2 for 10 minutes. The sample was reset by heating on a hot plate at 70 C for 5 minutes.

While a UV dose of 10 minutes at 1 mW/cm^2 is shown not to degrade the SPI, it is important to understand how the switching process degrades through multiple switching cycles. This was shown using ellipsometry measurements taken at each stage of the exposure-reset cycle. Each UV exposure was performed by illuminating the entire sample with a UV-LED at 1mW/cm^2 for 10 minutes. The sample was reset by heating on a hot plate at 70 C for 5 minutes. To make sure the sample was fully reset, ellipsometry measurements were performed between exposures to ensure the extinction coefficient was undetectably low across the visible spectrum, indicating that no MC molecules remained. As can be seen in Figure 3.3, the extinction coefficient drops by 14% after 4 exposure cycles. The fatigue of SPI from UV exposure is a result of side reactions leading to modified molecular structures with a lack of photoresponsive properties, but this deactivation is minimized when SPI is embedded in PMMA matrices [113].

In this section SPI is established as a suitable PCM for use in tunable photonic devices. Its favorable features include the ability to reversibly switch it using only incident light, its strong optical response at visible wavelengths, and its ability to tune through multiple cycles. Section 3.2 describes the sample structure used to evaluate the ability of nanoantennas to optically tune. The optical characterization techniques used for this are detailed in section 3.3. Section 3.4 describes finite element simulations that can be used to discern the physical mechanisms behind the tuning behavior. Section 3.5 discusses these mechanism and explains the observed behavior. Section 3.6 demonstrates the behavior of the same tuning mechanism when used in a metasurface rather than single nanoantennas.

3.2 Sample description

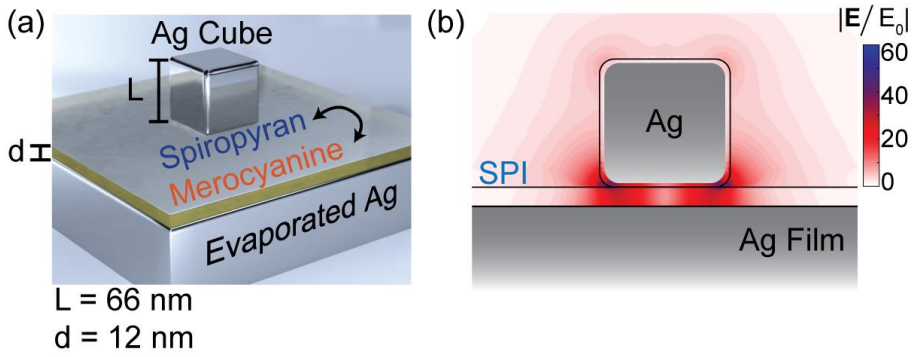

Figure 3.4: Plasmonic nanopatch antenna structure. (a) Device schematic showing geometry and material composition. (b) Electric field profile demonstrating large field enhancement.

The plasmonic nanopatch antennas are comprised of silver nanocubes separated from a silver film by a composite SPI and PMMA spacer layer as shown in Figure 3.4(a). They act as both a small mode volume nanocavity for extreme field confinement and a nanopatch optical antenna for efficient coupling of light to localized plasmons [120]. The fundamental resonance of this structure shown in the electric field profile of Figure 3.4(b) depends strongly on the nanocube size, gap layer thickness, and the dielectric properties of the material in the gap [4, 120, 121]. The 75 nm Ag films were evaporated onto silicon wafers using a CHA Industries Solution E-Beam Evaporator at a deposition rate of 5 Angstroms per second (Å/s). The Ag films were then epoxied (Epoxy Technology EPO-TEK 377) to glass substrates. Due to the poor adhesion of Ag to the native silicon oxide, the Ag films could be template stripped from the silicon wafer producing an ultra-smooth metallic film on the glass substrate. Immediately following the template stripping, the Ag films were coated with a SPI and PMMA solution in anisole before oxidation could damage

the silver film. The total weight of SPI and PMMA dissolved in anisole was 0.5% of the solution weight with a 3:2 ratio of SPI:PMMA. The SPI-PMMA films were spin coated onto the Ag film at 750 rpm for 15 seconds followed by 1500 rpm for 1 minute to produce 12 nm thick films. Excess solvent was evaporated by baking the samples at 70 C for 2 minutes. It was determined that baking at temperatures over 80 C damaged the SPI molecular structure and prevented photoisomerization reactions. A thin ~1 nm adhesion layer was deposited on top by dip-coating the substrate in 3 mM poly(allylamine) hydrochloride (PAH) solution for 5 minutes. Finally, the sample was washed by submersion in a 1 M NaCl solution, rinsed with 18 MΩ de-ionized water, and dried with nitrogen gas. Ag nanocubes were chemically synthesized by NanoComposix Inc. with an average side length of 66 nm and provided in a 1 mg/mL solution. The nanocubes were characterized by SEM to have a ± 5 nm size distribution resulting from the synthesis. A ~3 nm polyvinylpyrrolidone (PVP) stabilizer coating surrounds each cube and reduces oxidation and aggregation. To deposit the nanocubes, 7 μL of a dilute nanocube solution (1:1000 of stock solution to water) was dropcast onto the substrates with the SPI-PMMA and PAH thin films for 15 minutes. This resulted in a disperse distribution of nanocubes over the surface that allowed individual nanoantennas to be addressed within a diffraction limited spot.

3.3 Optical characterization and tuning

To find how the induced changes in the SPI-PMMA film affect the behavior of the nanopatch antenna, scattering spectra were collected before and after UV exposure using the experimental setup shown in Figure 3.5. The setup included a custom dark-field microscope with an EM-CCD camera and a spectrometer to measure the white light scattering from individual nanoantennas. A white light source is coupled into a beam splitter to direct light into a dark-field 100× objective with a high angle of incidence (65 degrees). The scattered light is collected and sent to the EM-CCD camera using a removable mirror mount. Once a suitable nanoantenna is selected, the scattered light is spatially filtered over a spot size of 3 μm and sent into the spectrometer. To isolate the

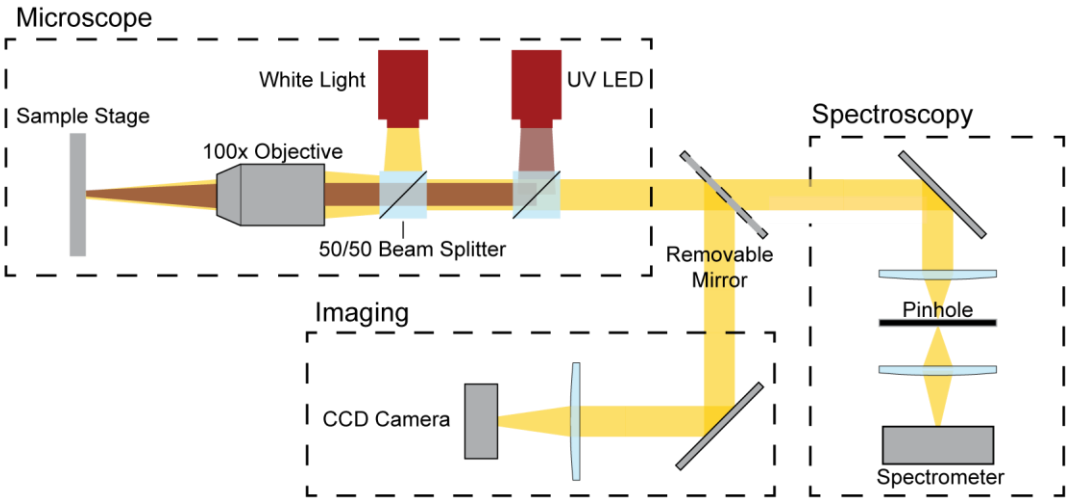

Figure 3.5: Microscope imaging and spectroscopy system. Custom microscope system with a path for imaging and one for spectroscopy. A white light source is used to illuminate the sample to measure its optical response. A UV LED is focused onto the sample to tune the SPI.

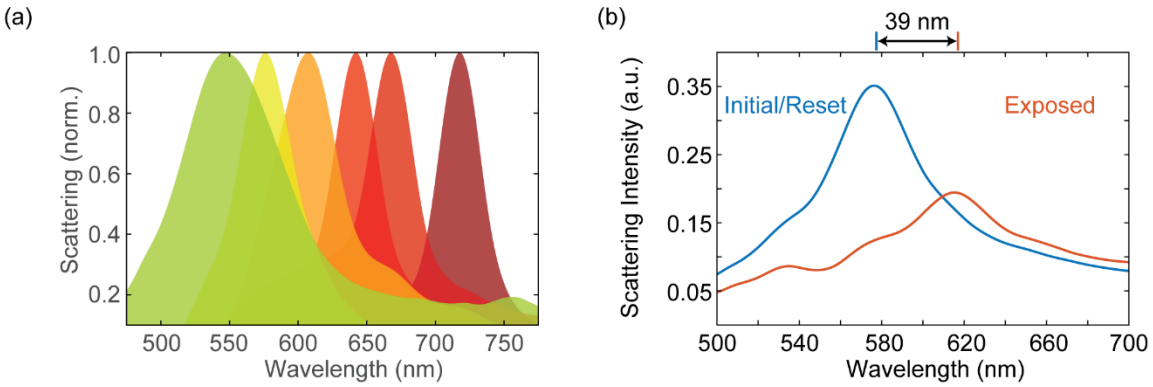

Figure 3.6: Scattering spectra from plasmonic nanopatch antennas. (a) Representative scattering spectra from nanoantennas with varied gap thicknesses. (b) Scattering spectra from an individual nanoantenna before and after UV exposure. Adapted from reference [14].

nanoantenna scattering spectra from the light source, all data was normalized relative to the scattering from a diffuse reflectance standard.

The results of such a measurement are shown in Figure 3.6(a) where clear scattering peaks can be seen corresponding to the surface plasmon resonance of each nanoantenna. The different resonances shown here are a result of changing the thickness of the SPI-PMMA layer. The experimental setup contains a path for a UV light emitting diode (LED) to illuminate the sample over a spot size of 10.6 μm. As mentioned in section 3.1, a UV dose of 10 minutes at 1 mW/cm^2 is sufficient to fully convert the SPI into MC. A representative scattering spectrum from each case is shown in Figure 3.6(b). There is a clear redshift in the peak scattering wavelength upon UV exposure as well as a drop in the scattering intensity.

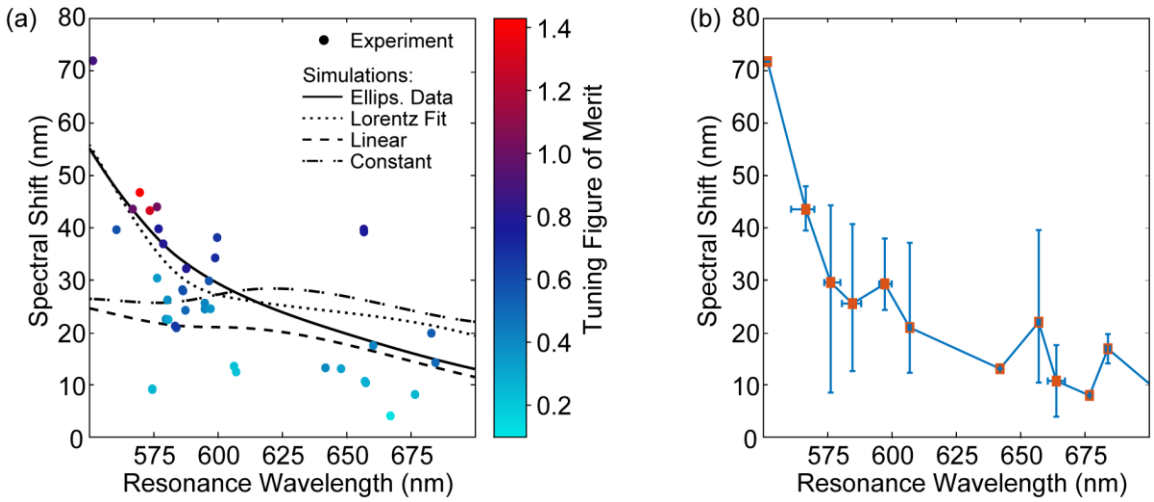

Figure 3.7: Switching behavior of tunable nanoantennas. (a) Experimental spectral shift vs plasmon resonance for individual nanoantennas. The overlaid lines show the spectral shift predicted by finite element simulations using several models for the dispersion in the gap region containing MC dipoles. (b) The same experimental data from (a) grouped to show the average (orange squares) and range (bounding lines) of spectral shift from individual nanoantennas grouped by resonance wavelength. Adapted from reference [14].

To further investigate the switching behavior at different resonance wavelengths, the scattering spectra for 41 individual nanoantennas were taken before and after UV exposure with the results summarized in Figure 3.7. For this investigation, nanoantennas with a fundamental resonance between 550 and 720 nm were fabricated by altering the thickness of the SPI-PMMA film from 2 to 25 nm and through the inherent size distribution of the 66 ± 5 nm silver nanocubes. Through this, the dependence between the tuning range and the gap thickness of the nanoantenna is investigated while keeping the nanocube size fixed within 7.5 percent. Switching data was taken for 41 individual nanoantennas across the visible spectrum. Figure 3.7(a) depicts the experimental data where each point corresponds to a single plasmonic nanoantenna plotted according to its resonance

wavelength and amount of spectral shift observed. Here, spectral shift is defined as the difference between the plasmon resonances – the wavelength where peak scattering intensity is observed – measured before and after UV exposure of the sample. The color of each data point indicates the tuning figure of merit (FOM) for the nanoantenna, defined as the spectral shift divided by the full width at half maximum (FWHM) of the initial resonance. The FOM was selected as a representation of the quality of tuning due to its isolation of the spectral switching properties from the absolute scattering intensity. Figure 3.7(a) shows that as the resonance wavelength is blue-shifted towards 550 nm the spectral shift increases. Furthermore, the FOM is the highest for nanoantennas with a 12 nm film thickness and resonance wavelengths near 570 nm. Thicknesses beyond 25 nm result in nanoantennas that are poorly coupled to the metallic substrate and cannot blue shift the resonance beyond 550 nm. Figure 3.7(b) shows the spectral shift for the same nanoantennas shown in Figure 3.7(a) binned according to initial resonance wavelength. The red squares show the average amount of spectral shift and the error bars show the range in spectral shift (vertical) and resonance wavelength (horizontal) for each bin. Despite the variation in spectral shift, it is clear that as the resonance wavelength is blue-shifted toward 550 nm, the amount of spectral shift tends to increase. This variation is due to inhomogeneity in the distribution of SPI molecules in the PMMA matrix. It is important to note that if the FWHM

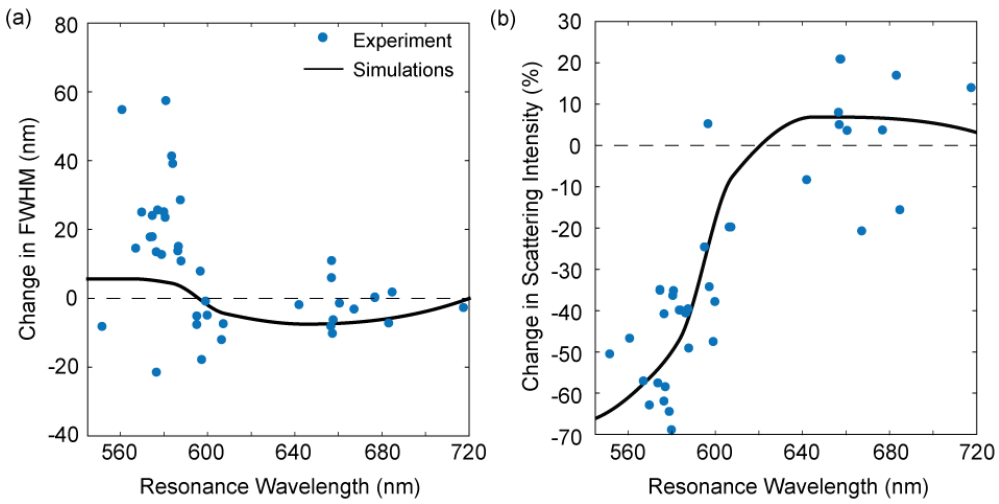

Figure 3.8: Change in scattering profile upon UV exposure . (a) Change in FWHM of the scattering spectra for individual nanoantennas as extracted from fits to a lorentzian distribution. (b) Percent change in scattering intensity measured at the original resonance wavelength.

of the scattering spectrum did not change upon UV exposure, the FOM would be directly related to on/off ratio. However, since the scattering FWHM and the intensity do change upon photoisomerization as shown in Figure 3.8(a-b), the nanoantennas with the highest FOM do not necessarily have the highest on/off ratios. The largest spectral shift and on/off ratio occurs for the nanoantenna with its initial resonance centered at 550 nm, which exhibits 71 nm of spectral shift and 9.2 dB of selectivity. On average the highest on/off ratios, FOMs, and spectral shifts arise from nanoantennas with initial resonances centered between 550-580 nm coinciding with the molecular transition energy of the MC isomer.

This section demonstrates all-optical tuning of a plasmonic nanoantenna's resonance wavelength and scattering intensity. This type of dynamic control over the

optical response of a plasmonic resonator is an important step toward real-time reconfigurable photonic devices.

3.4 Finite element simulations

The scattering from individual nanoantennas was modeled using a commercial finite element simulation package (COMSOL multiphysics). The simulations were performed by my colleague Jon Stewart, allowing me to analyze the simulated data in comparison to the experiments that I personally carried out. The parameters of the simulation were such that they modeled the experimental conditions as much as possible and are reported in Ref. [14]. The incident wavelength was varied to calculate the scattering spectrum for a given nanoantenna side length and gap spacing. The SPI-PMMA or MC-

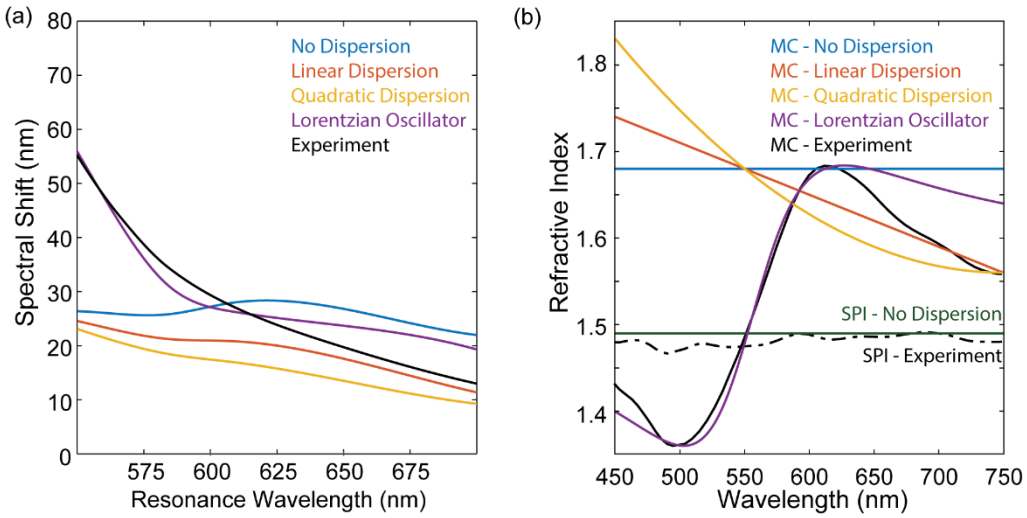

Figure 3.9: Simulated spectral shift of individual nanoantennas. (a) Simulated spectral shift using different models for the dispersion in the MC-doped gap region (b) Dispersion models for MC films used to simulate the scattering profiles for individual nanoantennas [14].

PMMA spacer layers were modeled using various optical constants as shown in Figure 3.9(b).

To study the effect of SPI fill-fraction in the nanoantenna gap region, different film thicknesses and nanocube sizes were simulated in the same manner. For 12 nm SPI-PMMA thicknesses the PVP only accounts for 20 percent of the gap material, while for the 2 nm SPI-PMMA layers the PVP occupies 60 percent of the plasmonic gap. Simulations were performed that varied the fill-fraction while maintaining the same plasmonic resonance. This method isolates the effects of the varying fill-fraction of SPI-PMMA in the plasmonic gaps. The plasmonic resonances were matched in the simulations by comparing 61, 66, and 71 nm nanocubes with the same fundamental resonance by varying the film thicknesses. For instance, the fundamental resonance of a 66 nm nanoantenna with a 5 nm SPI-PMMA layer matches that of a 71 nm nanoantenna with a 6 nm SPI-PMMA layer. Similarly, the resonance is the same for a 66 nm nanoantenna with an 8 nm SPI-PMMA layer and a 61 nm nanoantenna with a 6 nm SPI-PMMA layer. In both cases, the nanoantenna with the highest fill-fraction of SPI-PMMA (i.e. thicker SPI-PMMA films) exhibited larger spectral shifts by nearly 10 percent. Further simulations with 100 percent fill-fraction of SPI-PMMA in the plasmonic gap (i.e. no stabilizer coating) while also maintaining the same plasmonic resonance exhibited the exact same amount of tuning for the 61, 66, and 71 nm cube sizes. As expected the simulations with 100 percent fill-fraction of tunable material exhibited larger spectral shifts than those that included the stabilizer coating, which

introduces a trade-off between increased active material and the protective coating that makes the device more robust for open-air operation.

For further insight into the mechanisms underlying the large experimental tuning, simulations were conducted utilizing varying dispersion models for the refractive index of MC. The simulation results are overlaid with the experimental data in Figure 3.7(a) where the solid and dashed black lines correspond to the scattering simulations for 66 nm nanocubes with 2−12 nm spacer thicknesses and are labeled according to the dispersion profile used for the MC-PMMA refractive indices. The different dispersion profiles are plotted in Figure 3.9(b) along with the simulation results in Figure 3.9(a). The constant dispersion profile uses the largest index change at 615 nm in the ellipsometry data and models the photoisomerization reaction as a constant index change from 1.49 to 1.68 over the entire wavelength range. The linear dispersion profile is similar but accounts for the negative dispersion of the MC not included in the constant dispersion case. Simulations utilizing the ellipsometry data from Figure 3.1(b-c) for the refractive index of the spacer layer agrees well with the observed experimental spectral shifts and on/off ratios. Fitting the ellipsometry data with a Lorentzian oscillator dispersion model similarly results in good agreement with the experimental data. The Lorentzian dispersion model was chosen to enable investigation of the macroscopic effects of dipolar coupling of the MC molecules to the plasmonic mode. The Lorentzian dispersion model is a homogenized material response derived from assuming the material is comprised of many dipoles within a subwavelength volume, which as seen in Figure 3.7(a) is a good approximation for the

dense MC-PMMA photochromic films used in this work. Comparing the simulation results using these four dispersion profiles it is further evident that the nanoantenna tuning does not directly result from a change in refractive index in the gap region. If this were the case, the largest spectral shifts would be expected to occur where the spectral shift is the largest. The experimental and simulated data agree that the largest spectral shifts occur at 550 nm where the change in index is at its minimum. Therefore, resonant coupling is suggested as the mechanism behind the spectral shift for nanoantennas with resonances near 550 nm, as discussed in the next section.

3.5 Resonant coupling

Each experimental scattering spectrum was fit with a Lorentzian profile to extract the peak wavelength and full width at half maximum (FWHM). Upon photoisomerization of the SPI to MC, the plasmonic scattering resonance undergoes changes in absolute scattering intensity and spectral properties such as broadening or narrowing. The change in FWHM upon UV exposure is shown in Figure 3.8(a) and is plotted with results from the finite-element scattering simulations. A majority of nanoantennas with resonance wavelengths below 600 nm exhibit an increased FWHM once the gap material is switched to the MC isomer. Below 600 nm the plasmonic resonance experiences higher losses due to increased coupling to the lossy MC molecules in the gap. For single nanoparticle spectra, these losses damp the plasmons decreasing their lifetime and thus broadening the FWHM of the plasmonic resonance. Furthermore, the increased losses from coupling to the MC

isomers decrease the overall scattering intensity from the nanoantennas depicted in Figure 3.8(b). The largest decreases in scattering intensity occur with nanoantennas with initial resonances below 600 nm, while those with red-shifted resonance wavelengths (i.e. poorly coupled to MC isomers) exhibit only marginal changes in scattering intensity. The characterization of the FWHM and intensity changes through the photoisomerization suggesting that the large tuning exhibited in this work arises from resonant coupling between the fundamental plasmonic mode and MC isomer which can be modeled as a Lorentzian dipole.

To confirm the large nanoantenna tuning at wavelengths near 550 nm, different dispersion models for the refractive indices of spiropyran (SPI) and merocyanine (MC) were simulated in order to find which model best fit the experimental spectral shifts and on/off ratios. Classically, the spectral shift is due to a change in the refractive index. In this case, the largest spectral shifts would be observed where the change in refractive index is highest. As can be seen in Figures 3.7(a) and 3.9(a-b) the best match between experimental and simulated data is achieved when a Lorentzian dipole model is used for the refractive index and extinction coefficient, strengthening the argument that resonant coupling is responsible for the largest spectral shifts.

3.6 Strong coupling with plasmonic metasurfaces

Naturally occurring materials either have weak absorption or produce strong reflections [1]. Thus, the properties of these materials as light absorbers are insufficient for

many modern photonics applications. Nearly perfect absorbers based on metasurfaces with sub-wavelength metallic elements have been developed to address these limitations in spectral ranges from the visible [4], near-infrared [123,124], to microwaves [38]. Top-down lithographic techniques for fabricating these highly engineered materials are limited by the requirements of sub-wavelength metallic elements and the desire for large area scalability. The plasmonic nanoantenna design presented in this chapter consists of a colloidal Ag nanocube suspended over a metallic thin film, separated by a dielectric spacer layer. This configuration is well suited for scalable photonic devices because it can be fabricated with a lithography-free, bottom-up process that can be scaled to truly macroscopic areas [4]. By using colloidally synthesized nanocubes, the difficulty in fabricating sufficiently small nanoparticles by lithography is alleviated with the added benefit of the ease with which they can be deposited onto any electrically charged surface by drop-casting.

The previous sections studied nanoscale light-matter interactions using single nanoparticles. This section expands on this by experimentally investigating the optical response of large ensemble of nanoantennas in the context of spectral tuning of their plasmon resonances. By depositing the nanocubes in a way that more densely covers the metal film, collective action of many nanocubes on the surface creates an effective magnetic response. The impedance of the surface is matched to free space and both reflection and transmission of the surface are eliminated, resulting in complete absorption [125].

Nearly perfect absorbers made of plasmonic nanopatch antennas with a gap region containing a composite SPI-PMMA gap region can achieve absorption over 90% while maintaining an actively tunable absorption peak similar to the tunable scattering peak shown previously in this chapter. Figure 3.10 shows the reflection measured from one such metasurface, normalized to the reflection from a bare silver film. The sample with a resonance at 588 nm, was made of a 12 nm SPI-PMMA layer with a 1 nm adhesion layer and 65 nm Ag cubes over a 75 nm Ag film. The experimental setup used to measure the metasurface reflection spectra was the same setup used in to measure the scattering from single nanoantennas, but with a bright-field objective in place of the dark field objective. To isolate the nanoantenna reflection spectra from the light source, all data was normalized

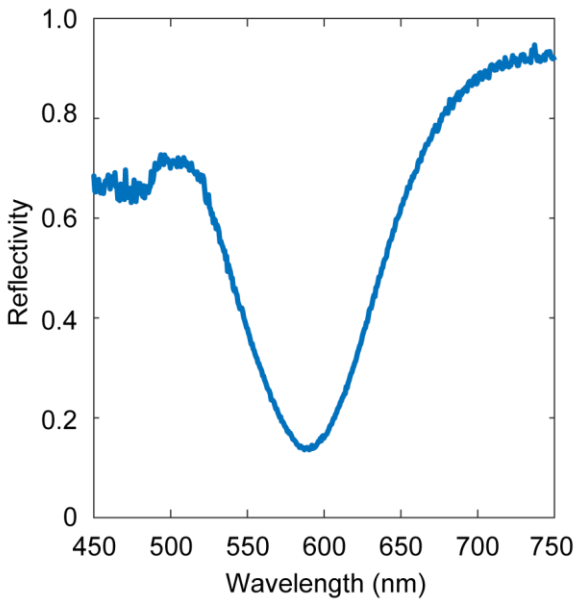

Figure 3.10: Optical response of plasmonic metasurface. The reflectivity is measured on a custom confocal microscope system and normalized to a Ag reflector.

relative to an Ag back mirror. A minimum reflectivity of 10.9% is achieved for the metasurface shown in Figure 3.10.

As with the single particle experiments, a UV LED is used to isomerize the SPI into MC and the reflection spectrum can be measured again to find the change induced. For this study, an exposure dose of 1 mW/cm^2 was used for an interval of 2 minutes. Upon isomerization into MC, the optical response of the metasurface is red-shifted as shown in Figure 3.11(a). By contrast figure 3.11(b) shows a metasurface resonance that has been blue-shifted. When the metasurface resonance wavelength is less than the resonant wavelength of MC (550nm), coupling between the resonant dipoles results in a blue-shift rather than the red-shifts that were seen in the single nanoantenna measurements. An

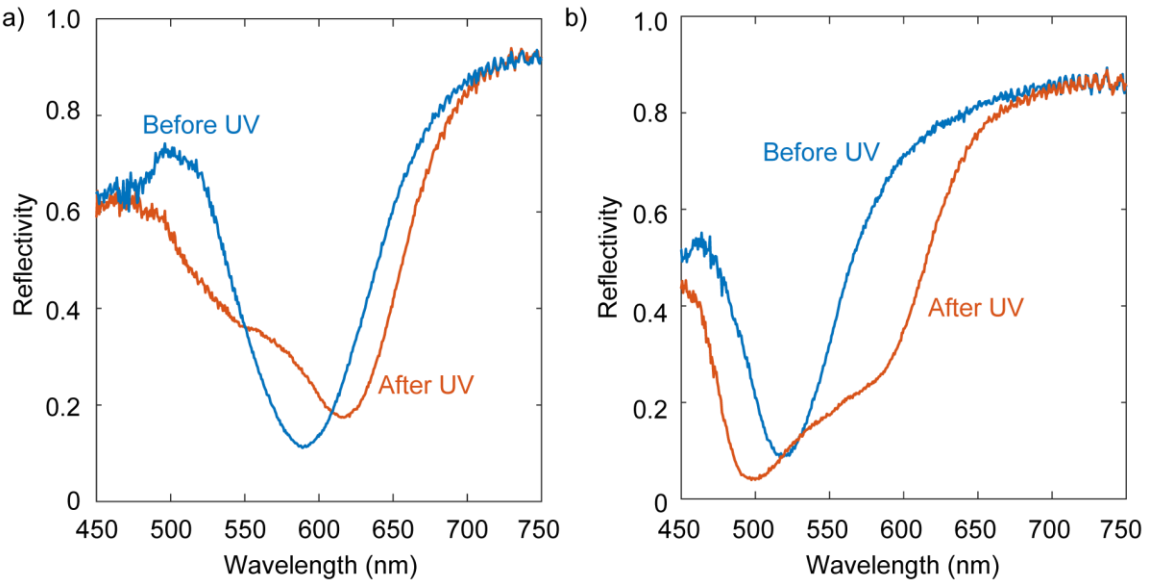

Figure 3.11: Optical tuning of plasmonic metasurfaces. (a) Red-shifted plasmon resonance evidenced by change in the reflection minimum (corresponding to absorption maximum) after UV exposure and conversion of SPI into MC. (b) Blue-shifted plasmon resonance.

interesting feature of the tuned metasurface optical responses is the apparent double peak that is especially prominent when the plasmon resonance is overlapped exactly with the resonance of MC dipoles. The two peaks can be modeled as the combination of two Lorentzian distributions, as shown in Figure 3.12. The two components represent two resonances, one blue-shifted and one red-shifted. As seen from the single-nanocube case in section 3.3, the strength of the coupling increases as the nanoantenna resonance is overlapped with the molecular transition of the SPI. Strong coupling is achieved when the energies of the two dipole oscillators hybridize in such a way that the rate of energy transfer between them exceeds the rates of decay pathways [115, 116]. This phenomenon is commonly modeled as a pair of coupled harmonic oscillators with equations of motion:

$$m_A\ddot{x}_A + k_A x_A + \kappa(x_A - x_B) = 0 \tag{3.1a}$$

$$m_B\ddot{x}_B + k_B x_B + \kappa(x_A - x_B) = 0 \tag{3.1b}$$

where the two oscillators have the eigenfrequencies $\omega_A^0 = \sqrt{k_A/m_A}$ and $\omega_B^0 = \sqrt{k_B/m_B}$ in the absence of coupling ($\kappa = 0$). Solving for the eigenfrequencies of the coupled oscillators ($\kappa \neq 0$) gives:

$$\omega_\pm^2 = \frac{1}{2}[\omega_A^2 + \omega_B^2 \pm \sqrt{(\omega_A^2 - \omega_B^2)^2 + 4\Gamma^2\omega_A\omega_B}] \tag{3.2}$$

where $\omega_A = \sqrt{(k_A + \kappa)/m_A}$, $\omega_B = \sqrt{(k_B + \kappa)/m_B}$, and $\Gamma = \frac{\sqrt{\kappa/m_A}\sqrt{\kappa/m_B}}{\sqrt{\omega_A\omega_B}}$. The coupled eigenfrequencies ω_+ and ω_- are separated when the strong coupling condition is reached. This happens when the frequency splitting, $\Gamma = \omega_+ - \omega_-$, is larger than the sum of the

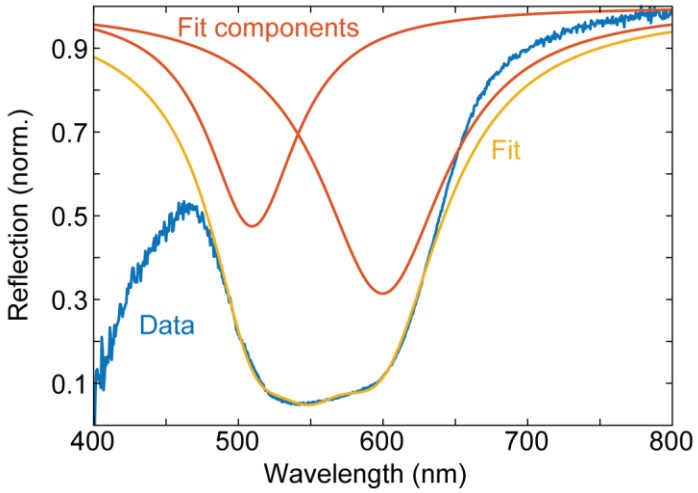

Figure 3.12: Lorentzian fits to metasurface optical response. The fit consists of two Lorenztian distributions. The overall fit is the linear combination of the two components that minimizes the error between the fit and data.

linewidths of the frequency eigenvalues in the presence of damping, indicating that the energy transfer rate between the two hybridized states is greater than the rate of dissipation.

In the case of frequency splitting, often denoted as Rabi-splitting (Ω_R) in coupled systems, the ultrastrong coupling regime is when the amount of splitting is larger than the linewidth of the plasmonic resonator [126]. For SPI in the nanopatch antenna architecture, each side of the split resonance has a half-width at half-maximum (HWHM) of 230 meV at the molecular transition at 550 nm. Therefore Rabi-splitting above ~230 meV would indicate strong coupling between the plasmonic nanocavities and the MC isomers.

In pursuit of such strong coupling, metasurfaces with different resonance wavelengths were fabricated using 65 nm Ag nanocubes over Ag films separated by SPI-PMMA films of varying thicknesses. The peak absorption wavelengths from each case are

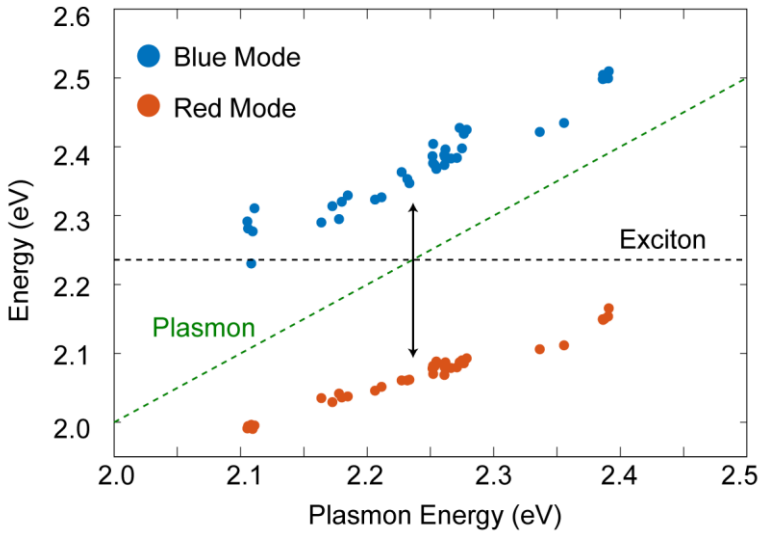

Figure 3.13: Plasmon resonances of a tuned metasurface. The blue mode is the lower resonance wavelength (higher energy) from metasurfaces where the reflectivity dip has been split through strong coupling to MC dipoles in the gap. The red mode is the larger resonance wavelength (lower energy). The exciton energy represents the MC dipole resonance (550nm). The plasmon energy line shows the initial resonance of each metasurface.

plotted in Figure 3.13. When the metasurface resonance was overlapped with the molecular transition of SPI at 550 nm, the single reflection dip splits into two distinct reflectivity dips. As the resonance was detuned from the molecular transition to either side, the characteristic anticrossing behavior of strong coupling is observed. At the molecular transition wavelength the Rabi-splitting is about 300 meV, well into the strong coupling regime.

3.7 Summary and future considerations

In this chapter, I have described dynamic tuning of plasmonic nanoantennas in isolation and as metasurfaces made of ensembles nanoparticles. Spiropyran was chosen as a PCM to tune the nanostructure because of its large optical response at visible

wavelengths. Resonant coupling between LSPRs and the resonant MC dipoles was found to be responsible for the spectral shift in the plasmon resonance. The experimental results show good agreement with finite-element simulations, demonstrating dynamic control over plasmon resonances with an all optical approach. Furthermore, strong coupling was demonstrated between plasmonic metasurfaces and MC molecules, as evidenced by Rabi splitting. This strong coupling could yield larger spectral shifts or faster response times by more efficiently coupling incident energy into the system. The real-time control over the optical response of plasmonic nanoantennas at visible wavelengths promises to enable a new class of dynamically reconfigurable photonic devices. Future research could explore the effect of varying the SPI concentration in the gap region to modify the coupling strength further. By optimizing the gap thickness and nanocube size, absorption closer to 100% could be achieved to increase coupling strength and demonstrate more pronounced switching behavior. A study of the switching time dynamics could yield interesting insights into the limits of the SPI-MC switching behavior. Using this tuning behavior in photonic components could give wavelength-multiplexed optical responses in a single device.

4. Tunable enhancement of emitters

4.1 Introduction

In chapter 2, an overview of plasmonic enhancement of photoluminescence. The long intrinsic emission lifetimes and weak emission intensity make certain fluorescent dyes and quantum emitters ill-suited for high performance nanophotonic devices. Improving absorption and emission efficiency is key to making these emitters faster and brighter for use in devices requiring optimized emission properties. Furthermore, actively tunable emissive properties would be highly desirable for reconfigurable photonic sources. To achieve this, tuning could be applied to a device that enhances either the absorption of incident electromagnetic energy or on that enhances the emission efficiency. Focusing on the latter case, this chapter demonstrates enhancement of the intrinsic emissive properties of fluorescent dyes in pursuit of a plasmonic device with dynamically controllable emissive properties.

The ability to dynamically tune the optical response of a plasmonic metasurface is an important step toward actively reconfigurable photonic devices. By incorporating fluorescent dyes and spiropyran, dynamically tunable emitters can be achieved with an all-optical tuning scheme. Large PL enhancements can be achieved by spectrally overlapping the resonance of the nanopatch antenna with the emission from the dyes. Section 4.2 demonstrates active tuning of emission from fluorescent dyes.

4.2 Tuning emission from fluorescent dyes

4.2.1 Sample description

To incorporate the dyes into the tunable metasurface architecture, a SPI-PMMA film was prepared to allow the metasurface to be optically tuned. The plasmonic nanopatch antennas that comprise the metasurface are silver nanocubes separated from a silver film by a composite SPI and PMMA spacer layer as shown in Figure 4.1. The dyes were deposited by drop casting onto the top surface and allowed to dry completely. The dye emission in aqueous solution is shown in Figure 4.2 [128]. The samples were fabricated with a solution-based, bottom-up process. The 75 nm Ag films formed a reflective back-mirror and were evaporated onto silicon wafers using a CHA Industries Solution E-Beam Evaporator at a deposition rate of 5 Angstroms per second (Å/s). The Ag films were then

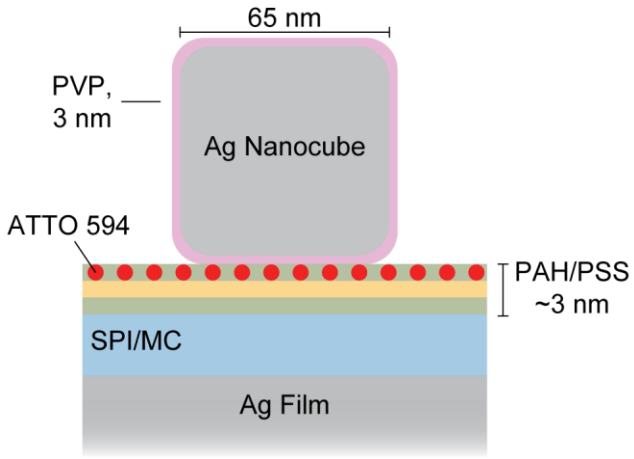

Figure 4.1: Unit cell of the metasurface absorber with fluorescent dyes. The metasurface consists of a nanopatch antenna with the fluorescent dye Atto 594 embedded in the plasmonic cavity. A thin SPI film forms the majority of the gap allowing UV exposure to control the plasmon resonance. The SPI film thickness controls the initial plasmon resonance before UV exposure.

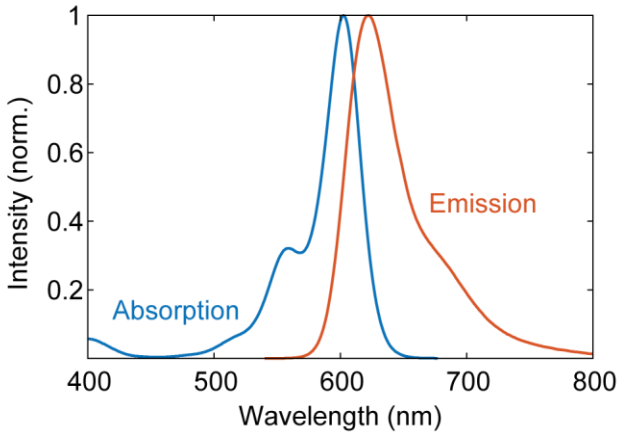

Figure 4.2: Atto 594 absorption and fluorescence in aqueous solution. [128]

epoxied (Epoxy Technology EPO-TEK 377) to glass substrates and template stripped from the silicon wafer producing an ultra-smooth metallic film on the glass substrate. Immediately following the template stripping, the Ag films were coated with a SPI and PMMA solution in anisole before oxidation could damage the silver film. The total weight of SPI and PMMA dissolved in anisole was 0.5% of the solution weight with a 3:2 ratio of SPI to PMMA. The SPI-PMMA films were spin coated onto the Ag film at 750 rpm for 15 seconds followed by 1500 rpm for 1 minute to produce 12 nm thick films. Excess solvent was evaporated by baking the samples at 70 C for 2 minutes. A series of alternating PSS and PAH layers was deposited on top by dip-coating the substrate in 3 mM solutions for 5 minutes for each layer. Between layers, the sample was washed by submersion in a 1 M NaCl solution and rinsed with 18 MΩ de-ionized water. After washing, the sample was dried with nitrogen gas. The fluorescent dye chosen for this work was Atto 594 (Sigma Aldrich) because of its bright optical response at wavelengths where the optical properties

of SPI and MC are well suited for tuning. It was incorporated into the PE layers by allowing 10 µL of a 10 µM solution to dry on the top PE layer surface. Ag nanocubes with an average side length of 65 nm were deposited by drop casting onto the top of the PE layers. For this step, 7 µL of a 4x concentrated nanocube solution (stock solution was 1mg/mL) was dropcast onto the PE thin films and allowed to adhere for 1 hour being washed with DI water. This resulted in a dense distribution of nanocubes over the surface that formed plasmonic metasurfaces.

4.2.2 Optical characterization and tuning

The reflection spectra of the metasurfaces were collected from 400 to 1000 nm using a custom confocal microscope system. A schematic of the system is shown in Figure

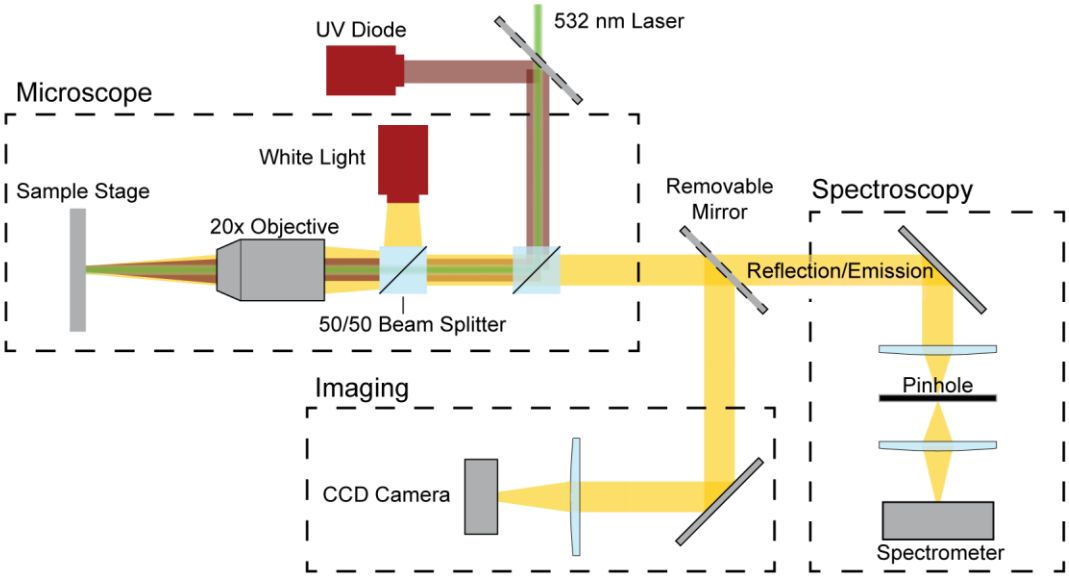

Figure 4.3: Optical imaging and spectroscopy system. The system features a microscope with white light illumination, an imaging system, and a visible-NIR spectrometer. A UV diode is integrated to allow the photochromic samples to be optically tuned.

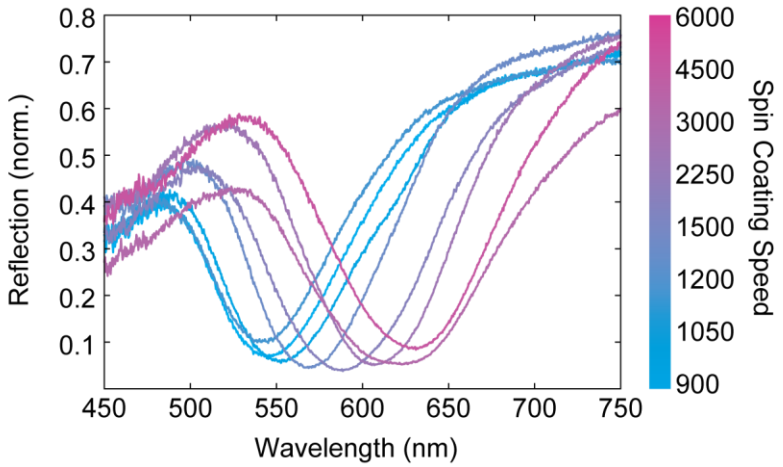

Figure 4.4: Reflection spectra for different spin coating rotation speeds. The plasmonic cavity thickness decreases as the spin coating speed increases which red-shifts the plasmon resonance.

4.3. A broadband white light source is coupled into the microscope and the spectrometer by a 50/50 beam splitter. The metasurface spectra were collected by a CCD camera and normalized to an Ag reflector. The spectra were averaged over a 15 μm spot size using a 20x, 0.4 NA microscope objective and pin-hole aperture inserted in the intermediate image plane. A removable mirror allows the image of the sample to be focused onto a separate CCD camera such that suitable sample areas can be chosen for characterization. Figure 4.4 shows how the metasurface plasmon resonance can be passively tuned by changing the spin coating rotation speed to overlap it with the dye PL peak.

With the dye and SPI incorporated into the plasmonic gap region, dynamic control over the plasmon resonance of the metasurface and emissive properties of the dye can be achieved. To measure the impact that SPI-to-MC conversion has on the emission of the dyes, the reflection from the metasurface and emission from the dyes must be measured before and after UV exposure. The dyes were excited using a 532 nm continuous wave (CW) laser diode. The SPI was tuned to MC in the gap region by exposure to a UV diode for 5 minutes at ~1 mW/cm^2. Figure 4.5(a) shows how the dye's intrinsic emission

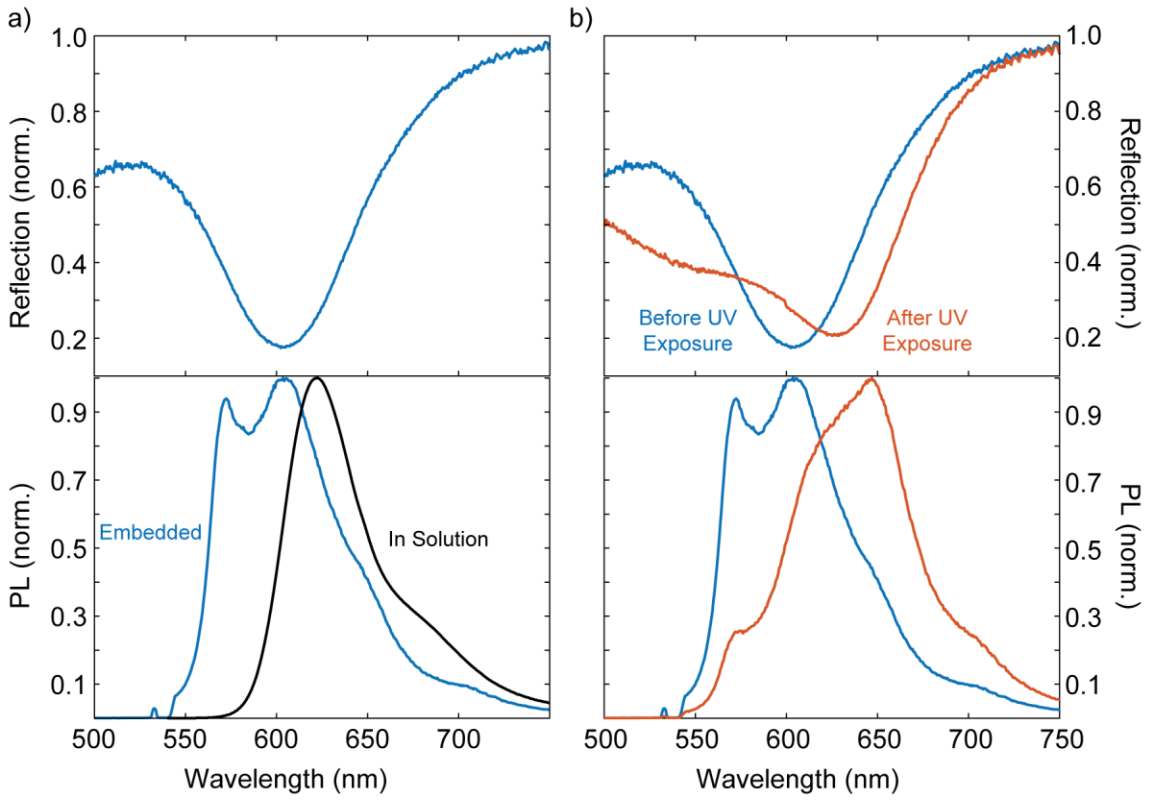

Figure 4.5: Tuning PL spectrum from fluorescent dyes. (a) Metasurface reflection spectrum (top) and PL spectra (bottom) from dyes embedded in the gap region of the metasurface. (b) Reflection spectra (top) before and after UV exposure as the SPI is tuned to MC overlaid with PL spectra of dyes embedded in the gap for each case (bottom).

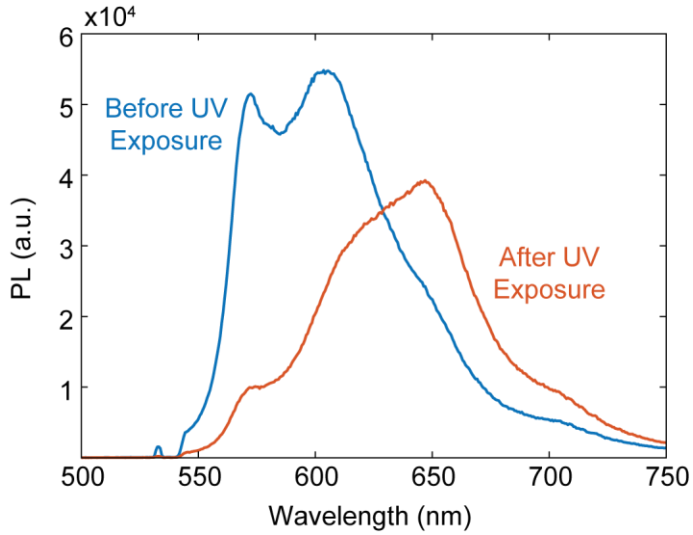

Figure 4.6: Tuning PL intensity . Change in PL intensity due to UV switching of SPI to MC in the plasmonic cavity.

spectrum is altered by the enhanced field strength in the plasmonic gap, increasing the emission at the plasmon resonance so that it shifts the wavelength where peak emission occurs. The effect the UV exposure has on each optical property can be seen in Figure 4.5(b) where exposure to UV light further shift the wavelength where peak emission is observed. The change in emission intensity at particular wavelengths is attributed to Purcell enhancement at the plasmon resonance of the plasmonic cavities. As the plasmon resonance shifts through the emission spectrum of the dye, the wavelength with the highest Purcell factor shifts with it, leading to a change in the peak PL wavelength.

The effect of the plasmonic cavity on the emission intensity is also of interest. With the configuration described here, dynamic control over the emission intensity can be achieved. Figure 4.6 shows the change in intensity that results from UV exposure. The UV

exposure converts the SPI into MC. This phase change introduces an additional energy loss mechanism, as evidenced by the onset of absorption of visible light when MC is in the gap, as shown in chapter 3. The additional losses cause less of the absorbed light to be lost as PL from the dye as it is lost to phononic modes in MC and in converting some of the MC molecules back to SPI [129]. Furthermore, as the plasmonic resonance is red-shifted, there is less overlap between it and the dye's absorption spectrum. This leads to less efficient absorption and thus conversion of incident light energy to radiative decay pathways [69].

4.3 Summary and future considerations

In this chapter, dynamic control over the optical response of a metasurface near-perfect absorber is demonstrated to produce actively tunable emission from fluorescent dyes. Both the spectral shape and intensity can be controlled optically using the nanoantenna platform presented here. Further studies of the emission tuning of the organic dyes would be required to fully understand the nature of their interaction with the metasurfaces. Dynamic control over the PL enhancement and spontaneous emission rate enhancement should also be studied more quantitatively to reveal the full capabilities of the system. Because visible light resets the photochromic reaction in the SPI/MC system, a different dye with an excitation outside of the absorption spectrum of MC might perform better in this system so that exciting the emitter does not reset the resonance shift. Because the active wavelength regime of SPI/MC is restricted, a nonlinear emitter with an excitation wavelength in the NIR and emission at visible wavelengths would be ideal. Another

interesting avenue to explore would be to overlap the resonances of the metasurface and MC isomers with the absorption or emission from dyes to achieve a triply-resonant structure.

5. Pyroelectric polymer for flexible sensing platform

5.1 Introduction

In chapter 2, thermal photodetection is explained and a review is given for its enhancement by plasmonic absorbers. This chapter introduces a design that utilizes a polyvinylidene difluoride copolymer with tifluoroethylene (PVDF-TrFE) thin film and a metasurface absorber in pursuit of a flexible, spectrally selective photodetector. This design leverages the plasmonic nanopatch antenna to give near-perfect absorption at the desired plasmon resonance, ranging from the visible (< 500 nm) to IR (up to 1650 nm). By using PVDF as the pyroelectric detection element, the device can be built through a bottom-up fabrication process on a bendable substrate so that the entire device can be flexible for e.g. wearable applications.

The chapter begins with a description of the device geometry and material components. Section 5.3 discusses the deposition and characterization of PVDF. The following section describes the measurement apparatuses used to characterize the detectors. Section 5.5 details the results from measurements of the detector's spectral response. Section 5.6 discusses the generation of hot electrons and how to mitigate their effects on device performance. Section 5.7 outlines the next steps that should be taken to fully realize a high-performance, flexible photodetector. The chapter closes with a brief summary and considerations for future research directions.

5.2 Sample description

To develop a flexible detector, a design based on well-understood, rigid materials must first serve as the proof-of-concept. The polymer used for this photodetector is PVDF-TrFE, a well-known pyroelectric material [102]. This copolymer of PVDF was chosen because of its commercial availability and widely reported pyroelectric properties [130-136]. The substrate is a conductive p-type silicon wafer with an evaporated gold film on the back to form an ohmic contact. A thin PVDF-TrFE film is deposited on the top surface by spin coating and then heated at 100 C to remove any remaining solvent. The detector area is defined by a 75 nm evaporated metal film that is restricted to a 500 μm radius circle by a shadow mask during evaporation. A spacer layer consisting of several layers of PE layers is deposited by dip coating. On top of the spacer layer, Ag nanocubes of varying sizes are deposited by drop-casting to form a metasurface absorber. A circular cover slip disburses the nanocubes evenly over the sample area in a controlled volume. The plasmon resonance of the metasurface, and thus the wavelength with peak responsivity, is selected by the combination of spacer layer thickness and nanocube size. Figure 5.1 shows the sample structure from mm-scale to nm-scale features.

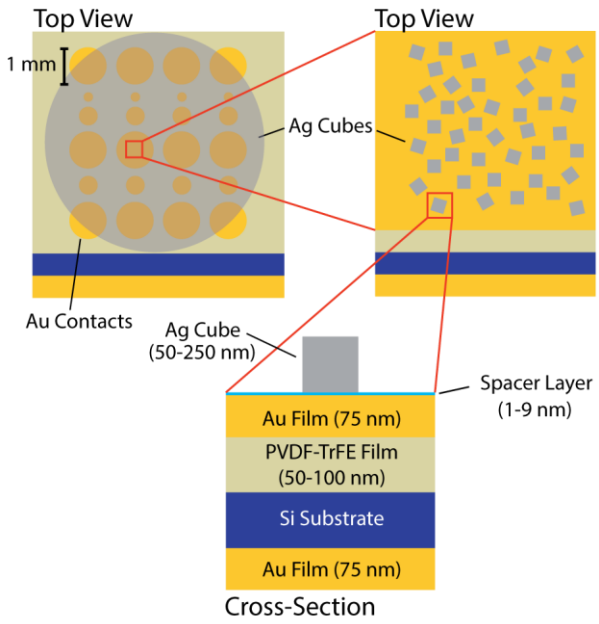

Figure 5.1: Pyroelectric photodetector structure. The Si substrate is coated in Au on the bottom side and PVDF-TrFE on the top. Each sample has 12 circular contact pads defined by the shadow mask during metal evaporation. Each contact pad is coated in a spacer layer and Ag nanocubes to form a plasmonic metasurface.

The Si substrate is conductive, so charge generated through the pyroelectric effect can be collected on its back side with a tungsten probe tip. The 75 nm gold film on the back side is softer than the Si to allow the probe tip to dig in and improve the contacting. The metasurface absorbs incident light energy preferentially at its plasmon resonance. When plasmons are generated by the absorbed light, they are dissipated as heat at the metal surfaces of the Ag cubes and the Au film. Because the nanocubes are surrounded by a protective PVP coating and Ag has lower thermal conductivity than Au, a majority of the heat losses occur in the Au film. The heat generated by this process diffuses through the Au film and into the PVDF-TrFE on a picosecond timescale [90]. As described in section

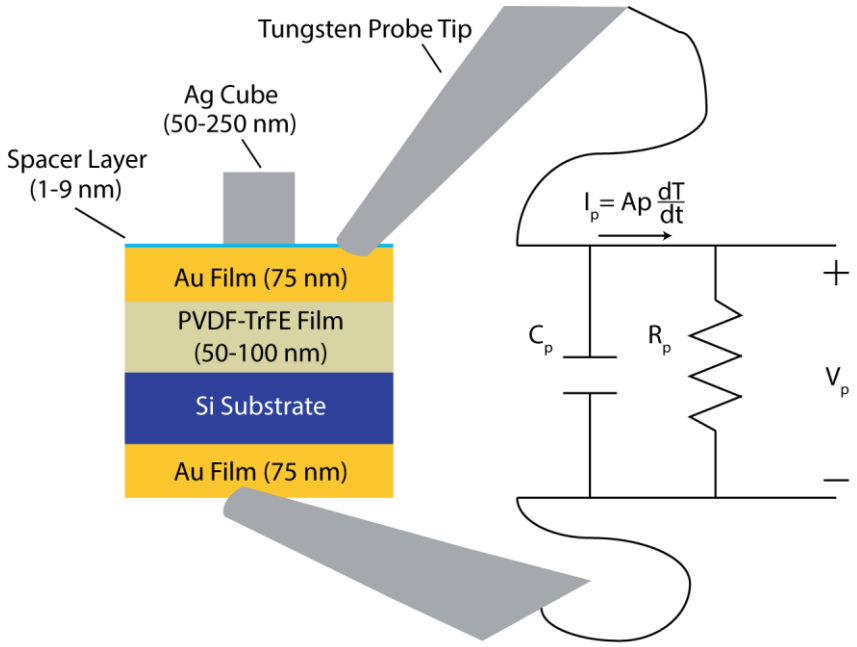

Figure 5.2: Contacting scheme for PVDF-TrFE photodetectors. Tungsten probe tips are used to contact the top and bottom of the sample so that the differential voltage can be measured.

2.5, when the pyroelectric film heats up, its spontaneous polarization decreases, allowing charges trapped at the interface between the PVDF-TrFE and Au films to flow through the detection circuit. Another probe tip is inserted by driving it through the PE spacer layers to contact the Au film on top of the PVDF-TrFE, completing the circuit as shown in Figure 5.2. Before the design parameters can be chosen to optimize performance, careful consideration of the PVDF-TrFE film properties must be taken.

Here the spectral range of operation is defined by the materials and geometry chosen for the plasmonic absorber. For resonances above ~650 nm, Au should be used as the back mirror for the absorber because of its resistance to oxidation and low ohmic losses.

However, for resonances below 650 nm, a different metal must be used because Au starts to absorb the incident light at shorter wavelengths and thus the spectral selectivity of the metasurface is diminished. For these shorter wavelengths, Ag or Al can be used to eliminate the undesired visible light absorption outside of the plasmonic resonance. The limitation with both of these metals is that they oxidize rapidly in air, requiring rapid surface treatment to prevent ambient air exposure. With Au and either Ag or Al, the spectral range spanning those typically covered by Si and InGaAs detectors (400-2000 nm) can be spanned without having to change any parameters affecting the pyroelectric film. The next section explores the effects of the film deposition parameters on device properties and performance.

5.3 Pyroelectric film deposition and characterization

Spin coating deposition of PVDF has been studied extensively, usually as a means of achieving a piezoelectric thin film [98, 99, 137, 138]. The key considerations are typically to encourage β-phase formation to increase the spontaneous polarization of the film and to reduce the porousness of the film to ensure the device is not shorted. As discussed in Chapter 2, β-phase formation is critical as it is PVDF's most polar crystal phase, thus providing the largest pyroelectric response [105]. The film's crystallinity can be evaluated by measuring its Fourier-transform infrared (FTIR) spectrum and looking for the characteristic absorption peaks for certain crystal phases.

To realize the device presented in this dissertation, a few methods for producing β-phase crystals were explored including controlling the temperature of the spin coating environment and adding solute to the PVDF solutions to serve as nucleation sites. There is evidence that by controlling the temperature of the solution and substrate, PVDF can be spun into its β-phase [98, 99]. Elevated temperatures during the spin coating process increase the rate of evaporation, and thus increase the centrifugal force exerted on the thin film by the rotation as it dries on the surface. This stretching force encourages the film to permanently switch from its α-phase to β-phase [137]. To test the effect of the elevated temperature, thin films were spin coated using various PVDF concentration in dimethylacetamide (DMAc) at a constant temperature ranging from 30 C to 125C. The temperature was maintained by heating an Al chuck along with the the sample substrate and solution on a hot plate. The Al chuck held residual heat during the spin coating process. Measurement of the temperature after spin coating revealed that the samples retained the elevated temperature within 3 C after spinning for a total of 30 seconds. After spinning, the samples were dried at 100 C to evaporate any remaining solvent. FTIR measurements revealed that the elevated temperature did not affect β-phase formation with this fabrication procedure, but the solution concentration had a significant impact. Figure 5.3 shows the

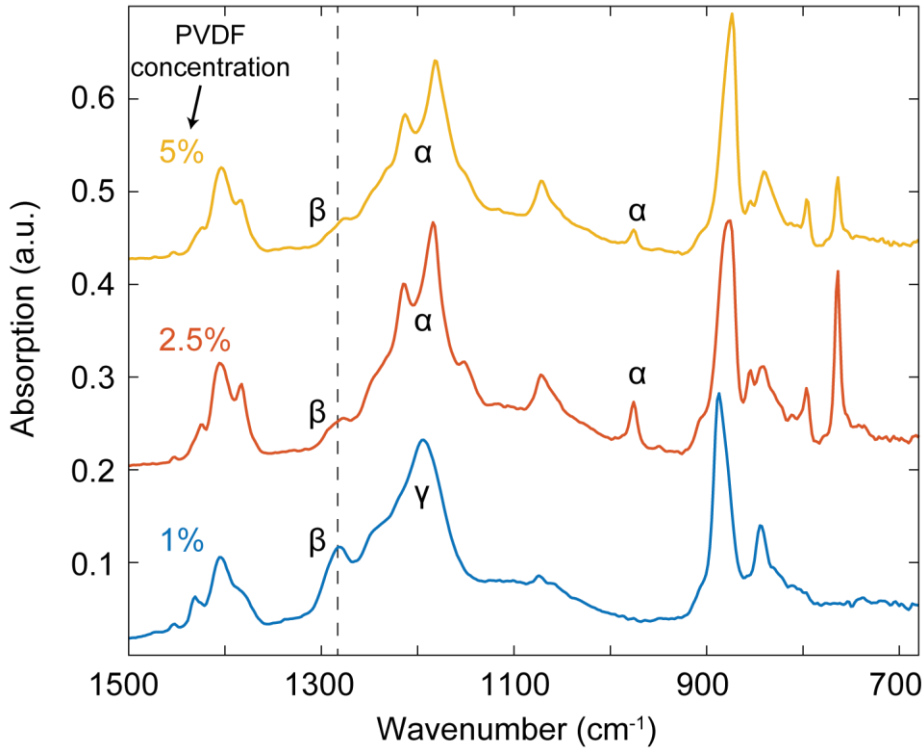

Figure 5.3: FTIR spectra for PVDF films. The films characterized here were spin coated using different solution concentrations. The labels represent characteristic peaks for different crystal phases. The peak at 1280 cm^{-1} shows β-phase formation.

FTIR spectrum for PVDF films made with solution concentrations from 1% to 5%, measured on a Thermo Electron Nicolet 8700 FTIR spectrometer. The blue, red, and yellow lines represent the absorption from films prepared with 1%, 2%, and 5% solutions, respectively. The α- and γ-phases exhibit absorption peaks at 970 cm^{-1} and 1180 cm^{-1}, respectively. The peak at 1280 cm^{-1} is characteristic of the presence of the β-phase in the film [137]. Increasing the solution concentration from 1% to 5% reduced the relative β-phase content as indicated by the reduction in the absorption peak height at 1280 cm^{-1} from 37% to 16%. Table 5.1 summarizes the effect of the solution concentration on β-phase

content. It should be noted that the absolute degree of crystallinity cannot be determined this way, but the relative content of each crystal phase can be compared by comparing the peak heights.

These measurements indicate that lower concentrations, and therefore thinner films, would produce better pyroelectric detectors. However, upon measuring the resistance of the films, those with low solution concentrations had prohibitively low resistances on the order of ~50 Ω. This indicates that they are too porous for use in electrical devices, causing shorts when metal contacts were deposited. The thicker films had higher resistances up to ~2 kΩ, but did not exhibit high β-phase concentrations as shown in Table 5.1 where the average film properties measured for 5 samples are listed for different solution concentrations.

Table 5.1: PVDF film properties.

Solution Concentration (%)	Resistance (kΩ)	1280 cm^{-1} Peak	Thickness (nm)
1	0.05	0.36	10
2.5	1.4	0.20	20
5	2	0.15	50

The thicknesses shown in Table 5.1 are estimated from fits to ellipsometry measurements. For a highly ordered pyroelectric films, the resistance should be on the order of MΩs [139], indicating that these films were too porous for use in a parallel plate

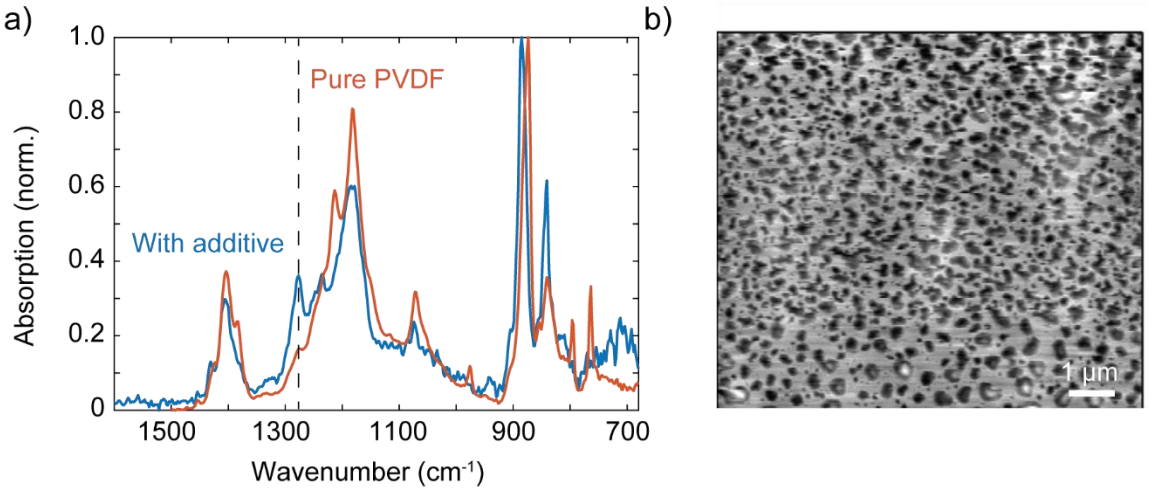

Figure 5.4: Properties of PVDF films prepared with $Mg(NO_3) \cdot 6H_2O$. (a) FTIR absorption spectrum. The blue line corresponds to a film with $Mg(NO_3)_2 \cdot 6H_2O$, the red line is for a pure PVDF film. The dashed black line highlights the characteristic peak of β-phase PVDF at 1280 cm^{-1}. (b) Optical microscopy image of the film where the $Mg(NO_3)_2 \cdot 6H_2O$ can be seen as black spots on the surface.

configuration. The results here indicate that films made with higher solution concentrations must be improved to have higher β-phase content.

Because of the low β-phase content of the thicker PVDF films, different spin coating solutions with additives were used in order to produce thicker films containing higher β-phase content. The first addition to the spin coating solutions used here was $Mg(NO_3)_2 \cdot 6H_2O$, which assists in β-phase formation according to Ref. [137]. The PVDF solution was adjusted from the previous solutions to include 0.2% weight of $Mg(NO_3)_2 \cdot 6H_2O$ powder (Sigma Aldrich). Figure 5.4(b) shows a microscope image of a film where the $Mg(NO_3)_2 \cdot 6H_2O$ can be seen as dark spots on the surface. This is consistent with previously reported results [137]. For these films, concentrations above 5% PVDF and

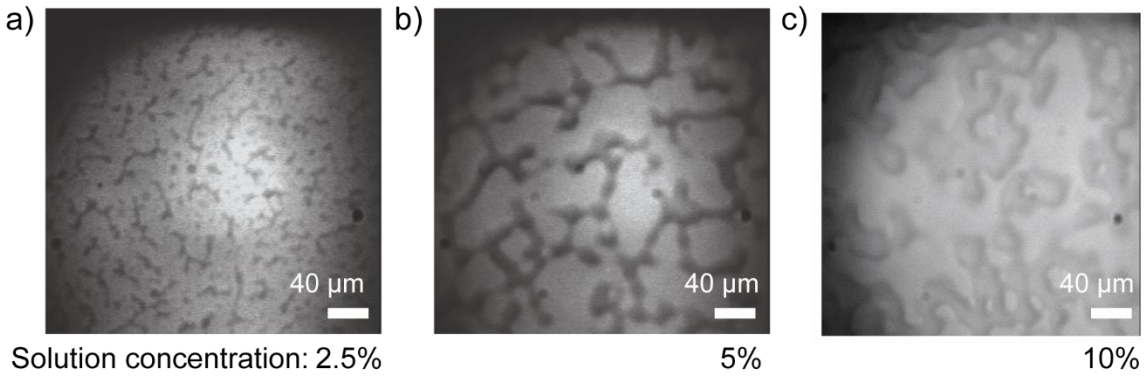

Figure 5.5: Microscope images of PVDF-TrFE films. The films were prepared with varying solution concentrations resulting in island formation.

$Mg(NO_3)_2 \cdot 6H_2O$ were found to be prohibitively viscous as spin coating them did not form films. Therefore films made with concentrations up to 5% were tested for β-phase content using FTIR spectroscopy. The β-phase formation is improved compared to films prepared with only PVDF in the solution, with the absorption at the 1280 cm^{-1} peak rising from 0.16 to 0.35 as shown in Figure 5.4(a). However, the microscope image in Figure 5.4(b) shows deposits of the solution additive which indicates that the film uniformity is not ideal. Since plasmonic devices require a roughness less than a few nanometers to support high quality resonances [69], an additive that mixes in to the film more uniformly is preferable.

To further improve the film quality, PVDF's copolymer with TrFE was studied as an alternative to increase the β-phase content of the films. PVDF-TrFE was chosen because of its commercial availability and widely reported pyroelectric properties [130-136]. Solutions were prepared at 0.25-10% weight of PVDF-TrFE (Solvene 300, Sigma Aldrich) with a 70/30 ratio of PVDF to TrFE. The 70/30 ratio was chosen as a balance between

pyroelectric response, which increases with PVDF content, and β-phase formation which increases with TrFE content. Figure 5.5 shows microscope images of PVDF-TrFE films fabricated with solution concentrations ranging from 2.5% to 10%. The film thickness increases with spin coating solution concentration due to the higher viscosity. Thicker films prepared with higher concentrations exhibited island formation with gaps between them that span 10s of microns. As the concentration is decreased, the islands become smaller with smaller gaps between them. The island and gap size is summarized for each solution concentration in Table 5.2.

Table 5.2: PVDF-TrFE film properties.

Solution Concentration (%)	Film Thickness (nm)	Average Gap Width (μm)	Average Island Width (μm)
2.5	25	8	32
5	70	12	57
10	100	30	50

Island formation is not conducive to using the films in electronic devices because the top metal film will be deposited over the PVDF-TrFE and will come into direct contact with the conductive substrate, shorting the device. The samples prepared with solutions containing 10% PVDF-TrFE produced islands with gaps up to 10s of μm across. Since the metal contacts will be 1 mm in diameter, these gaps are too large for use in electronic devices and the islands are not large enough to contain the whole detector area. To mitigate

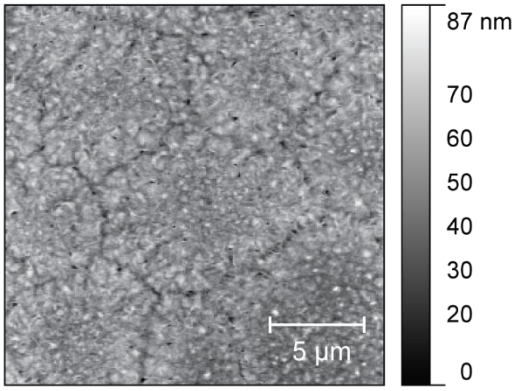

Figure 5.6: AFM image of PVDF-TrFE film. The film was deposited by spin coating with a 5% weight solution onto a clean Si wafer.

this, thinner films having smaller and fewer non-uniformities in the films would perform better in finished photodetectors.

To further characterize the film properties, the resistance was measured with a digital multimeter. For these films the resistance was unexpectedly low at 5-10 kΩ, whereas the resistance of comparable pyroelectric films is on the order of 1-100 MΩ [139]. To investigate if the film was porous which would lead to the low resistance, optical and atomic force microscopy (AFM) were performed. The films used for this were prepared the same way as those used for the pyroelectric detector with a 5% solution concentration. Figure 5.6 depicts the film surface, with grain boundaries being formed. The depth of each grain boundary is on the same order as the overall film thickness, meaning there are areas with no PVDF-TrFE to insulate the two conducting contacts from each other. This explains the low resistance of the samples and indicates that steps should be taken to improve film uniformity and thickness. The large scale variation in thickness is shown in the microscope

images in Figure 5.5, but the AFM image in Figure 5.6 reveals roughness at the nanoscale. The nanoscale roughness is most important for metasurface absorption because it shifts the plasmon resonance of each nanocube away from the average which leads to broader (less spectrally selective) signal from an ensemble of nanocubes.

Since the film will be sandwiched between two conductive plates to form the photodetector architecture, there are a few important film parameters affecting the device capacitance. The standard equation for a parallel plate capacitor given by equation 5.1 shows that the device capacitance is proportional to its dielectric permittivity, $\varepsilon = \varepsilon_r \cdot \varepsilon_0$, and its area, A, which is governed by the size of the top metal contact.

$$C = \frac{\varepsilon A}{d} \tag{5.1}$$

The capacitance is inversely proportional to the distance, d, between the conductive plates. In this case d is determined by the PVDF-TrFE film thickness. The temporal response of the photodetector is determined by the capacitance because it determines the resistance-capacitance (RC) time constant, $\tau = RC$. The thickness of the film can be varied by changing the rotation speed or the solution concentration during spin coating. Thicker films can reduce the capacitance and thus decrease the RC time constant, but the surface roughness tends to be higher in thicker films. The surface roughness needs to be minimized so that high performance plasmonic absorbers can be fabricated on the top surface. The tradeoff between thickness and roughness is highlighted by microscope images in Figure 5.5 where island formation introduces large scale variation in the film thickness.

5.4 Experimental Setup

5.4.1 Optical imaging and characterization

The reflection spectra of the metasurfaces were collected from 400 to 1600 nm using a custom confocal microscope system. A schematic of the system is shown in Figure 5.7. A broadband white light source is coupled into the microscope and the visible to near-IR spectrometer by a 50/50 beam splitter. The metasurface spectra were collected by either a CCD camera (visible) or an InGaAs detector (near-IR) and normalized to a Au film according to:

$$\text{Reflection} = \frac{I_{\text{metasurface}} - I_{\text{dark}}}{I_{\text{reflector}} - I_{\text{dark}}} \tag{5.2}$$

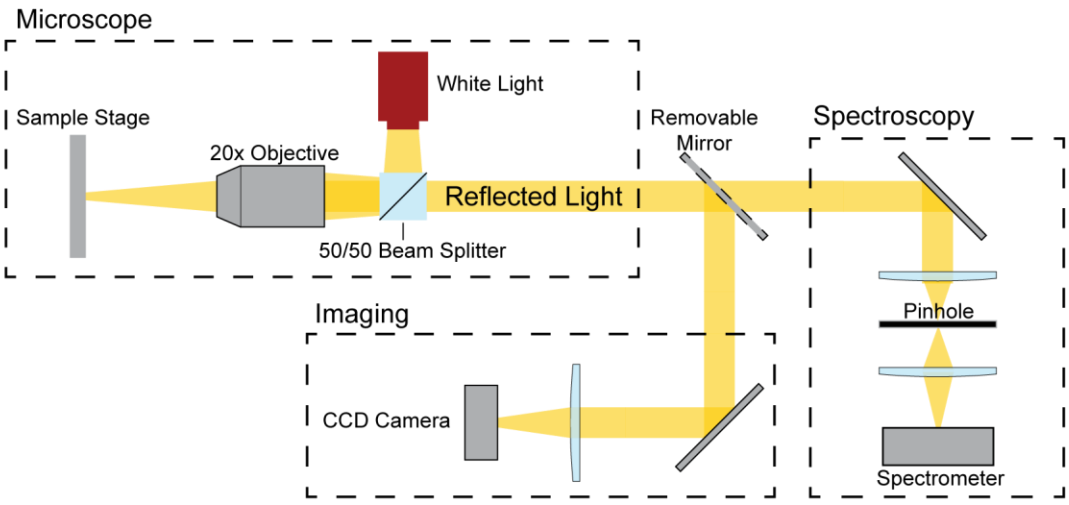

Figure 5.7: Optical imaging and spectroscopy system. Each outlined area serves a different purpose to allow for optical microscopy, imaging, and reflective spectroscopy. A magnetic mirror mount allows the imaging or spectroscopy system to be selected. A pinhole spatially selects the area to be measured by the spectrometer.

where $I_{metasurface}$ is the reflection measured from the sample area that has nanocubes disbursed on the surface, I_{dark} is the signal measured on the spectrometer when the white light source is turned off, and $I_{reflector}$ is the reflection measured on a sample area that has the Au film without nanocubes. Normalizing in this manner isolates the reflection spectrum of the metasurface absorber from the influence of the light source and optical components in the measurement system. The spectra were averaged over a 15 μm spot size large enough to collect the signal from an ensemble of nanocubes using a 20x, 0.4 NA bright-field objective and pin-hole aperture inserted in the intermediate image plane. A removable mirror allows the image of the sample to be focused onto a separate CCD camera such that suitable sample areas can be chosen for characterization.

5.4.2 Responsivity measurements

A schematic of the responsivity and temporal response measurement setup is shown in Figure 5.8. The sample is mounted on a 3-dimensional motion stage so that the detector area can be moved in and out of the focal plane of the laser through the objective. A variable ND filter with a motor to control its rotation allows for remote control of the laser power through the system. The beam passes through a chopper wheel to enable modulation at the frequency set by the chopper wheel motor. A modulation frequency of 113 Hz was selected because it is a prime number far enough away from common frequencies used in electrical power transport to avoid noise from the electrical systems in the room and any of their harmonics. A reflective microscope objective consisting of two reflective surfaces within the body of the objective was chosen so that the beam path does not change significantly

when selecting the laser wavelengths from 400-2000 nm. Because the reflective objective cannot pass the entire beam through the optical axis as it will be blocked by its central mirror, the beam must be expanded such that its edges fill the passable area of the objective. To expand the beam, it is sent through an elliptical mirror and reflected back to re-collimate. This is used instead of refractive optics so that the beam path is not affected by

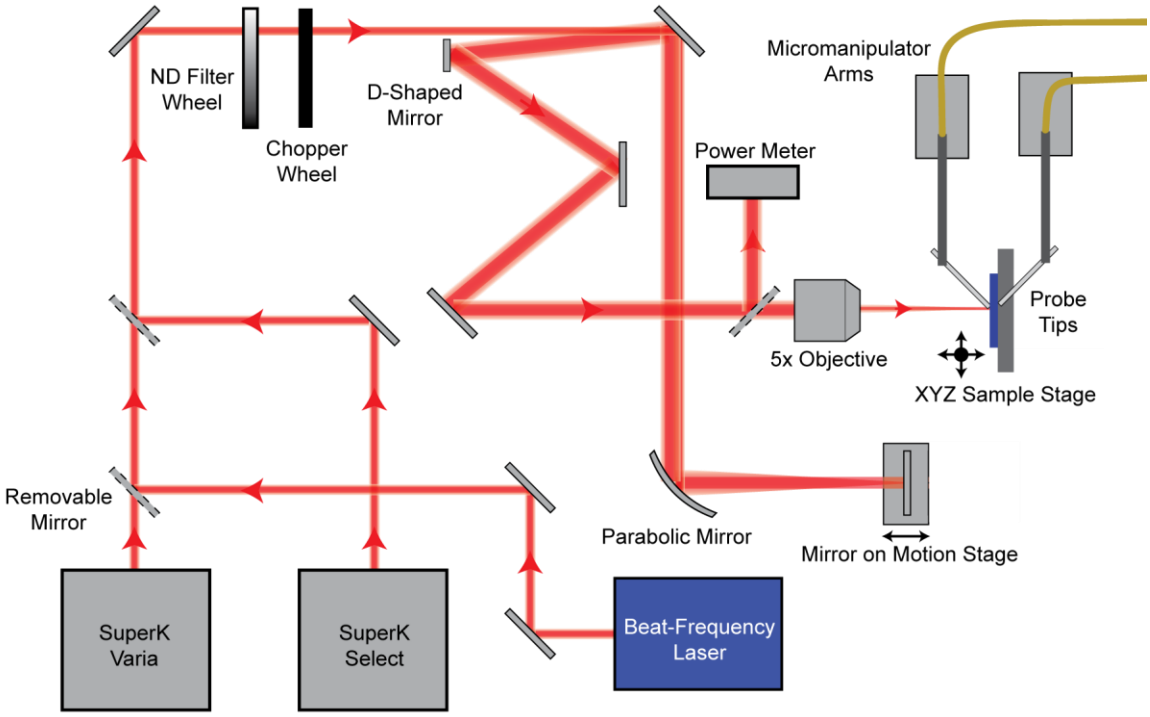

Figure 5.8: Spectral and frequency response measurement setup. The beam path is defined is defined by the red lines and the beam size is approximated by their thickness. Three lasers are available for use, with the SuperK filters used for the spectral response and the beat-frequency laser used for the frequency response. A variable ND filter and power meter are used to stabilize the average power at each wavelength measured. A chopper wheel modulates the laser signal to allow the pyroelectric films to heat and cool. An elliptical mirror and D-shaped pickoff mirror are used to expand the beam diameter. A reflective, infinity-corrected objective is used to focus the beam to fill the detector area. Micromanipulator arms and tungsten probe tips are used to contact the sample.

tuning the laser wavelength. A D-shaped mirror is cutoff on one side to allow the original beam to pass while redirecting the slightly off-axis expanded beam into the measurement beam path. A flip mirror allows the beam to be picked off and sent to a power meter. A custom Labview program controls the various components and allows that measurement process to be automated. The sample is contacted with two tungsten probe tips with the leads connected to a differential voltage amplifier, the output of which is connected to the input of a lock-in amplifier. The lock-in amplifier uses the frequency signal from the chopper controller as its frequency input.

The system is designed to perform automated wavelength sweeps to measure the spectral profile of the responsivity. A measurement cycle allows the detector to be heated by the chopped laser beam, generating a modulated pyroelectric signal. The signal is measured by the lock-in amplifier and recorded in Labview. The beam is then redirected away from the sample by the flip mirror and the charge is allowed to accumulate on the sample surface. The laser is tuned to the next wavelength and the next measurement can begin. It is critical that the laser power is stabilized between measurements because the pyroelectric coefficient is temperature dependent and therefore the detector will be more or less sensitive depending on the incident laser power. The incident power is controlled by rotating the variable ND filter until the power meter reads the desired level, typically on the order of 10s to 100s of μW, depending on the sensitivity of the detector. Before the lock-in amplifier, a low or high impedance pre-amplifier is used to measure the current or voltage responsivity, respectively. The voltage output from the pre-amplifier is connected

to the input channel of the lock-in amplifier and is divided by the incident power to calculate the responsivity.

5.5 Spectral response

To capitalize on the advantages of pyroelectric detectors, namely the decoupling of the pyroelectric sensing element from the spectral response, detectors with varying plasmon resonances were fabricated on PVDF-TrFE films. A first attempt at demonstrating a pyroelectric response was performed using the device structure shown in section 5.2. The metasurface absorber consisted of a 75 nm Au film serving as the detector contact pad separated from 100 nm Ag nanocubes by a ~5 nm spacer layer of alternating PAH and PSS films, corresponding to a targeted plasmon resonance of 780 nm. The PVDF-TrFE film was spin coated at 2000 rpm for 30 seconds using a 2.5% weight solution in DMAc. Figure 5.9 shows the voltage responsivity of a representative photodetector overlaid with the reflection spectrum of the integrated metasurface absorber on the surface of the detector. The large FWHM and low off-resonance reflectivity of the spectrum can be attributed to oxidation of the Ag nanocubes after their protective PVP coating degraded from prolonged

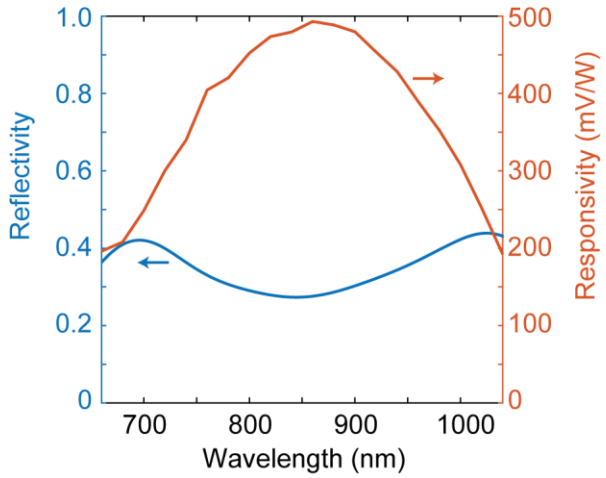

Figure 5.9: Spectral response of PVDF-TrFE photodetector. The blue line corresponds to the metasurface absorber's reflection spectrum. The red line corresponds to the detector's responsivity spectrum.

exposure to air. All subsequent samples were stored in a vacuum chamber to prevent such damage. From this measurement, a clear overlap can be observed between the plasmon resonance of the metasurface and the peak photoresponse of the detector. The incident laser power was stabilized at 100 μW for each wavelength and the photoresponse was measured with an integration time of 1 second to allow the lock-in amplifier to phase-match the signal.

To show control over the photoresponse, more detectors were fabricated with different plasmon resonances corresponding to each combination of nanocube size and spacer layer thickness. For these samples, a higher PVDF-TrFE solution concentration was used in attempt to improve film quality. Figure 5.10 shows the reflection spectra and pyroelectric responses of several representative detectors. They were fabricated with 5 PE layers and nanocube sizes from 75 nm to 100 nm, producing plasmon resonances from 677

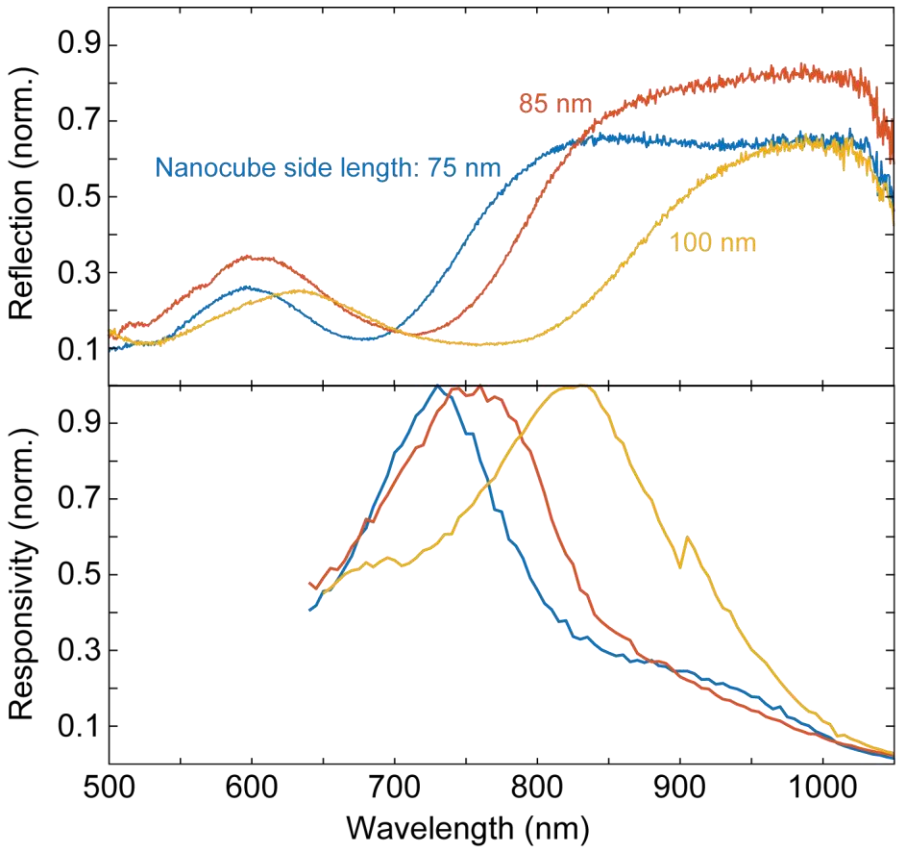

Figure 5.10: Optical and pyroelectric response of PVDF-TrFE photodetectors. (Top panel) Normalized reflection spectra of detectors made with different nanocube sizes. (Bottom panel) Normalized responsivity of each detector.

nm to 761 nm. Clear peaks in the responsivity can be seen corresponding to the plasmon resonances in each case. However, it was observed that the responsivity peaks were red-shifted from the plasmon resonance for all of the detectors measured. The red shift is a result of complex dynamics influenced by a conduction current brought on by the low resistance of the detectors and scattering by the rough sample surface.

5.6 Hot electron generation

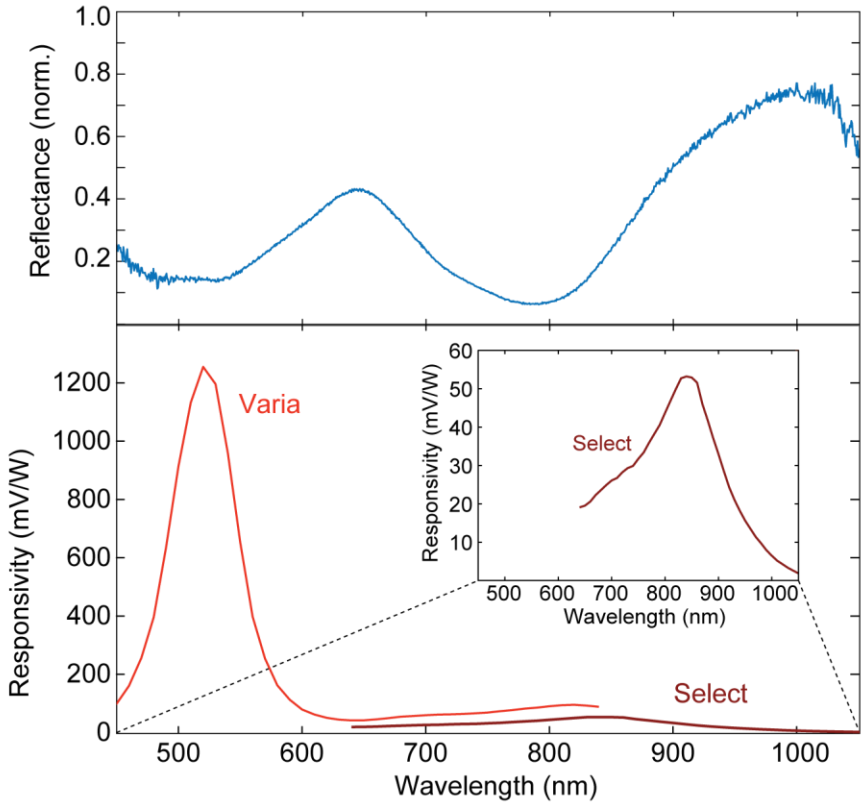

Figure 5.11: Photoresponse of pyroelectric detector under visible illumination. (Top Panel) Normalized reflectance of plasmonic metasurface. (Bottom panel) Responsivity spectra measured with two different lasers. The Varia emits from 400 to 840 nm, the Select covers the range from 640 to 1100 nm. The inset shows the responsivity measured with the Select, enlarged to show the peak that corresponds to the minimum reflectance at the plasmon resonance.

One of the biggest challenges encountered during the measurements described above was the generation of hot electrons in the Si substrate. Figure 5.11 shows the spectral dependence of the responsivity for a representative detector when illuminated by visible (SuperK Varia) and near-infrared (SuperK Select) lasers. There is a slight difference in the spectra from each laser because they have different spectral bandwidths. The dominant

peak around 510 nm persists when the top metal contact is varied between Au, Ag, and Al, indicating that the phenomenon responsible for the signal is dependent only on the substrate properties. By isolating the near-infrared spectrum, a peak in the responsivity can be observed, corresponding to absorption in the plasmonic metasurface covering the detector. Hot electron generation can be mitigated by evaporating a metal film between the PVDF-TrFE and Si that will reflect all incident light such that any light transmitted through the metasurface or scattered around it cannot thermally or electronically excite electrons in the Si.

Due to equipment failures, a different metal evaporation chamber was used to make samples on identical PVDF-TrFE films (switched from CHA Industries Solution E-beam to Kurt Lesker PVD 75). The PVD 75 system is unable to achieve vacuum pressures below ~2e-6 kPa, while the CHA Industries evaporator can pump to pressures below 5e-7 kPa. The higher pressure in the second round of evaporations yields rougher metal films. In

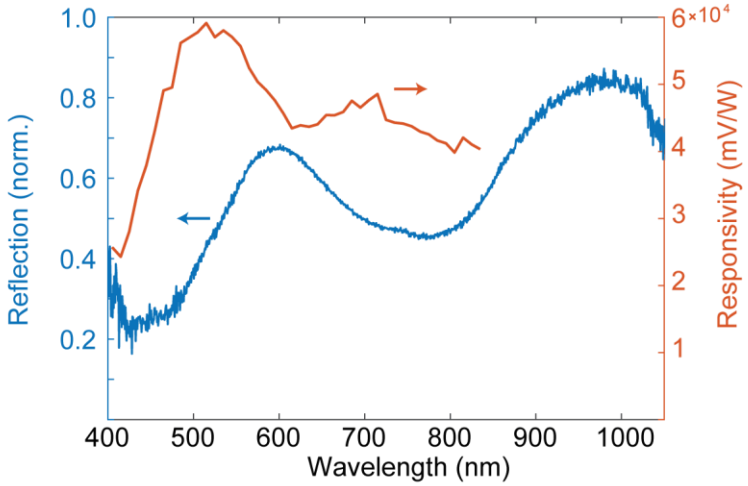

Figure 5.12: Response of photodetector fabricated at higher vacuum pressure.

general rougher films produce metasurfaces with broader and shallower resonances. Therefore, samples made with metal contacts deposited at higher vacuum pressures exhibited weaker absorption and no obvious pyroelectric response, as shown in Figure 5.12.

5.7 Next step experiments

The results shown so far are encouraging steps toward realizing a high performance, flexible pyroelectric photodetector. However, due to the unprecedented impact of the coronavirus, the remaining characterization and design required to demonstrate a flexible detector were unfinished. This section outlines the immediate steps that should be taken to complete the initial demonstration of the flexible detector.

5.7.1 PVDF-TrFE film deposition

In order to address the porous, conductive nature of the previous PVDF-TrFE films, steps must be taken to fabricate highly ordered, uniform pyroelectric films. The first evidence of a crystalline pyroelectric film is that its resistance is on the order of 10s to 100s of MΩ. Resistances in this range indicate that the film is not porous and less likely to suffer from the influence of hot electrons on the output signal. To improve the film quality, thinner films will be tested to provide better surface coverage, as shown earlier in this chapter. Another method to improve the crystallinity, uniformity, and resistance is to electrically pole the spin coated films while they dry under heat. Previous research suggests that corona poling allows polymer chains to orient themselves according to the external

electric field, resulting in higher spontaneous polarization and pyroelectric response [140]. If high quality films cannot be achieved with a simple spin coating process, commercially available PVDF-TrFE films that have been poled and proven to have excellent electrical and pyroelectric properties can be used in the same device design.

5.7.2 Spectral response

Once high quality PVDF-TrFE films have been obtained either through purchase or in-house fabrication, the first goal will be to demonstrate a large spectral range of operation. Because the responsivity has no dependence on the wavelength of incident light, the photodetector operational range is not limited to a particular spectral regime. Therefore, to capitalize on the unique advantages of thermal photodetection, plasmonic metasurfaces will be fabricated on various metal films to allow their resonances to span the visible, NIR, and well into SWIR wavelength ranges. Recent advances in the Mikkelsen group have demonstrated the ability to synthesize colloidal Ag nanocubes with side lengths as low as 36 nm. Commercially available nanocubes can reach side lengths up to 250 nm. With this size range, wavelengths from <450 nm to >2000 nm, surpassing what is available with either a Si or InGaAs detector.

The goal of spanning a wide wavelength range is to show control over the spectral response of the detectors by tuning the nanocube size and spacer layer thickness (by changing the number of PE layers). To achieve strong enough coupling between the nanocubes and the metal film for near perfect absorption, a maximum spacer layer thickness of ~10 nm can be used. Thicker spacer layers and smaller nanocubes each

produce blueshifted resonances. Therefore, the smallest resonance wavelength achievable with this detector design will occur with nanocubes with 36 nm side length and 9 PE layers, beyond which near-perfect absorption is lost due to decoupling of the nanoparticle with the metal film. Thinner spacer layers and larger nanocubes produce longer resonance wavelengths. Therefore the nanocubes with a 250 nm side length paired with a spacer layer consisting of a single PE layer would produce the longest resonance wavelength with this fabrication process. These two cases define the bounds of the lithography-free fabrication process outlined in this chapter, but any arbitrary wavelength within this range can produce a large pyroelectric response by varying the nanocube size and gap thickness.

5.7.3 Frequency response

The temporal response of the detector can be measured in the same setup described for the spectral response measurements. In this measurement, the laser source is switched to a beat-frequency laser system consisting of two lasers operating at different tunable repetition rates where the output is modulated at the difference of the two repetition rates. This gives control over the repetition rate, allowing the photodetectors to be modulated at the desired repetition rate. The lasers output at 780 nm and the same electrical measurement scheme is used as in the responsivity measurements. The laser repetition rate is set to a low frequency and the detector response is measured. The repetition frequency is increased and

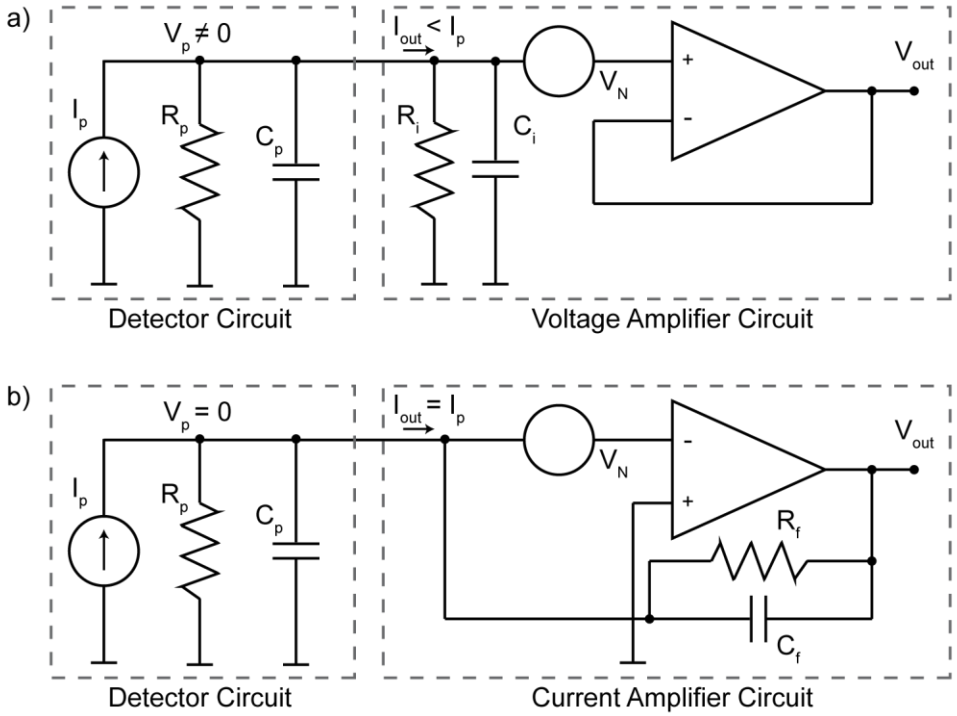

Figure 5.13: Pyroelectric photodetector readout circuits. (a) Detector connected to a voltage pre-amplifier. (b) Detector connected to current pre-amplifier.

the response is measured again. This response is repeated until a repetition rate is reached where the detector signal level drops by 3 dB, defined as the band width of the detector.

There are two methods available for the readout circuit. Figure 5.13 shows the readout circuits for this device using a high- (a) or low-impedance (b) amplifier. The distinction between them is the readout circuit resistance and capacitance, and is important when measuring the bandwidth of the device. The transfer function, $Z = V_{out}/I_{out}$, in each case can be obtained from the resistances and capacitances in each circuit [139]. Figure 5.13(a) depicts the voltage amplification mode in which the device accumulates surface charge until it is heated by incident light. When a pyroelectric current begins to flow as the

device's spontaneous polarization decreases, a potential difference is generated across the load resistor, R_i. The amplifier noise voltage, V_N, is added to the signal output. Imperfections in the device yield a parasitic capacitance and resistance that allow some charge to flow through it and cause the output current to be less than the total pyroelectric current. The impedance of the circuit can be expressed as [139]:

$$Z(f) = \frac{R}{1 + i\frac{f}{f_0}} \tag{5.3}$$

$$R = \frac{R_p R_i}{R_p + R_i} \tag{5.4}$$

$$C = C_p + C_i \tag{5.5}$$

where f is the light modulation frequency and $f_0 = (2\pi RC)^{-1}$. The resistance and capacitance of the circuit is the combination of device and amplifier properties. For low frequencies ($f < f_0$), the transfer function can be approximated as $Z(f) \approx R$ and is only dependent on the resistances of the detector and readout circuit. At frequencies above f_0, the detector frequency response is dependent on the capacitances of the detector itself and the readout circuit [139].

$$Z(f) = \frac{-i}{2\pi f (C_p + C_i)} \tag{5.6}$$

The output voltage, V_{out}, can be calculated as [139]:

$$V_{out}(f) = I_p Z(f) + V_N \tag{5.7}$$

In contrast, the circuit can be configured to readout the current through the system using the circuit in Figure 5.13(b). In this case, R and C can be replaced by R_f and C_f because the input to the amplifier is effectively grounded, short circuiting the device resistance and capacitance. For frequencies $f < f_0$, Z(f) is constant with a value approximately equal to R_f. For frequencies larger than f_0, the transfer function can be expressed as [139]:

$$Z(f) = \frac{-i}{2\pi f C_f} \tag{5.8}$$

There are three timing components that impact the response speed of the device: 1) thermal diffusion through the detector, 2) the capacitance of the detector, and 3) the capacitance of the readout circuit. Previous work on AlN-based detectors using the same geometry presented here indicated that the thermal limit for device bandwidth is much higher than the RC limit [90]. Therefore the device geometry should be carefully considered to minimize the RC time constant. When the RC time constant of the detector is lower than that of the readout circuit, the measured band width is instrument-limited. In this case no absolute measure of the device bandwidth can be made. To avoid this, high speed readout circuits must be designed with time dynamics that allow for a faster response than the detector's limit. If the detector's RC time constant is longer than its thermal diffusion time constant, the low-impedance readout scheme can be used to short circuit the readout and measure the current through the readout circuit rather than the voltage generated across a load resistance. This effectively removes the influence of the device

resistance and capacitance from the bandwidth measurement. This allows the temperature dynamics of the device to be measured without the influence of its electrical characteristics.

When deciding to use either the current or voltage readout, it is important to take note of the noise voltage at the input of the amplifier. When measuring in current mode, the noise voltage is amplified by the feedback loop. For low frequencies the amplification factor is [139]:

$$\frac{R_f + R_p}{R_p} \approx 1 \tag{5.9}$$

but for higher frequencies the amplification is:

$$\frac{C_f + C_p}{C_f} \gg 1 \tag{5.10}$$

so the noise can be much more of a factor when using a current amplifier unless careful consideration is given, such as adding a series resistance is added to the readout circuit.

For this step, samples will be measured for their bandwidth by using the beat-frequency laser to find the change in responsivity as the modulation frequency is tuned. If the bandwidth is undesirably low (below 100 MHz), it can be improved by decreasing the detector area or increasing the PVDF-TrFE thickness to decrease capacitance. The shadow mask used to deposit the metal contacts has circular holes ranging in diameter from 50 μm to 1 mm, allowing the frequency response to be varied with detector area. The PVDF-TrFE thickness can be varied by changing spin coating solution concentration or spinning speed. The results presented here suggest that thinner films produce more uniform surfaces,

introducing a tradeoff between metasurface absorber quality and capacitance. An interesting study would be to measure the relationship between pyroelectric signal strength and PVDF-TrFE thickness. These measurements can be carried out in voltage readout mode unless the electrical properties of the detectors cause the system to be detector RC-limited. If this is the case, current readout mode must be used.

5.7.4 Flexible detector

The pivotal demonstration of this device design will be a flexible detector. This can be achieved with either a free standing PVDF-TrFE film, or by using a flexible substrate such as PDMS. The solution-based processing of all but the metal contacts is conducive to flexible devices. The fabrication will be similar to the steps for a rigid substrate. A Au film will be deposited on the bottom of the PDMS/PVDF-TrFE substrate. For the PDMS substrate, PVDF-TrFE will be spin coated on top using the same process as with the rigid substrates. In both cases a metal film will be evaporated onto the top using a shadow mask, with the metal chosen based on the desired resonance wavelength. On the top surface, PE spacer layers will be deposited by dip coating. Then nanocubes will be electrostatically adhered to the PE layers by drop casting. The same characterization techniques that were used on the rigid samples can be applied to the flexible detector to show it as a proof-of-concept towards wearable technology. The device flexion will be achieved in a manner similar to previous flexible plasmonic devices used in the Mikkelsen group. Using these steps and the completed work shown in this dissertation, a flexible pyroelectric detector

based on plasmonic absorbers can span the visible to SWIR wavelength regimes with a large bandwidth.

5.8 Summary and future considerations

In conclusion, a lithography-free, solution based fabrication technique for pyroelectric photodetection is presented. The design is based on spectrally selective plasmonic absorbers and a pyroelectric polymer. The pyroelectric polymer chosen was PVDF-TrFE and after characterizing the key parameters for depositing it by spin coating, a functional NIR photodetector is demonstrated. Characterization of the PVDF-TrFE reveals the important parameters for producing high quality pyroelectric films. A plan is outlined for improving the detector performance over a broad wavelength range and fully realizing the flexible detector. The key performance metrics including responsivity and bandwidth can be measured with the same custom measurement system shown in this chapter. The lithography-free fabrication process allows for a simple, cost-effective method for realizing thermal photodetection and opens the door to a flexible, high-performance detection platform. With the work presented here, fully realizing high-performance, low-cost thermal photodetectors based on plasmonic absorbers and fabricated in a cost-effective, solution-based process is within reach. By combining this detection platform with an actively tunable plasmonic absorber, multispectral detection can be realized in a single pixel.

6. Conclusion

This dissertation has explored the possibilities of active plasmonic devices and demonstrated active control over the optical properties of tunable plasmonic nanoantennas. Additionally, progress was made towards the development of a flexible pyroelectric photodetector. For these demonstrations, optical and PL spectroscopy was performed on a custom confocal microscope system with various light sources coupled into the optical axis. Furthermore, a custom optoelectronic measurement system was used to measure the visible and NIR response of photodetectors.

First, thin films of SPI were used to tune the optical response of plasmonic nanoantennas in Chapter 3. The extent of the spectral tuning range is investigated by measuring the scattering and absorption of plasmonic nanoantennas and metasurfaces, respectively. The tuning provided over a full line width of reversible red-shift in the plasmon resonance. Furthermore, the physical mechanism behind the increased spectral tuning with lower plasmon resonance is identified as resonant coupling between the plasmonic cavity and dipolar MC. By applying the same structure to a metasurface absorber, reversible strong coupling between MC and the plasmonic cavity is demonstrated. The results demonstrate all optical control over the plasmon resonance and identify a tuning mechanism that can be exploited for use in on-chip optical computing applications.

In Chapter 4, fluorescent dyes are embedded in the plasmonic cavity to allow the electric field enhancement's effect on the emissive properties to be studied with

spectroscopy. These emission enhancement capabilities are useful for tailoring the optical response of emitters embedded in a plasmonic cavity. By combining this enhancement with the active tuning capabilities achieved in Chapter 3, dynamic control over the optical properties of emitters can be achieved. For this, Atto 594 was chosen because its absorption and emission spectra align well with the tuning range of SPI. Embedding SPI and Atto 594 in the plasmonic cavity yields a tunable peak emission wavelength by shifting the plasmon resonance. This shift changes the wavelength with maximum Purcell enhancement, while also affecting the absorption enhancement. These changes combine to reduce the total emission enhancement but open the door to drastic changes in radiative lifetime.

The same plasmonic absorber design can be applied to enhancing the absorption in pyroelectric photodetectors. The plasmon resonance, and thus the wavelength with peak absorption can be tuned by varying the nanocube size and gap thickness. Chapter 5 presents a lithography-free, solution based fabrication technique for pyroelectric photodetection based on PVDF-TrFE. Characterization of the PVDF-TrFE reveals the important parameters for producing high quality pyroelectric films, including the spin coating parameters, film thickness, and annealing conditions. Photodetection in the NIR is achieved with peak responsivities aligning with the plasmon resonance of the absorber. This gives tunable thermal emission from the visible (~450 nm) to the SWIR (~2500 nm). A plan is outlined for improving the detector performance over this broad wavelength range. The key performance metrics including responsivity and bandwidth can be measured with the same custom measurement system shown in Chapter 5. By fabricating

the same detector design on a flexible substrate rather than rigid Si, a wearable, transparent photodetector can be achieved. The lithography-free fabrication process allows for a simple, scalable method for realizing thermal photodetection and opens the door to a flexible, high-performance detection platform. Incorporating phase change materials or taking advantage of PVDF's piezoelectric properties would allow the photodetector to implement multispectral imaging in a single pixel by tuning the plasmon resonance. Moreover, by using PVDF-TrFE films thin enough to put them in the plasmonic cavity (~10 nm), the enhanced electric fields could produce more sensitive photodetectors.

Appendix A. Experimental details

A.1 Tunable nanoantenna fabrication

A.1.1 Solution preparation

A.1.1.1 Spiropyran/PMMA solution

1.1.1.1 Prepare a 0.5% weight spiropyran(SPI)/poly(methyl methacrylate) (PMMA) solution with a 3:2 ratio of SPI:PMMA in anisole by:

1.1.1.1.a Make a stock solution of SPI/PMMA in anisole by dissolving 116 mg of SPI powder into 2 mL of PMMA solution in anisole (stock is 4% PMMA) to make 9.4% SPI/PMMA solution.

1.1.1.1.b Vortex the stock solution for 30 seconds and make sure any remaining solid has time to dissole before drawing from the stock.

1.1.1.1.c Using a micropipette, measure 125 μL of stock solution and add 2 mL of anisole to dilute the new solution to 0.5% weight of SPI/PMMA.

1.1.1.2 Vortex the solution for 30 seconds.

1.1.1.3 Allow the solution to settle for 1 hour to allow remaining powder to dissolve and any trapped air bubbles to dissipate.

A.1.1.2 Ag nanocube solution

1.1.2.1 Using a micropipette, transfer 200 μL of stock silver (Ag) nanocube solution (NanoComposix Inc., 1 mg/mL in ethanol) to a plastic centrifuge tube.

1.1.2.2 Centrifuge the solution at 4000 rpm in 5 minute intervals until all visible traces of the nanoparticles are compacted at the bottom of the tube.

1.1.2.3 Using a micropipette, remove ~195 μL of ethanol, being careful not to disturb the pellet of compacted nanocubes.

1.1.2.4 Add 195 μL of DI water to the tube. The nanocubes are now suspended in mostly water.

1.1.2.5 Vortex the solution for 30 seconds and sonicate for 5 seconds. Note that sonicating for prolonged periods (longer than 10 seconds) can result in a breakdown of the PVP protective coating on the Ag nanocubes and result in oxidation.

1.1.2.6 Centrifuge the solution at 4000 rpm in 5 minute intervals until all visible traces of the nanoparticles are compacted at the bottom of the tube.

1.1.2.7 Using a micropipette, remove 195 μL of the ethanol/water mixture, being careful not to disturb the pellet of compacted nanocubes.

1.1.2.8 Add 195 μL of DI water to the tube. The nanocubes are now suspended in almost entirely DI water.

1.1.2.9 Vortex the solution for 30 seconds and sonicate for 5 seconds.

A.1.1.3 Ag nanocube solution dilution

1.1.3.1 Using the solution obtained by following the steps in A.1.1.2, dilute the nanocube solution 1000 times by combining 10 μL of it with 10 mL of DI water.

1.1.3.2 Vortex the solution for 30 seconds and sonicate for 5 seconds.

A.1.1.4 Ag nanocube solution concentration

1.1.4.1 Using the solution obtained by following the steps in A.1.1.2, centrifuge the solution at 4000 rpm in 5 minute intervals until all visible traces of the nanoparticles are compacted at the bottom of the tube.

1.1.4.2 Using a micropipette, remove 150 μL of the water, being careful not to disturb the pellet of compacted nanocubes.S

1.1.4.4 Vortex the solution for 30 seconds and sonicate for 5 seconds.

A.1.1.5 Polyelectrolyte (PE) solutions

1.1.5.1 Prepare a 1 M sodium chloride (NaCl) solution by mixing 29 g of NaCl powder with 500 mL of DI water.

1.1.5.2 Prepare a 3 mM poly(allylamine) hydrochloride (PAH) solution in 1 M NaCl solution by first mixing 29 g of NaCl powder with 500 mL of DI water, then adding 132 mg of PAH powder.

1.1.5.3 Prepare a 3 mM poly(styrenesulphonate) (PSS) solution in 1 M NaCl by first mixing 29 g of NaCl powder with 500 mL of DI water, then adding 1.5 mL of PSS stock solution.

A.1.2 Ag film preparation

A.1.2.1 Ag evaporation

Note: An electron-beam evaporator was used to deposit Ag films onto purchased cleanroom cleaned Si wafers. The evaporation process takes place inside a vacuum

chamber, enabling the molecules to evaporate freely in the chamber and then sublimate on the substrate. The operation procedure is:

1.2.1.1 Vent the chamber, by pressing “Auto Vent”.

1.2.1.2 Open chamber door and load substrates in the dome. Verify that the Ag target is in the pocket within the chamber.

1.2.1.3 Close the door and pump down by pressing “Auto Pump”, it takes approximately six hours for the chamber to pump down until the pressure is below 7×10-7 Torr.

1.2.1.4 Edit the recipe. Layer#1: Ag, thickness: 75 nm, deposition rate: 5 Angstrom/s.

1.2.1.5 Upon reaching the desired vacuum level, the deposition process of the first metal will automatically start by pressing “Auto Run”.

1.2.1.6 After the entire process is complete, press “Auto Vent” to vent the chamber and take the sample out.

A.1.2.2 Ag template stripping

Note: When exposed to ambient air, Ag will quickly oxidize, losing its pristine plasmonic properties. To avoid this, a template stripping method protects what will become the top Ag working surface until a protective coating can be applied.

1.2.2.1 Combine a 1:1 ratio (0.8 g each) of the EPO-TEK 377 A and B epoxy mix.

1.2.2.2 Vortex for 10 seconds.

1.2.2.3 Degas in a vacuum chamber for 10 minutes, or until all visible bubbles are gone.

1.2.2.4 Cut a glass slide to the desired sample size and clean with acetone, isopropyl alcohol, and DI water. Dry with a stream of nitrogen (N_2) gas.

1.2.2.5 Dispense 10 $\mu L/cm^2$ of epoxy mixture onto the sample slide and slowly adhere it to the evaporated Ag film from A.1.2.1, making sure no air bubbles are trapped.

1.2.2.6 Baked the entire wafer at 150 C for 1 hour.

1.2.2.7 Allow the wafer and glass slides to cool back to room temperature.

1.2.2.8 Using a clean razor blade, carefully slice through any epoxy that leaked out from under the glass slide.

1.2.2.9 Using the razor, carefully scrape under a corner of the glass slide to lift it up from the Si wafer. Since Ag adheres poorly to the native oxide on the wafer, the Ag film should be lifted from the wafer along with the glass slide.

Note: Because Ag oxidizes quickly in air, the exposed Ag film should be immediately treated with an air-tight film coating, or placed in a vacuum chamber for later use.

A.1.3 SPI/PMMA film deposition

Note: This step should be performed immediately after template stripping the Ag film to avoid oxidation of the Ag by ambient air.

1.3.1 Load the sample into the spin coater and adjust the spin recipe to: 1) 750 rotations per minute (rpm) for 15 seconds, 2) 1500 rpm for 1 minute. This recipe produced

films with ~12 nm thickness. Adjusting the rotation speed in step 2 will change the final thickness.

1.3.2 Using a micropipette, dispense 200 μL/cm^2 of the SPI/PMMA solution prepared in A.1.1.1 onto the sample surface and begin the spinning process.

1.3.3 After the spin process finishes remove excess solvent by baking the sample at 70 C for 2 minutes.

A.1.4 PE layer-by-layer deposition

Note: Once the SPI/PMMA layer thickness is set, the plasmon resonance of the complete structure is determined by the nanocube size and the number of PE layers deposited. The steps here show three PE layer, but the process can be repeated for the desired number of layers. PAH is slightly positively charged while PSS is slightly negatively charged. The choice of which layer to deposit first with depend on the surface chemistry of the sample. Each layer contributes about 1 nm in thickness to the stack. The steps below will demonstrate in details how to deposit three PE layers: PAH/PSS/PAH.

1.4.1 Immerse the entire sample in into the PAH solution prepared in A.1.1.5.2 for 5 minutes.

1.4.2 Rinse the sample with DI water.

1.4.3 Immerse the sample in NaCl solution prepared in A.1.1.5.1 for 1 minute.

1.4.4 Rinse the sample with DI water.

1.4.5 Immerse the sample in into the PSS solution prepared in A.1.1.5.3 for 5 minutes.

1.4.6 Rinse the sample with DI water.

1.4.7 Immerse the sample in NaCl solution for 1 minute.

1.4.8 Rinse the sample with DI water.

1.4.9 Immerse the sample in into the PAH solution for 5 minutes.

1.4.10 Rinse the sample with DI water.

1.4.11 Immerse the sample in NaCl solution for 1 minute.

1.4.12 Rinse the sample with DI water.

1.4.13 Dry the sample with a stream of N_2 gas.

A.1.5 Fluorescent dye deposition

1.5.1 Prepare a 25 μM Atto 594 solution with DI water as the solvent.

1.5.2 Expose the surface of the sample (which has a series of SPI/PMMA and PE layers the previous sections) to 100 μL of a 25 μM Atto 594 solution.

1.5.3 First drop cast 100 μL of the Atto 594 solution onto the sample surface and then place a cover slip on top of the solution drop.

1.5.4 After 10 min, rinse the sample with DI water and dry it with clean N_2 gas.

A.1.6 Ag nanocube deposition

Note: The process is the same for depositing dense, metasurface coverage of nanocubes on the sample surface or for producing sparse, individual nanoantenna coverage. The difference comes from which nanocube solution is chosen between the 1000x dilution

prepared in A.1.1.3 or the 4x concentration prepared in A.1.1.4 and the length of the deposition time.

1.6.1 Using a micropipette, drop 7.92 μL of nanocube solution prepared in A.1.1.3/4 onto a circular glass cover slip with a diameter of 12 mm. For individually addressable nanoantennas, use the 1000x diluted solution (A.1.1.3). For metasurfaces, use the 4x concentrated solution (A.1.1.4).

1.6.2 Carefully place the coverslip in contact with the sample surface making sure to avoid air bubbles. For individually addressable nanoantennas, allow the solution to stay in contact with the surface for 15 minutes. For metasurfaces, leave the solution for 1 hour.

1.6.3 Rinse the cover slip and solution off the sample surface with DI water and dry with N_2 gas.

A.2 Pyroelectric photodetector fabrication

A.2.1 Au film preparation

Note: An electron-beam evaporator was used to deposit Au films onto purchased cleanroom cleaned Si wafers. The operation procedure is:

1.2.1.1 Vent the chamber, by pressing “Auto Vent”.

1.2.1.2 Open chamber door and load substrates in the dome, remembering to evaporate onto the back (unpolished) side of the wafer and taking care not to scratch the top surface. It might be helpful to cover the top (polished) side of the wafer with a protective film during this step. Verify that the Au target is in the pocket within the chamber.

1.2.1.3 Close the door and pump down by pressing “Auto Pump”, it takes approximately 2 hours for the chamber to pump down until the pressure is below 1×10-6 Torr.

1.2.1.4 Edit the recipe. Layer#1: Au, thickness: 75 nm, deposition rate: 2 Angstrom/s.

1.2.1.5 Upon reaching the desired vacuum level, the deposition process of the first metal will automatically start by pressing “Auto Run”.

1.2.1.6 After the entire process is complete, press “Auto Vent” to vent the chamber and take the sample out.

A.2.2 PVDF-TrFE film deposition

2.2.1 Prepare a 5% weight solution of PVDF-TrFE in DMAc by mixing 50 mg of PVDF-TrFE (70/30%) powder with 950 mg (~1 mL) of DMAc.

2.2.2 Add a magnetic stir bar to the solution and mix with a magnetic stirrer for 1 hour at 120 rpm.

2.2.3 Let the solution stand until all air bubbles have dissipated.

2.2.4 Dice the Si wafer with Au on the back (from A.2.1) into ~1”x1” samples.

2.2.4 Load the samples into the spin coater and adjust the spin recipe to 2000 rpm for 30 seconds.

2.2.5 Remove excess solvent by heating the sample at 100 C for 1 minute.

A.2.3 Metal contact deposition

Note: An electron-beam evaporator was used to deposit Au films onto the prepared PVDF-TrFE samples. The operation procedure is:

2.3.1 Adhere the samples to a shadow mask using kapton tape, such that the holes allow metal to be deposited on the desired areas of the sample.

2.3.2 Vent the chamber, by pressing “Auto Vent”.

2.3.3 Open chamber door and load substrates in the dome. Verify that the Au target is in the pocket within the chamber.

2.3.4 Close the door and pump down by pressing “Auto Pump”, it takes approximately 2 hours for the chamber to pump down until the pressure is below 1×10-6 Torr.

2.3.5 Edit the recipe. Layer#1: Au, thickness: 75 nm, deposition rate: 2 Angstrom/s.

2.3.6 Upon reaching the desired vacuum level, the deposition process of the first metal will automatically start by pressing “Auto Run”.

2.3.7 After the entire process is complete, press “Auto Vent” to vent the chamber and take the sample out.

2.3.8 Carefully peel the kapton tape away from the sample to release the shadow mask.

A.2.4 PE layer-by-layer deposition

Note: The plasmon resonance of the complete structure is determined by the nanocube size and the number of PE layers deposited. The steps here show three PE layer, but the process

can be repeated for the desired number of layers. PAH is slightly positively charged while PSS is slightly negatively charged. The choice of which layer to deposit first with depend on the surface chemistry of the sample. Each layer contributes about 1 nm in thickness to the stack. The steps below will demonstrate in details how to deposit three PE layers: PAH/PSS/PAH.

2.4.1 Immerse the entire sample in into the PAH solution prepared in A.1.1.5.2 for 5 minutes.

2.4.2 Rinse the sample with DI water.

2.4.3 Immerse the sample in NaCl solution prepared in A.1.1.5.1 for 1 minute.

2.4.4 Rinse the sample with DI water.

2.4.5 Immerse the sample in into the PSS solution prepared in A.1.1.5.3 for 5 minutes.

2.4.6 Rinse the sample with DI water.

2.4.7 Immerse the sample in NaCl solution for 1 minute.

2.4.8 Rinse the sample with DI water.

2.4.9 Immerse the sample in into the PAH solution for 5 minutes.

2.4.10 Rinse the sample with DI water.

2.4.11 Immerse the sample in NaCl solution for 1 minute.

2.4.12 Rinse the sample with DI water.

2.4.13 Dry the sample with a stream of N_2 gas.

A.2.5 Metasurface absorber deposition

Note: The plasmon resonance is set by the combination of PE layer thickness and nanocube size.

2.5.1 Using a micropipette, drop 7.92 μL of nanocube solution prepared in A.1.1.4 onto a circular glass cover slip with a diameter of 12 mm.

2.5.2 Carefully place the coverslip in contact with the sample surface making sure to avoid air bubbles. Let stand for 1 hour.

2.5.3 Rinse the cover slip and solution off the sample surface with DI water and dry with N_2 gas.

A.3 Optical characterization

Note: A custom built optical bright-/dark-field microscope is used in these measurements. The nanoantennas are illuminated by a white light source through a long working distance bright-/dark- field objective. The reflected/scattered light from the nanoantennas is collected by the same objective. A pinhole aperture (150 micrometer diameter) is used at an image plane to select signal from an individual nanoantenna or select suitable areas of a metasurface. An electromagnetic charge coupled device (EM-CCD) camera is used to capture images of the sample surface. A spectrometer and a CCD camera are used to acquire spectral data at visible to NIR wavelengths. The IR spectra are collected with an InGaAs camera. For fluorescence measurements, a 532 nm continuous wave laser diode is used for excitation and the signal was spectrally filtered by a long pass filter.

A.3.1 Dark field scattering of single nanoantennas

3.1.1. Under white light illumination with the microscope in dark-field (high incidence-angle) configuration and high magnification (100x) objective, identify nanoantennas on the sample that was prepared in Section A.1. Under white light illumination, individual nanoantennas appear as bright dots in an EM-CCD image. A spectral filter can isolate the image from nanoantennas from those of imperfections in the sample surface.

3.1.2. Align the sample area with the pinhole aperture using a translation stage. An alignment laser can be used to ensure that the image of the nanoantenna is centered in the pinhole aperture.

3.1.3. Acquire a spectrum of the scattered light from the nanoantenna using the spectrometer and CCD camera with a 30 second integration time. Because the aperture area (150 μm) is much bigger than the physical size of the nanoantenna (~ 75 nm) the spectrum contains scattered light from the nanoantenna in addition to signal from the area surrounding the nanoantenna.

3.1.4. Move the sample to an area without any nanoantennas and acquire another spectrum with a 30 second integration time. This spectrum represents scattered light from the background.

3.1.5. Remove the sample with nanoantennas and place a certified reflectance standard sample in the setup. Acquire a spectrum of the scattered light with a 0.1 second integration time in order to normalize the signal from the nanoantenna.

3.1.6. Close the pinhole aperture and acquire a spectrum with a 0.1 second integration time without any input signal. This spectrum represents the CCD dark counts.

3.1.7. Calculate the final scattering spectrum of a nanoantenna as:

$$\text{Nanoantenna scattering} = \frac{I_{\text{nanoantenna+background}} - I_{\text{background}}}{I_{\text{standard}} - I_{\text{dark}}} \qquad (A.1)$$

where $I_{\text{nanoantenna+background}}$, $I_{\text{background}}$, I_{standard}, I_{dark} are the scattering spectra measured by steps 3.1.3, 3.1.4, 3.1.5 and 3.1.6, respectively.

3.1.8. Extract the plasmon resonance of the nanoantenna by calculating the centroid of the scattering resonance peak.

A.3.2 Bright-field reflection of metasurface absorbers

3.2.1. Under white light illumination with the microscope in bright-field (normal incidence) configuration and lower magnification (20x) objective, identify regions on the sample that was prepared in Section A.1 or A.2. Under white light illumination, ensembles of nanoantennas appear as clusters of bright and dark dots in an EM-CCD image. They can be differentiated by eye from uncoated regions which appear smooth.

3.2.2. Align the sample area with the pinhole aperture using a translation stage. An alignment laser can be used to ensure that the image of the metasurface is centered in the pinhole aperture.

3.2.3. Acquire a spectrum of the reflected light from the metasurface using the spectrometer and CCD camera with a 10 ms integration time. Because the nanoantennas

do not cover 100% of the sample surface, the spectrum contains reflected light from the metal back-mirror in addition to signal from the area covered by the nanoantennas.

3.2.4. Move the sample to an area without any nanoantennas and acquire another spectrum with a 10 ms integration time. This spectrum represents reflected light from the back-mirror.

3.2.6. Close the pinhole aperture and acquire a spectrum with a 10 ms integration time without any input signal. This spectrum represents the CCD dark counts.

3.2.7. Calculate the final reflected spectrum due to the ensemble of nanoantennas as:

$$\text{Metasurface reflection} = \frac{I_{\text{metasurface+background}} - I_{\text{dark}}}{I_{\text{background}} - I_{\text{dark}}} \qquad \text{(A.2)}$$

where $I_{\text{metasurface+background}}$, $I_{\text{background}}$, I_{dark} are the reflection spectra measured by steps 3.2.3, 3.2.3, and 3.2.4, respectively.

3.2.8. Extract the plasmon resonance of the metasurface by calculating the centroid of the reflection resonance minimum.

A.3.3 Optical tuning of SPI

Note: This process is the same whether tuning single nanoantennas or ensembles of them in a metasurface.

3.3.1 Collect a scattering or reflection spectrum as described in Section A.3.1.

3.3.2 Align the UV LED into the optical path using the EM-CCD to verify that the selected sample region is illuminated.

3.3.3 Illuminate the sample with UV light at up 1 mW/cm^2 for 10 minutes. Higher powers might damage the SPI and prevent photochromic switching.

3.3.4 Collect another scattering or reflection spectrum to compare to the original.

3.3.5 The photochromic switching can be reversed by illuminating the sample with white light for 10 minutes, or by heating the sample at 70 C for 5 minutes.

A.3.4 Fluorescence enhancement of Atto 594

3.4.1 Under white light illumination, identify single nanoantennas or metasurfaces from the sample prepared in Section A.1.

3.4.2 Align the pinhole aperture with the selected sample region using a translation stage and alignment laser.

3.4.3 Turn off the white light illumination and turn on the 532 nm continuous wave laser diode used for excitation.

3.4.4 Place a 532 nm long pass laser filter in the optical path right before the entrance to the spectrometer in order to block any scattered laser light.

3.4.5 Acquire a fluorescence spectrum of the emission from the Atto 594 molecules using a 10 second integration time. Because the aperture area (50 μm) is much larger than the physical size of an individual nanoantenna (~ 75 nm) this spectrum contains emission from both molecules embedded in the nanoantenna gap as well as molecules surrounding it.

3.4.6 Move the sample to an area without any nanoantennas and acquire another spectrum with a 10 s integration time. This spectrum represents the emission from molecules in the background, without any nanoantennas.

3.4.7 Prepare a separate sample, which will be used as a control sample, following the procedure in Sections A.1 where Atto 594 molecules are incorporated with PE layers on top of a glass slide (without a Ag film and Ag nanocubes).

3.4.8 Acquire a fluorescence spectrum of the emission from Atto 594 molecules on the control sample prepared in the previous step using a 30 s integration time.

3.4.9 Determine the fluorescence enhancement factor by using the fluorescence spectra measured in steps 3.4.5, 3.4.6 and 3.4.8, taking into account the CCD dark counts, normalization by unit area and acquisition times.

A.4 Photodetector responsivity measurement

Note: A custom built photovoltage measurement system is used in these experiments. The metasurfaces on the photodetector samples are illuminated by the chopped and filtered emission from a broad spectrum super-continuum laser through a reflective microscope objective. The absorbed light heats the pyroelectric film in the detectors. Tungsten micromanipulator probe tips contact to measure the electrical signal generated by the detector. The differential voltage between the tips is sent to a voltage pre-amplifier and then collected by a lock-in amplifier set to focus on the chopper's modulation frequency.

4.1 Adhere the sample to the motion stage using conductive copper tape. Be sure to leave a portion of the back side of the sample exposed to be contacted by the probe tip.

4.2 Allow the chopped laser beam to illuminate the sample.

4.3 Move the sample stage through the laser focus through the objective to change the beam size at the sample surface. Try to match the beam diameter to the detector area.

4.4 Contact each side of the detector with the probe tips while taking care not to block the beam path with the tips.

4.5 Block and unblock the laser to verify that the electrical signal on the lock-in amplifier is measuring a pyroelectric response.

4.6 Adjust the laser power by rotating the ND filter wheel and measuring the output on a power meter.

4.7 Record the photovoltage and incident laser power.

4.8 Calculate the detector responsivity as:

$$\text{Responsivity} = \frac{V_{measured} - V_{dark}}{G * P_{incident}} \quad \text{(A.3)}$$

where $V_{measured}$ is the output of the lock-in amplifier, V_{dark} is the lock-amplifier noise, G is the pre-amplifier gain, and $P_{incident}$ is the laser power at the sample surface.

4.9 Adjust the output wavelength of the super-continuum laser.

4.10 Rotate the ND filter wheel until the power matches the previous measurement

4.11 Collect and record another photovoltage measurement.

4.12 Construct a responsivity spectrum by repeating steps 4.9-4.11 for the desired wavelength range and calculating the responsivity at each data point.

References

[1] J. J. Talghader, A. S. Gawarikar, and R. P. Shea, *Light Sci. Appl.* **1**, e24 (2012)

[2] M. A. Baqir and P. K. Choudhury, *IEEE Photon. Technol. Lett.* **29**, 1548-1551 (2017)

[3] X. Ni, A. V. Kildishev, V. M. Shalaev, *Nat. Commun.* **4**, 2807 (2013)

[4] G. M. Akselrod, J. Huang, T. B. Hoang, P. T. Bowen, L. Su, D. R. Smith, and M. H. Mikkelsen, *Adv. Mater.* **27**, 8028-8034 (2015)

[5] J.-Y. Jung, J. Lee, D.-G. Choi, J.-H. Choi, J.-H. Jeong, E.-S. Lee, and D. P. Neikirk, *IEEE Photonics J.* **7**, 1-10 (2015)

[6] C. Wu, B. Neuner, III, G. Shvets, J. John, A. Milder, B. Zollars, S. Savoy, *Phys. Rev. B* **84**, 075102 (2011)

[7] T. B. Hoang, G. M. Akselrod, C. Argyropoulos, J. Huang, D. R. Smith, and M. H. Mikkeslen, *Nat. Commun.* **6**, 7788 (2015)

[8] A. Moreau, C. Ciraci, J. J. Mock, R. T. Jill, Q. Wang, B. J. Wiley, A. Chilkoti, and D. R. Smith, *Nature* **492**, 86-89 (2012)

[9] M. J. Rozin, D. A. Rosen, T. J. Dill, and A. R. Tao, *Nat. Commun.* **6**, 7325 (2015)

[10] C. Lumdee, S. Toroghi, and P. Kik, *ACS Nano* **6**, 6301−6307 (2012)

[11] X. Zhu, C. Vannahme, E. Højlund-Nielsen, N. Asger Mortensen, and A. Kristensen, *Nat. Nanotechnol.* **11**, 325−329 (2016)

[12] Z. Liu, D. Zhu, S. P. Rodrigues, K.-T. Lee, and W. Cai, *Nano Lett*. **18**, 6570-6576 (2018)

[13] R. Pestourie, C. Perez-Arancibia, Z. Lin, W. Shin, F. Capasso, and S. G. Johnson, *Opt. Express* **26**, 33732-33747 (2018)

[14] W. M. Wilson, J. W. Stewart, and M. H. Mikkelsen, *Nano Lett.* **18**, 853-858 (2018)

[15] G. T. Sincerbox and J. C. Gordon II, *Appl. Opt.* **20**, 1491-1496 (1981)

[16] R. Reinisch, P. Vincent, M. Neviere, and E. Pic, *Appl. Opt.* **24**, 2001-2004 (1985)

[17] E. M. Yeatman, M. E. Caldwell, *Appl. Phys. Lett.* **55**, 613 (1989)

[18] J. J. Baumberg, J. Aizpurua, M. H. Mikkelsen, and D. R. Smith, *Nat. Mater*. **18**, 668–678 (2019)

[19] N. Jiang, X. Zhuo, J. Wang, *Chem. Rev.* **118**, 3054-3099 (2018)

[20] D. F. Cruz, C. M. Fontes, D. Semeniak, J. Huang, A. Hucknall, A. Chilkoti, and M. H. Mikkelsen, *Nano Lett. accepted* (2020)

[21] F. Aieta, P. Geneven, M. A. Kats, N. Yu, R. Blanchard, Z. Gaburro, and F. Capasso, *Nano Lett*. **12**, 4932-4936 (2012)

[22] J. W. Stewart, G. M. Akselrod, D. R. Smith, and M. H. Mikkelsen, *Adv. Mater.* **29**, 1602971 (2016)

[23] X. Zhu, C. Vannahme, E. Højlund-Nielsen, N. Asger Mortensen, and A. Kristensen, *Nat. Nanotechnol.* **11**, 325−329 (2016)

[24] D. Pines and D. Bohm, *Phys. Rev*. **82**, 625-634 (1951)

[25] D. Pines and D. Bohm, *Phys. Rev*. **85**, 338-353 (1952)

[26] D. Pines and D. Bohm, *Phys. Rev*. **92**, 609-625 (1953)

[27] E. A. Stern and R. A. Ferrell, *Phys. Rev.* **120**, 130-136 (1960)

[28] C. J. Powell and J. B. Swan, *Phys. Rev*. **118**, 640-643 (1960)

[29] S. A. Maier, *Plasmonics: Fundamentals and Applications* (2007)

[30] A. Kinkhabwala, Z. Yu, S. Fan, Y, Avlasevich, K. Müllen and W. E. Moerner, *Nat. Photonics* **3**, 654-657 (2009)

[31] T. B. Hoang and M. H. Mikkelsen, *Appl. Phys. Lett*. **108**, 183107 (2016)

[32] J. Chen, Y. Li, Z. Chen, J. Peng, J. Qian, J. Xu, and Q. Sun, *IEEE Photonics J*. **6**, 1-6 (2014)

[33] A. Sobhani, A. Lauchner, S. Najmaei, C. Ayala-Orozco, F. Wen, J. Lou, and N. J. Halas, *Appl. Phys. Lett.* **104**, 31112 (2014)

[34] S. Butun, S. Tongay, and K. Aydin, *Nano Lett.* **15**, 2700 (2015)

[35] J. Kern, A. Trugler, I. Niehues, J. Ewering, R. Schmidt, R. Schneider, S. Najmaei, A. George, J. Zhang, J. Lou, U. Hohenester, S. Michaelis De Vasconcellos, and R. Bratschitsch, *ACS Photonics* **2**, 1260 (2015)

[36] K. C. J. Lee, Y.-H. Chen, H.-Y. Lin, C.-C. Cheng, P.-Y. Chen, T.-Y. Wu, M.-H. Shih, K.-H. Wei, L.-J. Li, and C.-W. Chang, *Sci. Rep*. **5**, 16374 (2015)

[37] B. Lee, J. Park, G. H. Han, H. S. Ee, C. H. Naylor, W. Liu, A. T. C. Johnson, and R. Agarwal, *Nano Lett.* **15**, 3646 (2015)

[38] N. I. Landy, S. Sajuyigbe, J. J. Mock, D. R. Smith, and W. J. Padilla, *Phys. Rev. Lett.* **100**, 207402 (2008)

[39] C. Rockstuhl, T. Zentgraf, H. Guo, N. Liu, C. Etrich, I. Loa, K. Syassen, J. Kuhl, F. Lederer, and H. Giessen, *Appl. Phys. B* **84**, 219–227 (2006)

[40] G. G. D. Han, H. Li and J. C. Grossman, *Nature Comm*. **8**, 1446 (2017)

[41] A.-K. Michel, P. Zalden, D. Chigrin, M. Wuttig, A. Lindenberg, and T. Taubner, *ACS Photonics* **1**, 833−839 (2014)

[42] S. Raoux, G. W. Burr, M. J. Breitwisch, C. T. Rettner, Y.-C. Chen, R. M. Shelby, M. Salinga, D. Krebs, S.-H. Chen, H.-L. Lung, and C. H. Lam, *IBM J. Res. Dev.* **52**, 465-479 (2008)

[43] W. H. Zachariasen, *J. Am. Chem. Soc.* **54**, 3841–3851 (1932)

[44] S. Earl, T. James, T. Davis, J. McCallum, R. Marvel, R. Haglund, and A. Roberts, *Opt. Express* **21**, 27503 (2013)

[45] H. Kocer, S. Butun, B. Banar, K. Wang, S. Tongay, J. Wu, and K. Aydin, Appl. *Phys. Lett*. **106**, 161104 (2015)

[46] D. Y. Lei, K. Appavoo, Y. Sonnefraud, R. F. Haglund, and S. A. Maier, *Opt. Lett*. **35**, 3988 (2010)

[47] Y. Abate, R. Marvel, J. Ziegler, S. Gamage, M. Javani, M. Stockman, and R. Haglund, *Sci. Rep*. **5**, 13997 (2015)

[48] X. Yin, M. Schaferling, A.-K. Michel, A. Tittl, M. Wuttig, T. Taubner, and H. Giessen, *Nano Lett*. **15**, 4255−4260 (2015)

[49] Y. Yang, K. Kelley, E. Sachet, S. Campione, T. Luk, J.-P. Maria, M. Sinclair, and I. Brener, *Nat. Photonics* **11**, 390−395 (2017)

[50] K. MacDonald, Z. Samson, M. Stockman, and N. Zheludev, *Nat. Photonics* **3**, 55−58 (2009)

[51] P. Guo, R. Schaller, J. Ketterson, and R. Chang, *Nat. Photonics* **10**, 267−273 (2016)

[52] M. Abb, P. Albella, J. Aizpurua, and O. Muskens, *Nano Lett.* **11**, 2457−2463 (2011)

[53] J. Kim, H. Son, D. J. Cho, B. Geng, W. Regan, S. Shi, K. Kim, A. Zettl, Y.-R. Shen, and F. Wang, *Nano Lett*. **12**, 5598−5602 (2012)

[54] F. Yi, E. Shim, A. Zhu, H. Zhu, J. Reed, and E. Cubukcu, *Appl. Phys. Lett.* **102**, 221102 (2013)

[55] Y. Vardi, E. Cohen-Hoshen, G. Shalem, and I. Bar-Joseph, *Nano Lett*. **16**, 748−752 (2016)

[56] J. Müller, C. Sönnichsen, H. von Poschinger, G. von Plessen, T. Klar, and J. Feldmann, *Appl. Phys. Lett*. **81**, 171−173 (2002)

[57] K. Chu, C. Chao, Y. Chen, Y. Wu, C. Chen, *Appl. Phys. Lett.* **89**, 103107 (2006)

[58] V. W. Brar, M. Seok Jang, M. Sherrott, J. J. Lopez, and H. A. Atwater, *Nano Lett*. **13**, 2541-2547 (2013)

[59] D. C. Zografopoulos, R. Beccherelli, A. C. Tasolamprou, and E. E. Kriezis, *Photonic Nanostruct*. **11**, 73-84 (2013)

[60] F. Huang, and J. Baumberg, *Nano Lett*. **10**, 1787−1792 (2010)

[61] X. Duan, S. Kamin, and N. Liu, *Nat. Comm*. **8**, 14606 (2017)

[62] G. Wang, X. Chen, S. Liu, C. Wong, and S. Chu, *ACS Nano* **10**, 1788 (2016)

[63] T. König, P. Ledin, J. Kerszulis, M. Mahmoud, M. El-Sayed, J. Reynolds, V. Tsukruk, V. *ACS Nano* **8**, 6182−6192 (2014)

[64] A. Brown, M. Sheldon, and H. Atwater, *ACS Photonics* **2**, 459−464 (2015)

[65] A. Yang, T. Hoang, M. Dridi, C. Deeb, M. H. Mikkelsen, G. Schatz, and T. Odom, *Nat. Comm*. **6**, 6939 (2015)

[66] T. Ding, D. Sigle, L. Zhang, J. Mertens, B. de Nijs, and J. Baumberg, J. *ACS Nano* **9**, 6110−6118 (2015)

[67] T. Ding, C. Rüttiger, X. Zheng, F. Benz, H. Ohadi, G. Vandenbosch, V. Moshchalkov, M. Gallei, and J. Baumberg, *Adv. Opt. Mater*. **4**, 877−882 (2016)

[68] M. A. Kats, R. Blanchard, P. Genevet, Z. Yang, M. Mumtaz Qazilbash, D. N. Basov, S. Ramanathan, and F. Capasso, *Optics Lett*. **38**, 368-370 (2013)

[69] A. Rose, T. B. Hoang, F. McGuire, J. J. Mock, C. Ciraci, D. R. Smith, and M. H. Mikkelsen, *Nano Lett.* **14**, 4797-4802 (2014)

[70] G. M. Akselrod, C. Argyropoulos, T. B. Hoang, C. Cirachi, C. Fang, J. Huang, D. R. Smith, M. H. Mikkelsen, *Nat. Photonics* **8**, 835-840 (2014)

[71] E. M. Purcell, H. C. Torrey, and R. V. Pound, *Phys. Rev.* **69**, 37 (1946)

[72] J. Huang, *Valley Dynamics and Tailored Light-matter Interaction in Two-dimensional Transition Metal Dichalcogenides*, Duke University Dissertation (2019)

[73] S. Nakayama, S. Ishida, S. Iwamoto, and Y. Arakawa, *Appl. Phys. Lett*. **98**, 171102–171104 (2011)

[74] J. T. Robinson, C. Manolatou, L. Chen, and M. Lipson, *Phys. Rev. Lett*. **95**, 143901–143904 (2005)

[75] M. Ringler, A Schwemer, M. Wunderlich, A. Nichtl, K. Kürzinger, T. A. Klar, and J. Feldmann, *Phys. Rev. Lett*. **100**, 203002 (2008)

[76] F. Stöckmann, *Appl. Phys*. **7**, 1-5 (1975)

[77] S. B. Lang, *Physics Today* **8**, 31 (2005)

[78] S. P. Langley, *Proc. Am. Acad. Arts Sci*. **16**, 342-358 (1880)

[79] M. Henini, M. Razeghi, *Handbook of Infra-red Detection Technologies* (2002)

[80] T. J. Seebeck, *Magnetische Polarisation der Metalle und Erze durch Temperatur-Differenz, Abhandlungen der Preussischen Akad, Wissenschaften*, 265–373 (1822)

[81] A. W. Van Herwaarden, D. C. Van Duyn, B. W. Van Oudheusden, and P. M. Sarro, *Sens. Actuators* **A21-A23**, 621-630 (1989)

[82] A. Graf, M. Arndt, M. Sauer, and G. Gerlach, *Meas. Sci. Technol.* **18**, R59-R75 (2007)

[83] N. W. Ashcroft, N. D. Mermin, *Solid State Physics* (1976)

[84] M. Almasri, B. Xu, J. Castracane, *IEEE Sens. J.* **6**, 293-300 (2006)

[85] N. Neumann, M. Ebermann, S. Kurth, K. Hiller, *J. Micro-nanolith. MEM.* **7**, 021004 (2008)

[86] Q. Li, Z. Li, N. Li, X. Chen, P. Chen, X. Shen, W. Lu, *Sci. Rep*. **4**, 6332 (2015)

[87] T. D. Dao, S. Ishii, T. Yokoyama, T. Sawada, R. P. Sugavaneshwar, K. Chen, Y. Wada, T. Nabatame, and T. Nagao, *ACS Photonics* **3**, 1271-1278 (2016)

[88] J. H. Goldsmith, S. Vangala, J. R. Hendrickson, J. W. Cleary, J. H. Vella, *J. Opt. Soc. Am. B* **34**, 1965-1970 (2017)

[89] J. Y. Suen, K. Fan, J. Montoya, C. Bingham, V. Stenger, S. Sriram, W. J. Padilla, *Optica* **4**, 276-279 (2017)

[90] J. Stewart, J. H. Vella, W. Lei, S. Fan, and M. H. Mikkelsen, *Nat. Mater*. **19**, 158-162 (2020)

[91] Z. Wang, R. Yu, C. Pan, Z. Li, J. Yang, F. Yi, and Z. L. Wang, *Nat. Commun.* **6**, 8401 (2015)

[92] S. C. Stotlar, E. J. McLellan, *Optical Engineering* **20**, 203469 (1981)

[93] M. El Badawe, T. S. Almoneef, and O. M. Ramahi, *Sci. Rep*. **6**, 19268 (2016)

[94] P. A. Huidobro, M. Kraft, S. A. Maier, and J. B. Pendry, *ACS Nano*. **10**, 5499–5506 (2016)

[95] G. M. Akselrod, J. Huang, T. B. Hoang, P. T. Bowen, L. Su, D. R. Smith, M. H. Mikkelsen, *Adv. Mater*. **27**, 8028-8034 (2015)

[96] X. Tang, M. M. Ackerman, and P. Guyot-Sionnest, *ACS Nano* **12**, 7362-7370 (2018)

[97] D. K. Efetov, R.-J. Shiue, Y. Gao, B. Skinner, E. D. Walsh, H. Choi, J. Zheng, C. Tan, G. Grosso, C. Peng, J. Hone, K. C. Fong, and D. Englund, *Nat. Nanotechnol.* **13**, 797-801 (2018)

[98] S. Ramasundaram, S. Yoon, K. J. Kim, and J. S. Lee, *Macromol. Chem. Phys*. **209**, 2516-2526 (2008)

[99] S. J. Kang, Y. J. Park, J. Sung, P. S. Jo, and C. Park, *Appl. Phys. Lett*. **92**, 012921 (2008)

[100] X. He, K. Yao, *Appl. Phys. Lett*. **89**, 112909 (2006)

[101] Y. J. Park,, S. J. Kang, and C. Park, *Appl. Phys. Lett*. **88**, 242908 (2006)

[102] M. G. Broadhurst, G. T. Davis, and J. E. McKinney, *J. Appl. Phys*. **49**, 4992 (1978)

[103] A. J. Hopfinger, *Conformational properties of macromolecules* (1973)

[104] N. C. Banik, F. P. Boyle, T. J. Sluckin, P. L. Taylor, S. K. Tripathy, A. J. Hopfinger, *Phys. Rev. Lett.* **43**, 456-460 (1979)

[105] F.-C. Sun, A. M. Dongare, A. D. Asandei, S. P. Alpay, and S. Nakhmanson, *J. Mater. Chem. C* **3**, 8389-8396 (2015)

[106] C. Xie and F. Yan, *Small* **13**, 1701822 (2017)

[107] F. Paleyo Garcia de Arquer, A. Armin, P. Meredith, and E. H. Sargent, *Nat. Rev. Mater.* **2**, 16100 (2017)

[108] D. B. Velusamy, R. H. Kim, S. Cha, J. Huh, R. Khazaeinezhad, S. H. Kassani, G. Song, S. M. Cho, S. H. Cho, I. Hwang, J. Lee, K. Oh, H. Choi, and C. Park, *Nat. Commun.* **6**, 8063 (2015)

[109] A. Yildiz, Z. Celik-Butler, and D. P. Butler, *IEEE Sens. J.* **4**, 112-117 (2004)

[110] T. Barman, A. R. Pal, *ACS Appl. Mater. Interfaces* **7**, 2166–2170 (2015)

[111] N. W. Tyer and R. S. Becker, *J. Am. Chem. Soc.*, **92**, 1289–1294 (1970)

[112] E.E. Polymeropoulos and D. Möbius, *Ber. Bunsenges. Phys. Chem.*, **83**, 1215 (1979)

[113] R. Klajn, *Chem. Soc. Rev.*, ***43***, 148–84 (2014)

[114] A. Tork, F. Boudreault, M. Roberge, A. M. Ritcey, R. A. Lessard, and T. V. Galstian, *Appl. Opt.*, **40**, 1180−1186 (2001)

[115] A.-L. Baudrion, A. Perron, A. Veltri, A. Bouhelier, P.-M. Adam, R. Bachelot, *Nano Lett.*, **13**, 282−286 (2013)

[116] T. Schwartz, J. Hutchison, C. Genet, T. Ebbesen, *Phys. Rev. Lett.*, **106**, 196405 (2011)

[117] Y. Zheng, B. Kiraly, S. Cheunkar, T. Huang, P. Weiss, *Nano Lett.*, **11**, 2061 (2011)

[118] T. Cai, R. Bose, G. Solomon, E. Waks, *Appl. Phys. Lett*., **102**, 141118 (2013)

[119] D. Sridharan, E. Waks, G. Solomon, J. Fourkas, *Appl. Phys. Lett.*, **96**, 153303 (2010)

[120] B. Lassiter, F. McGuire, J. Mock, C. Ciracì, R. Hill, B. Wiley, A. Chilkoti, and D. Smith, *Nano Lett.*, **13**, 5866−5872 (2013)

[121] R. Chikkaraddy, X. Zheng, F. Benz, L. Brooks, B. de Nijs, C. Carnegie, M.-E. Kleemann, J. Mertens, R. Bowman, G. Vandenbosch, V. Moshchalkov, and J. Baumberg, *ACS Photonics*, **4**, 469 (2017)

[122] P. Johnson and R. Christy, *Phys Rev B*, **6**, 4370–4379 (1972)

[123] N. Liu, M. Mesch, T. Weiss, M. Hentschel, and H. Giessen, *Nano Lett.* **10**, 2342 (2010)

[124] C. Wu, B. Neuner, G. Shvets, J. John, A. Milder, B. Zollars, and S. Savoy, *Phys. Rev. B* **84**, 75102 (2011)

[125] A. Moreau, C. Ciracì, J. J. Mock, R. T. Hill, Q. Wang, B. J. Wiley, A. Chilkoti, and D. R. Smith, *Nature* **492**, 86 (2012)

[126] C. Ciuti, G. Bastard, and I. Carusotto, *Phys Rev B*, **72**, 115303 (2005)

[127] Y. Yu, G. Fan, A. Fermi, R. Mazzaro, V. Morandi, P. Ceroni, D.-M. Smilgies, D.-and B. Korgel, *J Phys Chem C* **121**, 23240-23248 (2017)

[128] Atto 594 – 08637 Sigma Aldrich (2018)

[129] W. Tian and J. Tian, *Langmuir* **30**, 3223-3227 (2014)

[130] B. Ploss, F. G. Shin, H. L. W. Chan and C. L. Choy, *IEEE Trans. Dielectr. Electr. Insul.***7**, 517-522 (2000)

[131] C. Ribeiro, C. M. Costa, D. M. Correia, J. Nunes-Pereira, J. Oliveira, P. Martins, R. Goncalves, V. F. Cardosa, and S. Lanceros-Mendez, *Nat. Protoc.* **13**, 681-704 (2018)

[132] S. Horiuchi and Y. Tokura, *Nature Materials* **7**, 357–366 (2008)

[133] D. K. Das-gupta, *Ferroelectrics* **118**, 165-189 (1991)

[134] N. Levi, R. Czerw, S. Xing, P. Iyer,and D. L. Carroll *Nano Letters* **4**, 1267-1271 (2004)

[135] S. B. Lang, and S. Muensit, *Appl. Phys. A* **85**, 125-134 (2006)

[136] J. J. Simonne, F. Bauer, and L. Audaire, *Ferroelectrics* **171**, 239-252 (1995)

[137] X. He, J. Yao, *Appl. Phys. Lett.* **89**, 112909 (2006)

[138] Y. J. Park, S. J. Kang, C. Park, *Appl. Phys. Lett*. **88**, 242908 (2006)

[139] M. Chirtoc, E. H. Bentefour, J. S. Antoniow, C. Glorieux, J. Thoen, S. Delenclos, A. H. Sahraoui, S. Longuemart, C. Kolinsky, and J. M. Buisine, *Rev. Sci. Instrum*. **74**, 648 (2003)

[140] V. Bharti, T. Kaura, R. Nath, *IEEE Trans. Dielectr. Electr. Insul.* **4**, 738-741 (1997)